Technische Universität München
Lehrstuhl für Computation in Engineering
UNIVERSITÀ DEGLI STUDI DI PAVIA

Modelling, Validation, and Design for Additive Manufacturing

Applications of Numerical methods to 3D printing processes

Massimo Carraturo

Vollständiger Abdruck der von der Ingenieurfakultät Bau Geo Umwelt der Technischen Universität München zur Erlangung des akademischen Grades eines

Doktor-Ingenieurs

genehmigten Dissertation.

Vorsitzender: Prof. Dr. Ferdinando Auricchio

Prüfer der Dissertation:

1. Prof. Dr. Ernst Rank
2. Prof. Alessandro Reali
3. Prof. Dr. Michele Chiumenti

Die Dissertation wurde am 10.08.2020 bei der Technischen Universität München eingereicht und durch die Ingenieurfakultät Bau Geo Umwelt am 15.10.2020 angenommen.

Università degli Studi di Pavia
Facoltà di Ingegneria

Ingenieurfakultät Bau Geo Umwelt
Lehrstuhl für Computation in Engineering

Modelling, Validation, and Design for Additive Manufacturing

Applications of numerical methods to 3D printing processes

Massimo Carraturo, M.Sc. (hons.)

A Thesis submitted in Partial Fulfilment of the Requirements for the Degree of

Doctor of Philosophy

at the University of Pavia and

Doktor-Ingenieurs

at the Technical University of Munich

Supervisors:
Prof. Alessandro Reali
University of Pavia
Prof. Ernst Rank
Technical University of Munich

Co-advisors:
Prof. Ferdinando Auricchio
University of Pavia
Dr. Stefan Kollmannsberger
Technical University of Munich

XXXII Ciclo (2016-2019)

"Die Wahrheit ist eben kein Kristall, den man in die Tasche stecken kann, sondern eine unendliche Flüssigkeit, in die man hineinfällt"

R. Musil, *Der Mann ohne Eigenschaften*

Abstract

Additive manufacturing (AM) technology has experienced an exponential growth over the last decade. From aerospace industry to biomedical applications, from organic tissues to jewelry production, the range of components that can be produced by means of additive technology is extremely various. Nevertheless, AM is still far from being considered a mature technology. Its limitation is mainly due to the lack of standardization and predictability of AM processes. In fact, these processes involve complex physical phenomena which are extremely challenging to be measured and modelled.

Within the field of AM, numerical methods can be effectively employed to improve the understanding of the physical effects occurring during the manufacturing process, to optimize the process parameters in order to minimize defects in the final artifact, and to develop optimal design specifically suited for AM.

Starting from the above observations, this work aims at developing numerical methods and models specifically tailored to be employed in AM applications. The objective of the present work is to decline novel numerical techniques in the field of AM. To this end, we devote a special effort in the experimental validation of the presented results, which is a necessary step to assess the reliability of the proposed methodologies.

Acknowledgments

I want to thank my Ph.D. advisor at the University of Pavia Prof. Alessandro Reali for his support and all the valuable suggestions he gave me during these years. He was able to create a friendly and motivating working environment, making his group in Pavia a place where I really enjoy to stay and work.

I would also like to thank my Ph.D. advisor at the Technical University of Munich Professor Ernst Rank for giving me the opportunity to join his group at the Chair of Computational in Engineering, first as an HiWi and then as a Ph.D. student. His precious advises during our scientific discussions drove all my research activity in these years.

I want to thank Professor Ferdinando Auricchio for the enthusiasm and vitality he puts in his work and for all the fruitful discussions we had in these years. I really enjoy working together with him and I am grateful to be part of his team in Pavia.

A special thank goes to Dr. Stefan Kollmannsberger because without knowing him I probably would have not taken this path. Since the very beginning, he has always inspired and strongly supported me. I am sure that, not only our friendship, but also our scientific collaboration will continue in the future.

Many thanks to Professor Carlotta Giannelli and Dr. Rafael Vázquez, our collaboration was very inspiring for me and gave me the opportunity to learn a lot.

I want to thank Dr. Brandon Lane and Dr. Ho Yeung for making the months I spent in their lab at NIST a great occasion to learn many new things on additive manufacturing and in particular to gather different points of view on my research topics. I personally found our collaboration very exciting and I hope we will continue to collaborate in the future.

I wish to thank also Dr. Gianluca Alaimo for the uncountable things I am learning working together with him and also for his dedication and genuine passion to his work which strongly motivates me.

I want to thank to John, for his help and for all the effort he dedicated in the work we made together.

Many thanks to my two friends Luca and Davide, from them I learned a lot and together we have spent many of the best moments of my Ph.D. traveling around the world, attending conferences, and partying together.

Thank you very much to all the CompMech group in Pavia: Michele, Simone, Lorenzo, Laura, Alessia, Gianmaria, Mauro, Alfredo, Guille, John Eric (a.k.a. Giorgione), Alex, Alice, Alberto S., Alberto C., Stefania, Erika, Giulia, Franca, Vale, Rodrigo, Marghe, Valeria and Gaetano. I want also to thank the SAM group in Munich for making me feel at home every time I come back at the Chair: Nina, Ali, Alex, Laszlo, Mohamed, Philipp, Nils, Tino, Lisa and Benjamin.

A very special thank to my mom, my dad, my grandmother and my sister Chiara, which

have supported me through all my life.

Finally, I want to thank the person who made all this possible, changing my life with her kindness and genuine love, motivating and supporting me every day either when we are together at home or far away in different continents: Thank you Alice.

Massimo Carraturo

Pavia, September 2019

Contents

Acknowledgments **iii**

1 Introduction **1**
1.1 Motivations . . . 1
1.2 Objectives . . . 4
1.3 Outline . . . 4

2 Adaptive Isogeometric Analysis for Heat Transfer Problems **7**
2.1 Heat transfer problem . . . 8
2.2 Truncated hierarchical B-splines . . . 9
2.2.1 Introduction to hierarchical spaces . . . 9
2.2.2 The truncated basis . . . 9
2.2.3 Admissible meshes . . . 11
2.3 Adaptive isogeometric analysis . . . 13
2.3.1 Spatial discretization . . . 13
2.3.2 Time integration . . . 14
2.3.3 Error estimator . . . 14
2.4 Algorithms for admissible adaptivity . . . 15
2.4.1 Overview of the scheme . . . 15
2.4.2 Refinement . . . 15
2.4.3 Coarsening . . . 17
2.5 Numerical examples . . . 18
2.5.1 2D Benchmarks . . . 18
2.6 Summary and further outlooks . . . 24

3 Numerical Modelling and Experimental Validations **29**
3.1 Governing equations . . . 30
3.2 Model Verification . . . 32
3.3 Model Validation . . . 32
3.3.1 Benchmark cases . . . 33
3.3.2 Isotropic conductivity model . . . 34
3.3.3 Anisotropic conductivity model . . . 43
3.4 Summary and further outlooks . . . 44

4 Real-time Feed Forward Control using a-priori Simulation Results **47**
4.1 Laser system . . . 48

4.2 Control strategies for laser powder bed fusion technology . . . 48
4.2.1 Laser scan control strategies . . . 49
4.2.2 Co-axial thermal camera signal . . . 49
4.2.3 Conversion to true temperature field . . . 49
4.3 Real-time process control . . . 51
4.3.1 From simulated "true" temperatures to camera signal . . . 51
4.3.2 Towards real-time control . . . 52
4.4 Summary and further outlooks . . . 52

5 Part-scale Additive Manufacturing Thermal Process Simulations using the Finite Cell Method 55
5.1 Thermal analysis . . . 56
5.1.1 Governing equations . . . 56
5.1.2 Boundary conditions . . . 57
5.1.3 Time integration . . . 58
5.2 Numerical model for complex geometry part-scale simulation . . . 58
5.2.1 Finite Cell Method . . . 58
5.2.2 Multiple layer-by-layer element activation scheme . . . 59
5.3 Applications . . . 59
5.4 Summary and further outlooks . . . 61

6 Functionally Graded Material Design for Additive Manufacturing 65
6.1 Topology Optimization: From origins to functionally graded material design . 66
6.1.1 Original approach to structural topology optimization . . . 66
6.1.2 Phase field method in topology optimization . . . 68
6.1.3 Functionally graded material design optimization . . . 74
6.2 Numerical and Experimental Results . . . 81
6.2.1 Verification of the asymptotic homogenization assumption . . . 82
6.2.2 Two dimensional MBB . . . 83
6.2.3 Three dimensional MBB . . . 86
6.2.4 L-bracket design . . . 88
6.3 Summary and further outlooks . . . 89

7 Conclusion and outlook 95
7.1 Summary of scientific conclusions . . . 95
7.2 Future research . . . 96

A AMBench CHAL-AMB2018-02 107

B Inconel 625 thermal properties 110

C Steel 316L thermal properties 111

D Analytical results for FGM Topology Optimization 112

List of Figures

1.1 Laser powder bed fusion systems 2
1.2 Example of structures designed for AM. Left: an architectural spider bracket (https://altairenlighten.com/). Right:crystallon, lattice structures in Rhino and Grasshopper (https://noizear.com). 3

2.1 Univariate hierarchical B-splines defined on three refinement levels. The elements $\hat{Q}_i$ are selectively activated to refine the discretization towards the right-end of the domain. Active basis functions (solid lines) are shown together with inactive functions (dashed line). 10
2.2 Univariate truncated hierarchical B-splines defined on three refinement levels. The elements $\hat{Q}_i$ are selectively activated to refine the discretization towards the right-end of the domain. Active truncated basis functions on each level are shown. 11
2.3 Circular arc scan track: Heat source moving on a circular arc, the red arrow indicates the scan path (all distances are in mm). 20
2.4 Circular arc scan track: DOFs (left) and relative errors (right) comparison at each time step for different levels of refinement using adaptive THB-splines and uniform tensor-product meshes. 21
2.5 Circular arc scan track: CPU time comparison at each time step for different levels of refinement using adaptive THB-splines and uniform tensor-product meshes. 21
2.6 Circular arc scan track: DOFs (left) and relative errors (right) for the admissible adaptive mesh with $m = 2$ and $m = 3$, the function support balancing [Lorenzo et al., 2017] and a non-admissible mesh. 22
2.7 Circular arc scan track: Evolution of the temperature distribution for admissible meshes with $m = 2$ at time steps 1, 10 and 20. 23
2.8 Circular arc scan track: Evolution of the non-admissible (left) and admissible with $m = 2$ (right) adaptive meshes at time steps 1, 10, 20 (from top to bottom). 24
2.9 Alternate scan directions: Heat source moving on multiple adjacent tracks (in red) with alternate directions. 25
2.10 Alternate scan directions: CPU time (left) and DOFs (right) comparison at each time step between uniform, admissible and non-admissible adaptive meshes with 9 levels of refinements. 26
2.11 Alternate scan directions: Internal (left) and total (right) energy of the system at each time step between uniform, admissible and non-admissible adaptive meshes with 9 levels of refinements. 26

2.12 Alternate scan directions: Evolution of the non-admissible (left) and admissible (right) temperature distributions at time steps 40, 150, 330, and 500 (from top to bottom) with contour lines at 1000, 1500, 2000 and 2500°C. 27
2.13 Alternate scan directions: Evolution of the non-admissible (left) and admissible (right) adaptive meshes at time steps 40, 150, 330, and 500 (from top to bottom). 28

3.1 Phase change function for different values of the parameter S. 31
3.2 Goldak model for the heat flux input. The model consists in a double-ellipse on which a gaussian profile is defined. 32
3.3 Bare plates of IN625 used for AMBench experiments. Courtesy of NIST. . . . 33
3.4 Additive Manufacturing Metrology Testbed (AMMT) and its thermography setup, which uses a long distance microscope and angled first-surface mirror mounted in an argon purge box. Courtesy of NIST. 34
3.5 CBM machine. Sensitivity studies w.r.t. the emissivity of the material ϵ. . . 36
3.6 CBM machine. Sensitivity studies w.r.t. the absorptivity of the material η. . 37
3.7 CBM machine. Sensitivity studies w.r.t. the power fraction f_f/f_r. 38
3.8 CBM machine. Sensitivity studies w.r.t. the radius ratio c_r/c_f. 39
3.9 Computation of the temperature profile calibrated to case 7 in Ghosh et al. [2018]. 40
3.10 Computation of cross section (red line) calibrated to case 7 in Ghosh et al. [2018]. 41
3.11 Power density profile. 42
3.12 Scaling of the conductivity in direction $i = x, y, z$. 43
3.13 Melt pool cross section micrograph image 50×DF (from `https://phasedata.nist.gov/rest/blob?id=5b102edd4407e700870ff13e`) over computed cross sections using isotropic (dashed red line) and anisotropic conductivity (dashed green line). 44

4.1 Typical scheme of a two-dimensional (x-y) optical scan system [Yeung et al., 2016]. 48
4.2 Block diagram feedback control from Fox et al. [2016]. 50
4.3 Block diagram describing measurement process. The blue squared blocks indicates the physical quantities, the green diamond blocks the conversion functions and the yellow squared blocks the input data required for each function. . . . 50
4.4 Block diagram feedback control employing as reference a digitalized numerical solution in the same co-axial field of view of the thermal camera, where Q is the laser power and v indicates the laser speed. 51
4.5 Conversion steps from simulated ground truth temperature in degree Celsius to camera signal in digital level. 52
4.6 Comparison between simulated temperature signal and real thermal image. . . 53

5.1 Concept of Finite Cell Method 58
5.2 GE-bracket: CAD model of an optimized GE Bracket. 60

5.3 GE-bracket: FCM analysis procedure, the original .stl file is in a first step embedded within a cartesian grid (inactive cells are hidden in the figure) to construct the voxel integration grid, we can then perform a layer-by-layer thermal analysis where the BCs are applied directly on the .stl surfaces. 60
5.4 GE-bracket: FCM grid embedding the CAD model. 61
5.5 GE-bracket: Temperature distribution at different heating time steps hts. . . . 62
5.6 GE-bracket: Temperature distribution at the last time step ($ts = 120$). 63
5.7 GE-bracket: Temperature distribution around a geometrical detail of the bracket. 63

6.1 Example of checkboard pattern for simply supported beam problem from Sigmund and Petersson [1998]. 67
6.2 Example of mesh dependency for simply supported beam problem from Sigmund and Petersson [1998]. 67
6.3 a) Schematic representation of the FGM; b) microstructure consisting of square cells with centrally-placed squared holes (RVE). 76
6.4 Macroscopic strain histories applied to the RVE for the evaluation of the components of the homogenized material tensor $\mathbb{C}^H(\chi)$. a) $\bar{\varepsilon}_{11}$, b) $\bar{\varepsilon}_{22}$, c) $\bar{\gamma}_{12}$ 77
6.5 One-quarter traction test. All units are in mm. 82
6.6 Microstructure domains with different cell sizes and density fraction $\rho_f = 0.5$. . 82
6.7 Two dimensional MBB: half-domain setup. 83
6.8 Two dimensional MBB: Evolution of the density variable χ at different time steps t. 84
6.9 A complete pipeline from a continuously graded numerical solution to a 3D printed FGM structure; a) phase-field based topology optimization, b) generation of 3D virtual model from the discrete maps of the field variables, c) finished 3D virtual model, d) 3D-printed part 85
6.10 Specimens used in the experiment. 86
6.11 Load vs displacements plot. 87
6.12 Three dimensional MBB: domain setup. The red area indicates the surface where the load is applied, while the blue areas the surfaces where Dirichlet BCs are aplied 87
6.13 Three dimensional MBB: Evolution of the material variable ϕ at different time steps t. 88
6.14 Three dimensional MBB: Evolution of the density variable χ at different time steps t. 89
6.15 Three dimensional MBB: compliance evolution. 90
6.16 Three dimensional MBB: density distribution of optimized structure. Longitudinal plane clip. 90
6.17 L-bracket: domain setup. The red area indicates the surface where the load is applied, while the blue area the clamped surface. 91
6.18 L-bracket: Evolution of the density variable χ at different time steps t. Midplane section view. 92
6.19 L-bracket: density variable χ distribution in the optimized structure. 93
6.20 L-bracket: Von Mises stress distribution in the optimized structure. 93
6.21 L-bracket: compliance evolution. 94

A.1 Example of laser traces on the upper surface of a IN625 bare plate used for AMBench measurements. Courtesy of NIST. 107

B.1 IN625; temperature dependent material properties. 110

C.1 Steel 316L; temperature dependent material properties. 111

List of Tables

2.1 Circular arc scan track: Process and material parameters. 19
2.2 Alternate scan directions: Process and material parameters. 25

3.1 CBM machine: parameter values. 34
3.2 AMMT machine: parameter values. 34
3.3 CBM machine: experimental measurements according to www.nist.gov/ambench [2018], CHAL-AMB2018-02-MP. 35
3.4 AMMT machine: experimental measurements according to www.nist.gov/ambench [2018], CHAL-AMB2018-02-MP. 35
3.5 CBM machine: obtained weld pool length l and cooling rates CR. 40
3.6 AMMT machine: computed values. 42
3.7 AMMT machine: deviations from experimental values. 42
3.8 Anisotropic conductivity model: computed values. 44
3.9 Anisotropic conductivity model: deviations of computed values from experimental values. 44

6.1 Compliance and max. displacement value of different microstructures and corresponding homogenized material. 83

A.1 Melt Pool Data ♦ - Solidus could not be detected on these samples. 108
A.2 Cooling Rate Data ▼ - Due to the limited calibration range of camera on AMMT, temperature below 1100°C were too erroneous to use in cooling rate measurements. 109

B.1 IN625; material constant parameters 110

C.1 Steel 316L; material constant parameters 111

Chapter 1

Introduction

1.1 Motivations

Additive Manufacturing (AM) technologies are undergoing an exponential growth in many engineering fields, from aerospace to biomedical applications, from fashion to food industry. The main benefit of this technology is the possibility to design the product such that it is optimized for a specific function. The manufacturing constraints are in fact dramatically reduced and the designer can finally focus more on the intended application of the part rather than on its manufacturability [Gibson et al., 2015].

As a direct consequence of AM diffusion, there is an increasing demand for efficient and reliable numerical technologies not only to enhance the understanding of the physical manufacturing process but also to generate optimal design of 3D printed structures. In the present thesis we aim at investigating the applications of different numerical methods in the field of both AM process of metal 3D-printing systems and optimal design for AM.

Additive manufacturing process simulations

A first classification of additive manufacturing systems can be made based on the material used to build the product (metal, plastic, organic materials, etc.). Once a specific material is chosen it can be manufactured using a large variety of AM systems which address different applications, deliver specific surface finiture, and have also different production costs.

In this work we mainly focus on a specific metal 3D printing technology, namely laser powder bed fusion (LPBF), alternatively known as selective laser melting (SLM, cf. figure 1.1a), selective laser sintering (SLS), electron beam melting (EBM), direct metal laser sintering (DMLS), or direct metal laser melting (DMLM). LPBF is an AM process consisting of a laser beam which selectively melts a layer of metal powder, building the final product by means of a layer-by-layer process, as depicted in figure 1.1b. Nowadays, most of the metal additive manufacturing systems employ a powder bed fusion technology due to the accurate surface finiture, the lower porosity, and the better mechanical properties of the resulting part compared to other AM technologies [King et al., 2015a].

In LPBF systems a single layer is $\approx 30\mu$m thick and the typical laser beam radius is $30 - 50\mu$m, while the dimensions of the product are in the order of decimeters. This multi-scale nature in space makes the simulation of such a process an extremely challenging

(a) Selective Laser Melting metal 3D printer (Renishaw AM400) located in the laboratories of the University of Pavia (http://www-4.unipv.it/3d/laboratories/3dmetalunipv/).

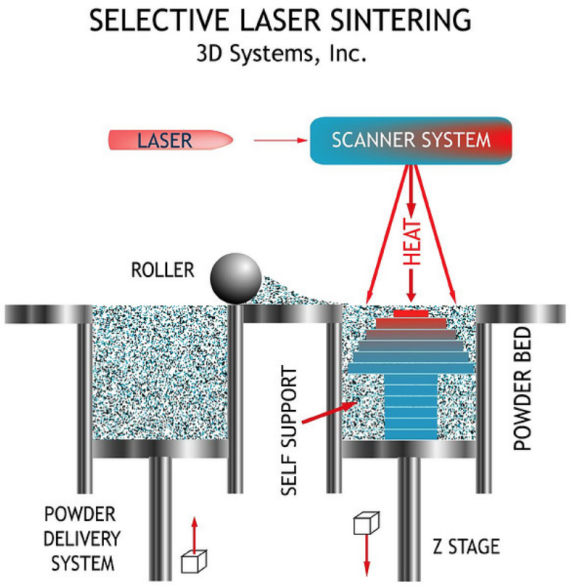

(b) Overview of a laser powder bed fusion system (Selective Laser Sintering by 3D Systems, Inc.)

Figure 1.1: Laser powder bed fusion systems

task. Moreover, melting and solidification phenomena occur in few microseconds in a very small region around the laser spot. Considering that a complete LPBF process lasts hours, we can immediately understand that the computational costs for a high-fidelity simulation of such a process easily becomes too expensive even for the most recent supercomputers (see, e.g., [Heigel and Lane, 2017; King et al., 2015b; Lundbäck and Lindgren, 2011; Pal et al., 2016; Papadakis et al., 2014]). In particular, we can identify three main open tasks in developing a validated and reliable simulation tool for this kind of processes:

1. Develop a suitable physical and numerical model to represent the phenomena occurring during the process [Dunbar et al., 2016; Lu et al., 2018];
2. Deliver accurate measurements of the physical parameters to validate the physical and numerical model [Ghosh et al., 2018];
3. Develop a numerical technology which addresses the computational issues coming from the multi-physics and multi-scale nature of the problem [Chiumenti et al., 2017a; Denlinger et al., 2017].

Moreover, to obtain a real advance in the understanding and control of powder bed fusion systems, all these different topics have to be linked together. To this end, numerical simulations of 3D printing processes should aim at creating a bridge between the different research areas of additive manufacturing, from design optimization to process control systems. In fact, once an optimal design (e.g., minimizing the mass under a stress constraint) is found, it is not straightforward to obtain the corresponding AM product matching the designed shape and mechanical properties. For example, high residual stresses generated during the building process may lead to strong deformations of the final artifact once removed from the building

platform. Additionally, it may occur that local overheating due to critical geometrical features leads to void inclusions in the microstructure, compromising the mechanical behavior of the component. All these and other process-related issues can be potentially predicted by means of numerical simulations. In this sense, reliable numerical models can lead to an actual improvement of the technology itself allowing to choose and control optimal process parameters for specific AM processes.

Design for additive manufacturing

As initially mentioned, the true benefit behind the success of additive manufacturing is the radical shift introduced in the design perspective. In fact, with AM technology, the classical design for manufacturing, in which the designer has to take into account the manufacturing constraints before the actual functionality of the product, can be now replaced by a functional design, or design for additive manufacturing (DfAM), where the focus is now put on the efficiency and functionality of a specific component with respect to its target application (see e.g., figure 1.2).

Figure 1.2: Example of structures designed for AM. Left: an architectural spider bracket (https://altairenlighten.com/). Right:crystallon, lattice structures in Rhino and Grasshopper (https://noizear.com).

A large variety of numerical methods have been developed helping the designer to obtain optimal shapes and topologies for mechanical and structural components, see [Allaire, 2015; Eschenauer and Olhoff, 2001; Sigmund and Maute, 2013] for detailed reviews. All these methods have found in the additive manufacturing system their natural application, since AM allows to directly produce the optimal design generated by the algorithm almost without any limitation related to its complexity.

Within this framework, the so-called functionally graded material design (FGMD) additionally extends the design flexibility building performance-driven functionality directly into the material micro-structure of the component. Contrary to the standard approach where an homogeneous material is assigned to a pre-shaped domain, FGMD allows to vary in a continuous fashion the material properties of the final product, enhancing material distribution at the sub-millimeter scale.

1.2 Objectives

The aim of the present thesis is to investigate the application of numerical methods in the field of AM, showing their possible usage from a design stage up to machinery control. Validated and reliable numerical methods can be effectively employed to optimize all the steps of AM production, from optimal shape and topology design to the optimization of process parameters.

Before declining a numerical method in all its possible usages, we attach the utmost importance to a thorough investigation of both numerical schemes and physical models able to effectively capture the complex nature of the physical phenomena occurring during AM processes. First, we aim at verifying and validating an isogeometric approach to thermal analysis of AM together with the development of a robust yet minimal physical model. The goal of this preliminary work is to provide a reliable numerical framework which could be later used in practical applications. At the same time, we investigate another numerical method, the so-called phase-field method, which we employ in topology optimization of functionally graded components.

Among this broad range of applications we focused mainly on two fundamental problems: thermal analysis of LPBF processes and FGM design. Thermal analysis of LPBF processes is an extremely challenging topic which involves metrology, material, and numerical science aiming at obtaining accurate measurements of the complex physical phenomena occurring during AM processes. We consider both meso and macro-scale thermal simulations. The former can be used, e.g., to predict the melt-pool shape behavior in presence of critical geometrical features, or alternatively to obtain a reference solution which can be potentially employed for *real-time* process control. The latter, is meant to predict macro-scale effects occurring during LPBF processes and can be employed to estimate residual stresses in the final artifact. FGM design is a recent topic which is gaining more and more importance among AM productions since it allows to exploit the new design possibilities introduced by AM technology. Also in this field, numerical methods can play a crucial role if we want to make use of all the technological potential of AM. In fact, nowadays it is possible to obtain structural components fulfilling the same time manufacturing constraints and optimal design only by means of numerical procedures.

The *fil rouge* of the results presented within this thesis can be found in the desire to decline non-standard numerical methods within the wide field of additive manufacturing, trying to give new resources for the understanding of this exciting and powerful technology.

1.3 Outline

The outline of the thesis is structured as follows: chapter 2 presents an adaptive isogeometric scheme suitable to simulate thermal problems with a localized heat source, i.e., the simplest numerical model describing an LPBF process. This numerical method is applied to 2D examples to show its efficiency in solving highly localized thermal problems compared to standard FEM and another adaptive isogeometric method present in literature. Chapter 3 introduces a numerical model to predict melt-pool geometry based on an anisotropic thermal conductivity definition. The model is validated employing the experimental results obtained at the National Institute of Standards and Technology (NIST) within the context of the AMBench2018. Chapter 4 presents a conversion procedure to obtain, from the simulated continuous temperature

field, a corresponding digital signal in the field of view of a thermal camera, such that a pixel-by-pixel comparison can be directly performed, potentially opening the door to real-time control of LPBF processes employing simulated results as *ground-truth* solution. In chapter 5 an immersed numerical method based on the Finite Cell Method (FCM) is employed to perform part-scale thermal analysis. The numerical procedure is applied to predict the thermal distribution during the building process of an industrial component. Chapter 6 presents a topology optimization procedure based on the phase-field method and asymptotic homogenization to obtain FGM structures. The proposed numerical procedure is validated by means of a 3-point bending test for a plane-stress structure. 3D computational results of the same problem are also presented. Finally, in chapter 7 we draw the main conclusions of the thesis and possible further outlooks for these researches. Finally, in the Appendices we report AMBench2018 experimental data, Inconel 625 and steel 316L thermal properties, and the main analytical results and proofs for chapter 6.

Chapter 2

Adaptive Isogeometric Analysis for Heat Transfer Problems

Isogeometric analysis (IGA) [Cottrell et al., 2009; Hughes et al., 2005] is a paradigm to solve partial differential equations employing smooth spline functions as basis for the analysis. The classical isoparametric approach of the finite element method is reversed and the exact geometry representation is now introduced within the analysis. The original idea underlying this novel approach is to develop a tight connection between computer aided design (CAD) and numerical analysis, with the aim of performing analysis directly from CAD models to avoid tedious and time-consuming meshing processes. IGA has been so far successfully applied in many engineering fields including, among others, structural analysis [Cottrell et al., 2007], biomechanics [Kamensky et al., 2015], structural dynamics [Hughes et al., 2014], and contact mechanics [De Lorenzis et al., 2014].

As CAD standard for spline representations, B-splines and non-uniform rational B-splines (NURBS) are the most commonly used spline technologies in the isogeometric setting. Nevertheless, due to their tensor product structure, they are not well suited to treat localized phenomena. Hierarchical B-splines (HB-splines) [Forsey and Bartels, 1988; Kraft, 1997] is an adaptive spline technology that enables the possibility to properly deal with local problems. Its application in isogeometric analysis has been widely studied, see e.g. [Schillinger et al., 2012; Scott et al., 2014; Vuong et al., 2011]. Based on the multi-level concept of HB-splines, truncated hierarchical B-splines (THB-splines) [Giannelli et al., 2012], have also been proposed as an effective tool to perform hierarchical refinement while reducing the interactions between different levels in the spline hierarchy. The truncated basis has been successfully applied in different problems related to computer aided design [Bracco et al., 2018a; Kiss et al., 2014] and isogeometric analysis [D'Angella et al., 2018; Giannelli et al., 2016; Hennig et al., 2016; Marussig et al., 2018]. It is worth to mention that, while several papers investigated refinement schemes for adaptive isogeometric methods in the last years, only very recently, few authors also focused on the study of suitable and effective mesh coarsening [Hennig et al., 2018; Lorenzo et al., 2017].

In this chapter we discuss a novel, adaptive numerical scheme, as introduced in Carraturo et al. [2019a]. The proposed method is based on THB-splines defined on suitably graded meshes to solve linear heat transfer problem including a localized heat source. The THB-spline refinement routine follows the approach introduced in Buffa and Giannelli [2016], while the

coarsening algorithm which automatically preserves the grading properties of the hierarchical mesh configuration is newly introduced. Even if our simple model neglects many features of the process, it still includes the spatial multi-scale issue present in LPBF processes. The choice of employing an adaptive isogeometric scheme to solve the problem of a traveling laser source is justified by the presence of high thermal gradients in the region surrounding the laser beam. In Kollmannsberger et al. [2018] it is demonstrated that high-order schemes combined together with adaptive mesh refinement and coarsening can optimally treat localized problems involving steep gradients, motivating the choice of employing an adaptive isogeometric method for this kind of applications.

We outline that, even if we consider a simple, linear, two-dimensional model, the presented algorithms can be directly extended to 3D, non-linear, and multi-physics problems due to the flexibility of the presented discretization technique.

2.1 Heat transfer problem

In this section the strong and the weak form of the governing equations of a heat transfer problem are presented.

Assuming the material obeys the Fourier's law of heat conduction with a Lagrangian reference frame, the problem can be written using the linear heat transfer model as described in Bathe [2007]. Let us consider a temporal domain $T \subset \mathbb{R}$ and a spatial domain $\Omega \subset \mathbb{R}^2$ with Neumann boundaries Γ_N such that $\Gamma_N = \partial\Omega$. The heat flow equilibrium in the interior of the body gives:

$$C_p\rho\frac{\partial\theta(\mathbf{x},t)}{\partial t} - \nabla\cdot(k\nabla\theta(\mathbf{x},t)) = f(\mathbf{x},t) \qquad \text{in} \quad \Omega\times T, \tag{2.1}$$

where f is the external heat source, k is the thermal conductivity, C_p is the specific heat capacity and ρ is the density of the solid material.

The problem in equation (2.1) is solved with respect to the temperature field $\theta = \theta(\mathbf{x},t)$ function of space and time, and defined under the following initial conditions

$$\theta(\mathbf{x},0) = \theta_0, \qquad \text{in} \quad \Omega, \tag{2.2}$$

and adiabatic boundary conditions

$$k\nabla\theta(\mathbf{x},t)\cdot\mathbf{n} = 0, \qquad \text{on} \quad \Gamma_N\times T, \tag{2.3}$$

where θ_0 is the initial temperature of the body and $\mathbf{n}$ is the exterior unit normal vector. Note that we consider a simple linear heat transfer model in order to focus on the spatial discretization of the problem defined in equations (2.1) to (2.3). Consequently, we consider only the adiabatic boundary conditions defined in equation (2.3) by neglecting radiation and convection effects on the domain boundaries.

At time t the weak solution of the problem in equations (2.1) to (2.3) is obtained using the *principle of virtual temperature* which can be written as follows:

$$C_p\rho\int_\Omega\tilde{\theta}(\mathbf{x},t)\frac{\partial\theta}{\partial t}(\mathbf{x},t)d\Omega + k\int_\Omega\nabla\tilde{\theta}(\mathbf{x},t)\cdot\nabla\theta(\mathbf{x},t)d\Omega = \int_\Omega\tilde{\theta}(\mathbf{x},t)f(\mathbf{x},t)d\Omega \tag{2.4}$$

where $\tilde{\theta}$ is the virtual temperature.

2.2 Truncated hierarchical B-splines

This section presents the basic concepts of *admissible* adaptive isogeometric methods, by exploiting truncated hierarchical B-splines Giannelli et al. [2012] defined on suitably graded meshes as basis for the analysis. The definitions of this section mainly follow Buffa and Giannelli [2016, 2017], where a sound mathematical theory for adaptive isogeometric methods is fully developed, while related numerical results were recently presented in Bracco et al. [2019].

2.2.1 Introduction to hierarchical spaces

Given a nested sequence of parametric domains $\hat{\Omega}^0 \supseteq \ldots \supseteq \hat{\Omega}^{N-1}$, subsets of a closed hyper-rectangle $D \in \mathbb{R}^d$ (d=2,3), we can construct the hierarchical B-spline space of depth N by considering a hierarchy of nested tensor-product B-spline spaces of degree p, $\hat{V}^0 \subset \hat{V}^1 \subset \ldots \subset \hat{V}^{N-1}$. These spaces have associated the bases $\hat{\mathcal{B}}^\ell$ and a rectangular grid $\hat{G}^\ell$ for each level ℓ, with $\ell = 0, 1, \ldots, N-1$. We assume that the domain $\hat{\Omega}^\ell$ considered at level ℓ is the union of cells of the previous level $\ell - 1$. A hierarchical mesh $\hat{\mathcal{Q}}$ collects the active cells which represent the elements of our discretization. It can be defined as

$$\hat{\mathcal{Q}} := \left\{ \hat{Q} \in \hat{\mathcal{G}}^\ell, \ell = 0, \ldots, N-1 \right\},$$

where $\hat{\mathcal{G}}^\ell$ is the set of active cells of level ℓ, namely

$$\hat{\mathcal{G}}^\ell := \left\{ \hat{Q} \in \hat{G}^\ell : \hat{Q} \subset \hat{\Omega}^\ell \wedge \hat{Q} \not\subset \hat{\Omega}^{\ell+1} \right\}.$$

Figure 2.1 shows an example of hierarchical mesh for $d = 1$. Figures 2.8 and 2.13 in section 2.5 instead illustrate several hierarchical mesh configurations for $d = 2$. In the present work we consider only dyadic refinement, i.e., the children $\hat{Q}_i$, $i = 1, \ldots, 2^d$, of an active cell $\hat{Q}$ are obtained by bisection. We finally define the hierarchical B-spline basis $\hat{\mathcal{H}}$ on the hierarchical mesh $\hat{\mathcal{Q}}$ as:

$$\hat{\mathcal{H}}(\hat{\mathcal{Q}}) := \left\{ \hat{\beta} \in \hat{\mathcal{B}}^\ell : \mathrm{supp}\hat{\beta} \subseteq \hat{\Omega}^\ell \wedge \mathrm{supp}\hat{\beta} \not\subseteq \hat{\Omega}^{\ell+1}, \ell = 0, \ldots, N-1 \right\}, \tag{2.5}$$

where $\mathrm{supp}\hat{\beta}$ denotes the intersection of the support of $\hat{\beta}$ with $\hat{\Omega}^0$. Hierarchical B-splines for a univariate example are shown in figure 2.1.

2.2.2 The truncated basis

B-spline representations offer the possibility of suitably exploiting efficient refinement rules when nested spline spaces are considered. We can then consider the representation of $\hat{s} \in \hat{V}^\ell \subset \hat{V}^{\ell+1}$ with respect to the tensor-product B-spline basis $\hat{\mathcal{B}}^{\ell+1}$,

$$\hat{s} = \sum_{\hat{\beta} \in \hat{\mathcal{B}}^{\ell+1}} c_{\hat{\beta}}^{\ell+1}(s) \hat{\beta},$$

and define the truncation of $\hat{s}$ with respect to level $\ell + 1$ as follows:

$$\mathrm{trunc}^{\ell+1} \hat{s} := \sum_{\hat{\beta} \in \hat{\mathcal{B}}^{\ell+1}, \mathrm{supp}\hat{\beta} \not\subseteq \hat{\Omega}^{\ell+1}} c_{\hat{\beta}}^{\ell+1}(s) \hat{\beta},$$

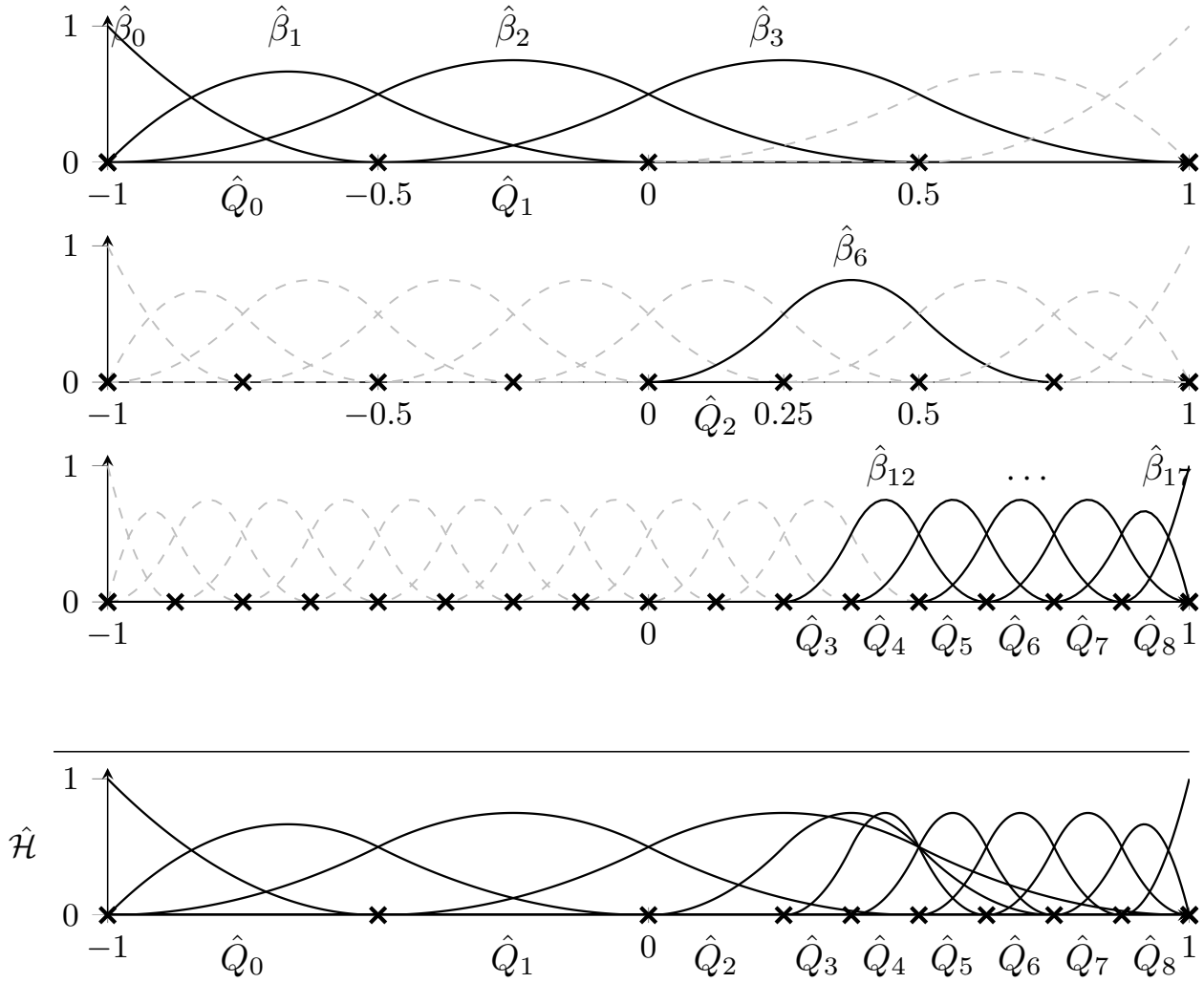

Figure 2.1: Univariate hierarchical B-splines defined on three refinement levels. The elements $\hat{Q}_i$ are selectively activated to refine the discretization towards the right-end of the domain. Active basis functions (solid lines) are shown together with inactive functions (dashed line).

where $c_{\hat{\beta}}^{\ell+1}(s)$ is the coefficient of the function $\hat{s}$ with respect to the basis function $\hat{\beta}$ at level $\ell+1$. By iteratively applying the truncation operation at the hierarchical basis functions in $\hat{\mathcal{H}}$, we obtain the truncated hierarchical basis (see figure 2.2).

Definition 2.2.1:
The truncated hierarchical B-spline (THB-spline) basis $\hat{\mathcal{T}}$ with respect to the mesh $\hat{\mathcal{Q}}$ is defined as

$$\hat{\mathcal{T}}(\hat{\mathcal{Q}}) := \left\{ \mathrm{Trunc}^{\ell+1}\hat{\beta} : \hat{\beta} \in \hat{\mathcal{B}}^{\ell} \cap \hat{\mathcal{H}}(\hat{\mathcal{Q}}), \ell = 0, \dots, N-2 \right\} \bigcup \left\{ \hat{\beta}^{N-1} : \hat{\beta}^{N-1} \in \hat{\mathcal{B}}^{N-1} \cap \hat{\mathcal{H}}(\hat{\mathcal{Q}}) \right\},$$

where $\mathrm{Trunc}^{\ell+1}\hat{\beta} := \mathrm{trunc}^{N-1}(\mathrm{trunc}^{N-2}(\dots(\mathrm{trunc}^{\ell+1}(\hat{\beta}))\dots))$*, for any* $\hat{\beta} \in \hat{\mathcal{B}}^{\ell} \cap \hat{\mathcal{H}}(\hat{\mathcal{Q}})$.

The key basic properties of the truncated basis are the following: non-negativity, linear

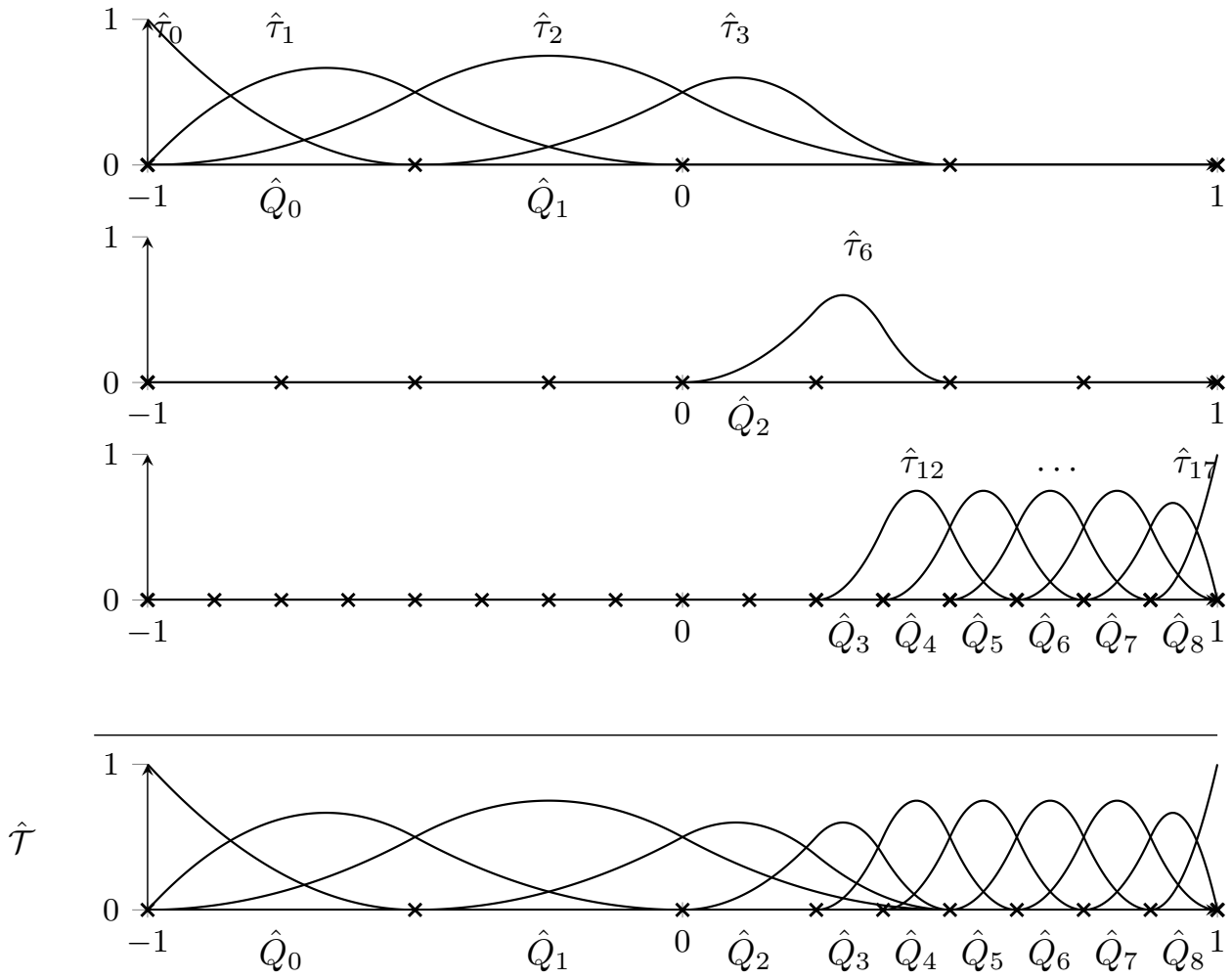

Figure 2.2: Univariate truncated hierarchical B-splines defined on three refinement levels. The elements $\hat{Q}_i$ are selectively activated to refine the discretization towards the right-end of the domain. Active truncated basis functions on each level are shown.

independence, partition of unity, and, in addition, $\operatorname{span}\hat{\mathcal{H}} = \operatorname{span}\hat{\mathcal{T}}$ (cfr. Giannelli et al. [2012]).

2.2.3 Admissible meshes

In this work we use the definition of *classes of admissible meshes* introduced in Buffa and Giannelli [2016].

Definition 2.2.2:
A mesh $\hat{\mathcal{Q}}$ is admissible of class m if the truncated basis functions in $\hat{\mathcal{T}}(\hat{\mathcal{Q}})$ which take non-zero values over any element $\hat{Q} \in \hat{\mathcal{Q}}$ belong to at most m successive levels.

This definition allows to consider hierarchical meshes where the number of THB-splines acting on a single element does not depend on the total number of levels in the hierarchy, but only on the parameter m.

In order to implement the algorithms for admissible refinement and coarsening, see sections 2.4.2 and 2.4.3, we need to consider three additional sets of elements: the *multilevel support extension* of an element, together with the so-called *refinement and coarsening neighborhoods*.

Definition 2.2.3:
The multilevel support extension of an element $\hat{Q} \in \hat{G}^\ell$ with respect to level k, with $0 \leq k \leq \ell$, is defined as:

$$S(\hat{Q}, k) := \left\{ \hat{Q}' \in \hat{G}^k : \exists \hat{\beta} \in \hat{\mathcal{B}}^k, supp\hat{\beta} \cap \hat{Q}' \neq \emptyset \wedge supp\hat{\beta} \cap \hat{Q} \neq \emptyset \right\}.$$

That is, the multilevel support extension is formed by the support of B-splines of level k, such that they do not vanish on an element $\hat{Q}$. By following Buffa and Giannelli [2016], we now consider the neighborhood of an element for the refinement algorithm, which we rename as *refinement neighborhood* to differentiate it from the analogous set used in coarsening.

Definition 2.2.4:
The refinement neighborhood $\mathcal{N}_r(\hat{\mathcal{Q}}, \hat{Q}, m)$ of an element $\hat{Q}$ of level ℓ with respect to the class of admissibility m is defined as:

$$\mathcal{N}_r(\hat{\mathcal{Q}}, \hat{Q}, m) := \left\{ \hat{Q}' \in \hat{\mathcal{G}}^{\ell-m+1} : \exists\, \hat{Q}'' \in S(\hat{Q}, \ell - m + 2), \hat{Q}'' \subseteq \hat{Q}' \right\}.$$

Note that, when considering the element $\hat{Q}$ of level ℓ to be refined into four elements of level $\ell + 1$, we want to guarantee that any THB-spline of level $\ell - m + 1$ acting on $\hat{Q}$ is fully truncated with respect to level $\ell - m + 2$, so that it will vanish on the children of $\hat{Q}$ which will be activated after the refinement of $\hat{Q}$. By (recursively) refining the elements in the multilevel support extension of level $\ell - m + 2$, as in the definition of the refinement neighborhood, guarantees that the admissibility property is maintained. Note however that this choice is conservative in nature, since we do not consider the real support of the THB-splines, but only their truncation with respect to level $\ell - m + 2$, while they could be truncated at intermediate levels depending on the mesh configuration.

Finally, we introduce here the definition of *coarsening neighborhood* of an element, an additional set of elements required for admissible coarsening.

Definition 2.2.5:
The coarsening neighborhood $\mathcal{N}_c(\hat{\mathcal{Q}}, \hat{Q}, m)$ of an element $\hat{Q}$ of level ℓ with respect to the class of admissibility m is defined as:

$$\mathcal{N}_c(\hat{\mathcal{Q}}, \hat{Q}, m) :=$$
$$\left\{ \hat{Q}' \in \hat{\mathcal{G}}^{\ell+m} : \exists\, \hat{Q}'' \in \hat{\mathcal{G}}^{\ell+1} \text{ and } \hat{Q}'' \subset \hat{Q}, \text{ with } \hat{Q}' \in S(\hat{Q}'', \ell + 1) \right\}.$$

The set $\mathcal{N}_c(\hat{\mathcal{Q}}, \hat{Q}, m)$ includes the active elements of level $\ell + m$ that are contained in the support extension of the children of $\hat{Q}$. By starting from an admissible mesh of class m, when considering the element $\hat{Q}$ of level ℓ to be reactivated, to preserve the admissibility condition we have to ensure that newly activated basis functions will vanish on the elements of level $\ell + m$. This is guaranteed when the coarsening neighborhood is empty, because newly added functions will be fully truncated with respect to level $\ell + 1$. This property allows us to define a fully automatic way to preserve admissibility of the mesh, that we exploit in the algorithm of Section 2.4.3.

2.3 Adaptive isogeometric analysis

In this section the discrete form of the problem of section 2.1 is derived.

2.3.1 Spatial discretization

In order to define the mesh and basis functions for the physical domain Ω we introduce the isogeometric mapping $\mathbf{F} : \hat{\Omega}^0 \to \Omega$, such that:

$$\mathbf{x} \in \Omega, \quad \mathbf{x} = \mathbf{F}(\hat{\mathbf{x}}) = \sum_{\hat{\tau} \in \hat{\mathcal{T}}^0} \mathbf{C}_{\hat{\tau}} \hat{\tau}\left(\hat{\mathbf{x}}\right),$$

with $\hat{\mathbf{x}} \in \hat{\Omega}^0$, $\mathbf{C}_{\hat{\tau}} \in \mathbb{R}^d$, and where $\hat{\mathcal{T}}^0$ is the truncated basis defined on an initial tensor-product mesh.

The corresponding hierarchical mesh in the physical domain can be written as:

$$\mathcal{Q} = \left\{ Q = \mathbf{F}(\hat{Q}) : \hat{Q} \in \hat{\mathcal{Q}} \right\}$$

and, analogously,

$$\Omega^\ell = \mathbf{F}(\hat{\Omega}^\ell), \quad \mathcal{G}^\ell = \left\{ Q \in \mathcal{Q} : \hat{Q} \in \hat{\mathcal{G}}^\ell \right\} \quad \text{and} \quad G^\ell = \left\{ Q \subset \Omega : \hat{Q} \in \hat{G}^\ell \right\}.$$

The weak form of the heat transfer problem equation (2.4) can now be written in a discrete form applying the isogeometric expansion to the temperature field θ, such that:

$$\theta(\mathbf{x}, t) = \mathbf{N}(\mathbf{x})\boldsymbol{\theta}_t,$$

where $\boldsymbol{\theta}_t$ is the column vector of temperature degrees of freedom (DOFs) of the hierarchical mesh $\mathcal{Q}$ at time t and $\mathbf{N}(\mathbf{x})$ is the row vector of the corresponding THB-spline basis functions. We can now rewrite the integrals of equation (2.4) at a given instant in time in a matrix form, such that:

$$\mathbf{M}\dot{\boldsymbol{\theta}}_t + \mathbf{K}\boldsymbol{\theta}_t = \mathbf{f}_t, \tag{2.6}$$

where

$$\mathbf{M} = C_p \rho \int_\Omega \mathbf{N}^T \mathbf{N} d\Omega, \quad \mathbf{K} = k \int_\Omega \mathbf{B}^T \mathbf{B} d\Omega,$$

and

$$\mathbf{f}_t = \int_\Omega \mathbf{N}^T f(\mathbf{x}, t) d\Omega,$$

with $\mathbf{B}(\mathbf{x}) = \nabla \mathbf{N}(\mathbf{x})$. Equation (2.6) presents the time derivative of the temperature vector, therefore an additional discretization in time is required to numerically solve the problem.

2.3.2 Time integration

The linear system in equation (2.6) is approximated in time using the unconditionally stable backward Euler approach. At time $t + \Delta t$, equation (2.6) can be written in terms of the temperature increment $\Delta\boldsymbol{\theta}_{t+\Delta t}$ as:

$$\mathbf{M}\Delta\boldsymbol{\theta}_{t+\Delta t} + \Delta t\mathbf{K}\Delta\boldsymbol{\theta}_{t+\Delta t} = \Delta t\mathbf{f}_{t+\Delta t} - \Delta t\mathbf{K}\boldsymbol{\theta}_t, \tag{2.7}$$

where Δt is the constant time increment at each time step and $\boldsymbol{\theta}_t$ is the the solution vector at the previous time step. Finally, we can iteratively solve the discrete problem defined in equation (2.7) using the algorithms described in the next section.

2.3.3 Error estimator

Before describing the implementation of the numerical method, we introduce the error estimator used to drive our adaptive scheme. We employ a residual-based *a posteriori* error estimator $\varepsilon_{\mathcal{Q}}$ defined as:

$$\varepsilon^2_{\mathcal{Q}}(\theta, \mathcal{Q}) = \sum_{Q\in\mathcal{Q}} \varepsilon^2_Q, \tag{2.8}$$

where

$$\varepsilon^2_Q = h^2_Q \int_Q \mid f_{t+\Delta t} - C_p\rho\frac{\theta_{t+\Delta t} - \theta_t}{\Delta t} + \nabla\cdot(k\nabla\theta_{t+\Delta t}) \mid^2 dQ$$

and h_Q is the size of the element Q. For simplicity, since we are using homogeneous Neumann boundary conditions, we neglect the boundary terms that should appear in the estimator.

Finally, to estimate the quality of the results with respect to a reference solution $\boldsymbol{\theta}_{t,ref}$, we need to define the error with respect to a certain norm. To this end we employ two different definitions of the energy of the system. Following O'Hara et al. [2011], we define the internal energy of the system $\mathcal{E}_i(\boldsymbol{\theta}_t, \boldsymbol{\theta}_t)$ at time t as

$$\mathcal{E}_i(\boldsymbol{\theta}_t, \boldsymbol{\theta}_t) = \frac{k}{2}\int_\Omega \nabla\theta_t\cdot\nabla\theta_t d\Omega,$$

whereas the total energy of the system $\mathcal{E}_T(\boldsymbol{\theta}_t, \boldsymbol{\theta}_t)$ at time t is defined as

$$\mathcal{E}_T(\boldsymbol{\theta}_t, \boldsymbol{\theta}_t) = \frac{1}{2}\left(k\int_\Omega \nabla\theta_t\cdot\nabla\theta_t d\Omega + C_p\rho\int_\Omega \theta_t\frac{\partial\theta_t}{\partial t}d\Omega\right).$$

We can then define the relative error in internal and total energy at a given instant in time t as

$$\varepsilon_i = \sqrt{\frac{\mid \mathcal{E}_i(\boldsymbol{\theta}_{t,ref}, \boldsymbol{\theta}_{t,ref}) - \mathcal{E}_i(\boldsymbol{\theta}_t, \boldsymbol{\theta}_t) \mid^2}{\mid \mathcal{E}_i(\boldsymbol{\theta}_{t,ref}, \boldsymbol{\theta}_{t,ref}) \mid^2}} \quad \text{and}$$

$$\varepsilon_T = \sqrt{\frac{\mid \mathcal{E}_T(\boldsymbol{\theta}_{t,ref}, \boldsymbol{\theta}_{t,ref}) - \mathcal{E}_T(\boldsymbol{\theta}_t, \boldsymbol{\theta}_t) \mid^2}{\mid \mathcal{E}_T(\boldsymbol{\theta}_{t,ref}, \boldsymbol{\theta}_{t,ref}) \mid^2}},$$

respectively.

2.4 Algorithms for admissible adaptivity

This section presents the implementation of admissible adaptivity that we developed in GeoPDEs starting from the algorithms previously implemented in the code and described in [Bracco et al., 2018b; Garau and Vázquez, 2018]. The initial set of algorithms in Garau and Vázquez [2018] is now modified, since we aim here at solving the parabolic problem of equation (2.7) by employing admissible adaptive discretizations.

2.4.1 Overview of the scheme

We are given an initial tensor-product mesh $\mathcal{Q}_0$, the corresponding truncated hierarchical B-spline space $\mathcal{T}_0$, an initial solution vector $\boldsymbol{\theta}_0$, a class of admissibility m, a maximum number of refinement levels N, and a tolerance tol. With such a set of initial parameters algorithm 1 returns an approximated solution of the problem defined in section 2.1 employing a backward Euler time integration scheme together with adaptive mesh refinement and coarsening procedures fulfilling the admissibility requirements. In this way, the algorithm allows to concentrate the computational efforts where the estimated errors are higher and, at the same time, to obtain an admissible mesh that gives the possibility to avoid undesired oscillations in the solution. The algorithm can be split, at each time step, into two separate parts: first, we refine the mesh iteratively, and, subsequently, we coarsen the mesh to generate the initial mesh for the next time step, and project the solution of the previous time step onto the coarsened space. These two parts are detailed in the following subsections.

Algorithm 1 `solve_heat_transfer_problem`

Input: $\mathcal{Q}_0$, $\mathcal{T}_0$, $\boldsymbol{\theta}_0$, m, N, tol
Output: $\boldsymbol{\Theta} := \{\boldsymbol{\theta}_0, \dots, \boldsymbol{\theta}_{t_{end}}\}$

1: $t \leftarrow 0$
2: $(\mathcal{Q}_{t+\Delta t}, \mathcal{T}_{t+\Delta t}, \varepsilon_{\mathcal{Q}}, \boldsymbol{\theta}_{t+\Delta t}) \leftarrow$`adpt_iter_refine`$(\mathcal{Q}_t, \mathcal{T}_t, \boldsymbol{\theta}_t, m, t, N, \text{tol})$ ▷ algorithm 2 (1^{st} time step)
3: $t \leftarrow t + \Delta t$
4: **while** $t < t_{end}$ **do**
5: $\quad(\mathcal{Q}_{t+\Delta t}, \mathcal{T}_{t+\Delta t}, \varepsilon_{\mathcal{Q}}, \boldsymbol{\theta}_{t+\Delta t}) \leftarrow$`adpt_iter_refine`$(\mathcal{Q}_t, \mathcal{T}_t, \boldsymbol{\theta}_t, m, t, 2, \text{tol})$ ▷ algorithm 2
6: $\quad\mathcal{M}_c \leftarrow$`mark_min`$(\varepsilon_{\mathcal{Q}}, \mathcal{Q}_{t+\Delta t})$ ▷ equation (2.10)
7: $\quad\mathcal{Q}_{t+\Delta t} \leftarrow$ `coarsen`$(\mathcal{Q}_{t+\Delta t}, \mathcal{M}_c, m)$ ▷ algorithm 5
8: $\quad(\mathcal{T}_{t+\Delta t}, \boldsymbol{\theta}_{t+\Delta t}) \leftarrow$ `project`$(\mathcal{Q}_{t+\Delta t}, \mathcal{T}_{t+\Delta t}, \boldsymbol{\theta}_{t+\Delta t})$ ▷ L_2 projection onto the coarsened space
9: $\quad t \leftarrow t + \Delta t$
10: **end while**

2.4.2 Refinement

Algorithm 1 at each time step calls the function `adpt_iter_refine` defined in algorithm 2 to adaptively refine the mesh and the corresponding function space. The `adpt_iter_refine` function returns a refined mesh and the corresponding function space together with the solution vector and the estimated error on the refined space. Algorithm 2 starts by solving

Algorithm 2 `adpt_iter_refine`

Input: $\mathcal{Q}^0$, $\mathcal{T}^0$, $\boldsymbol{\theta}_t$, m, t, I_{MAX}, tol
Output: $(\mathcal{Q}, \mathcal{T}, \varepsilon_{\mathcal{Q}}, \boldsymbol{\theta}_{t+\Delta t})$

$i \leftarrow 0$
$\Delta\boldsymbol{\theta}_{t+\Delta t} \leftarrow$`solve`$(\mathcal{Q}^i, \mathcal{T}^i, \boldsymbol{\theta}_t)$ ▷ equation (2.7)
$\boldsymbol{\theta}_{t+\Delta t} \leftarrow \boldsymbol{\theta}_t + \Delta\boldsymbol{\theta}_{t+\Delta t}$
$\varepsilon_{\mathcal{Q}} \leftarrow$`estimate`$(\boldsymbol{\theta}_{t+\Delta t}, \mathcal{Q}^i, \mathcal{T}^i)$ ▷ equation (2.8)
while $i \leq I_{\text{MAX}}$ & $\varepsilon_{\mathcal{Q}} \geq$ tol **do**
    $\mathcal{M}_r \leftarrow$`mark_max`$(\varepsilon_{\mathcal{Q}}, \mathcal{Q}^i)$ ▷ equation (2.9)
    $\mathcal{Q}^{i+1} \leftarrow$ `refine`$(\mathcal{Q}^i, \mathcal{M}_r, m)$ ▷ algorithm 3
    $(\mathcal{T}^{i+1}, \boldsymbol{\theta}_t) \leftarrow$ `project`$(\mathcal{Q}^{i+1}, \mathcal{T}^i, \boldsymbol{\theta}_t)$ ▷ knot insertion as described in [Garau and Vázquez, 2018, Sec. 4.3]
    $i \leftarrow i + 1$
    $\Delta\boldsymbol{\theta}_{t+\Delta t} \leftarrow$`solve`$(\mathcal{Q}^i, \mathcal{T}^i, \boldsymbol{\theta}_t)$
    $\boldsymbol{\theta}_{t+\Delta t} \leftarrow \boldsymbol{\theta}_t + \Delta\boldsymbol{\theta}_{t+\Delta t}$
    $\varepsilon_{\mathcal{Q}} \leftarrow$`estimate`$(\boldsymbol{\theta}_{t+\Delta t}, \mathcal{Q}^i, \mathcal{T}^i)$
end while
$\mathcal{Q} \leftarrow \mathcal{Q}^i$, $\mathcal{T} \leftarrow \mathcal{T}^i$

equation (2.7) on the mesh obtained in the previous time step $\mathcal{Q}^0$. Successively, the algorithm estimates the element error and marks a set of active elements to be refined

$$\mathcal{M}_r = \texttt{mark\_max}\left(\varepsilon_{\mathcal{Q}}(\theta_t, Q)_{Q\in\mathcal{Q}}, \mathcal{Q}\right), \tag{2.9}$$

following the so-called *Dörfler marking* (cfr. Dörfler [1996]), i.e. by considering a fixed refinement marking parameter $\alpha_r \in (0, 1]$ such that

$$\varepsilon_{\mathcal{Q}}(\theta_t, \mathcal{M}_r) \geq \alpha_r \varepsilon_{\mathcal{Q}}(\theta_t, \mathcal{Q}),$$

where θ_t is the discrete solution at time t.

The marked elements are then refined employing algorithms 3 and 4, previously introduced in Buffa and Giannelli [2016], see also Bracco et al. [2018b] for a more detailed explanation of these algorithms which generate admissible meshes. Note that the choice of the parameter m naturally influences the grading of the the hierarchical meshes.

Algorithm 3 `refine`

Input: $\mathcal{Q}$, $\mathcal{M}_r$, m
Output: $\mathcal{Q}^\star$

for $Q \in \mathcal{Q} \cap \mathcal{M}_r$ **do**
    $\mathcal{Q} \leftarrow$`refine_recursive`$(\mathcal{Q}, Q, m)$
end for
$\mathcal{Q}^\star \leftarrow \mathcal{Q}$

Algorithm 4 `refine_recursive`

Input: $\mathcal{Q}$, Q, m
Output: $\mathcal{Q}$

for $Q' \in \mathcal{N}_r(\mathcal{Q}, Q, m)$ **do**
    $\mathcal{Q} \leftarrow$`refine_recursive`$(\mathcal{Q}, Q', m)$
end for
if Q has not been subdivided **then**
    subdivide Q and
    update $\mathcal{Q}$ by replacing Q with its children
end if

Algorithm 2 is terminated when either a maximum number of iterations is reached or the estimated error $\varepsilon_{\mathcal{Q}}$ is below a certain tolerance tol. In particular, in this work we iterate the first time step until the maximum level of refinement N is achieved, while, for the remaining time steps, we set the maximum number of iterations equal to two, see the call to `adpt_iter_refine` (algorithm 2) on line 5 of `solve_heat_transfer_problem` (algorithm 1). This choice is justified by the small values of Δt that are generally used in AM simulations to discretize the problem in time. Even if for linear problems a different choice for the time step size and, then, for the stopping criteria could be made, we aim at developing and verify an algorithm suitable to be used in more complex AM applications. In these applications, in fact, the time step increments are necessarily very small due to the strong non linearity of the problem, therefore two consecutive meshes would not differ too much from each other.

At each iteration of algorithm 2 the temperature $\boldsymbol{\theta}_t$ at the previous time step must be written in terms of basis functions of the newly computed mesh. To guarantee the best accuracy this could be done as in line 8 of algorithm 1, by applying a projection of the (fine) solution of the previous time step onto the space associated with the new mesh, see the details in section 2.4.3. In view of the above considerations, and to save computational time, this projection is only applied onto the space defined on the coarse mesh $\mathcal{Q}^0$. For the refined meshes, instead of computing a new projection we use again the projection onto the coarse space associated to $\mathcal{Q}^0$, and to obtain its expression in terms of the basis functions of the refined space we take advantage of the nestedness of the spaces, using knot insertion as described in Garau and Vázquez [2018]. In other words, we always consider the temperature at the previous time $\boldsymbol{\theta}_t$ in the coarse mesh. In fact, with our choice we lose some accuracy each time we coarsen the mesh, but, since we employ very small time steps, this approximation remains acceptable as it will be shown in section 2.5.

2.4.3 Coarsening

In order to complete the time step routine we need to coarsen the hierarchical mesh, that will be used in the next time step. Also in this case we first mark a set of active elements to be coarsened

$$\mathcal{M}_c = \texttt{mark\_min}\left(\varepsilon_{\mathcal{Q}}(\theta_t, Q)_{Q\in\mathcal{Q}}, \mathcal{Q}\right), \tag{2.10}$$

fixing a coarsening marking parameter $\alpha_c \in (0, 1]$ and considering the elements with the lowest estimated error, such that

$$\varepsilon_{\mathcal{Q}}(\theta_t, \mathcal{M}_c) \leq \alpha_c \varepsilon_{\mathcal{Q}}(\theta_t, \mathcal{Q}).$$

The last step is the coarsening of the mesh, which is described in algorithm 5. An important issue is to decide, from the list of marked elements, the elements that should be reactivated. In principle, the parents of all marked elements could be reactivated. However, since coarsening implies a loss of information we have chosen to be conservative, and an element is reactivated only if all its children are marked. In other words, elements that are not marked will remain active. This is ensured by the first condition in line 6 of the algorithm. Moreover, to guarantee that the coarsened mesh fulfills the admissibility property, we perform one more check on the selected elements: the element can be reactivated only if the coarsening neighborhood is

empty, otherwise the admissibility condition would be violated, as we have explained in section 2.2.3. If the chosen element satisfies the two conditions, the last step, performed in line 7 of algorithm 5, updates the mesh by reactivating the element and removing its children.

Algorithm 5 `coarsen`

Input: $\mathcal{Q}$, $\mathcal{M}_c$, m
Output: $\mathcal{Q}$

1: **for** $Q \in \mathcal{M}_c$ **do**
2: $\quad \mathcal{R}_c \leftarrow \mathcal{R}_c \cup$ `get_parent`(Q)
3: **end for**
4: **for** $Q \in \mathcal{R}_c$ **do** ▷ This loop must be done from the finest to the coarsest level
5: $\quad Q_c \leftarrow$ `get_children` (Q)
6: $\quad$ **if** $(Q_c \subset \mathcal{M}_c \ \ \& \ \ \mathcal{N}_c(\mathcal{Q}, Q, m) = \emptyset)$ **then**
7: $\quad\quad$ update $\mathcal{Q}$ by activating Q and removing its children Q_c
8: $\quad$ **end if**
9: **end for**

Once the mesh is coarsened, we need to project the solution from the fine space onto the coarse one, and in this work we have chosen to do it by using a global L^2 projection. With a similar notation to the one used in section 2.3.1, with the c, f subindices referring to coarse and fine spaces, respectively, the L^2 projection is computed as the solution of the linear system

$$\mathbf{M}_c \boldsymbol{\theta}_{t,c} = \mathbf{b}, \text{ with } \mathbf{M}_c = \int_\Omega \mathbf{N}_c^T \mathbf{N}_c d\Omega \text{ and } \mathbf{b} = \int_\Omega \mathbf{N}_c^T (\mathbf{N}_f \boldsymbol{\theta}_{t,f}) d\Omega.$$

Other alternatives to compute the projection with local operators are given by the quasi-interpolant in Speleers and Manni [2016], or the Bézier projection as presented in Lorenzo et al. [2017].

We remark that the coarsening algorithm for THB-splines that we propose differs from other algorithms presented in previous papers. In particular, in Hennig et al. [2018] a global *a posteriori* check for the admissibility of the mesh is performed after coarsening, which may cause to refine again reactivated elements. In our algorithm this check is local and performed before reactivating the elements. This guarantees an *a priori* automatic control which saves computational time. In Lorenzo et al. [2017] the admissibility condition is replaced by a similar concept, that the authors call *function support balancing*, that also guarantees a certain grading of the mesh. As we will see in the numerical tests of section 2.5, the condition of admissibility maintains the same accuracy as the function support balancing, while the obtained refinement is more local for the former, which leads to spaces with many less degrees of freedom.

2.5 Numerical examples

2.5.1 2D Benchmarks

Two numerical examples are discussed in the following section. In the first example, defined by a Gaussian heat source tavelling on a circular arc scan track, we compare the solution

obtained using an admissible hierarchical mesh with the ones computed employing uniform refinement, non-admissible hierarchical refinement and the function support balancing algorithm introduced in Lorenzo et al. [2017]. The second example consists of a Gaussian heat source traveling on a multi-track source path. In this case we investigate the ability of the presented admissible adaptive scheme to capture the influence of adjacent scan tracks on the temperature evolution. Again we compare the solution of the admissible adaptive mesh with respect to the results obtained with uniform and non-admissible adaptive refinement. In both the examples we use standard Gauss integration to numerically approximate the integrals of equation (2.6) and we set the admissibility parameter m equal to 2. The results are obtained using GeoPDEs (cfr. de Falco et al. [1 12]; Vázquez [2016]), a MATLAB® toolbox which implements, beside classical tensor product IGA, also adaptive hierarchical discretizations Bracco et al. [2018b]; Garau and Vázquez [2018], on an Intel® Core™ i7-6700, CPU@3.40GHz, RAM 24Gb.

Circular arc scan track

The first example consists of a Gaussian heat source traveling along a circular arc on a 10×10 mm^2 surface domain, as described in figure 2.3. The external heat source function f is modeled using a Gaussian function defined as:

$$f = \mathrm{P}\eta \exp\left(-\left((x - x_0)^2 + (y - y_0)^2\right)/r_h^2\right), \tag{2.11}$$

where P is the heat source power, η the absorptivity of the material, r_h the heat source spot radius, while (x_0, y_0) is the position of the source at a given instant in time. In table 2.1 the values adopted for the process and the material model parameters are reported. In this first example we aim at comparing different discretization techniques without focusing on the real physics of the process, justifying in such a way the choice of simple unitary values for the material parameters.

Parameters	**Values**
Laser power P	9×10^5[W]
Laser speed	1.57 [mm/sec]
Absorptivity η	0.33
Source radius r_h	100 [μm]
Conductivity k	1.0 [W/mm/K]
Specific heat capacity C_p	1.0 [J/kg/K]
Density ρ	1.0 [kg/mm^3]
Initial temperature θ_0	20.0 [°C]

Table 2.1: Circular arc scan track: Process and material parameters.

For such a problem we generate an overkill solution obtained with B-spline of degree 4 defined on $2^9 \times 2^9$ isogeometric tensor-product elements, while adaptive IGA discretization starts from a single knot span and is recursively bisected towards the regions with the highest error, as indicated by the error estimator defined in equation (2.8) choosing $\alpha_r = 0.1$ and $\alpha_c = 0.25$.

Figure 2.4 (right) shows the relative error in the internal energy norm ε_i with respect to the reference solution for two different cubic admissible adaptive discretizations with seven and

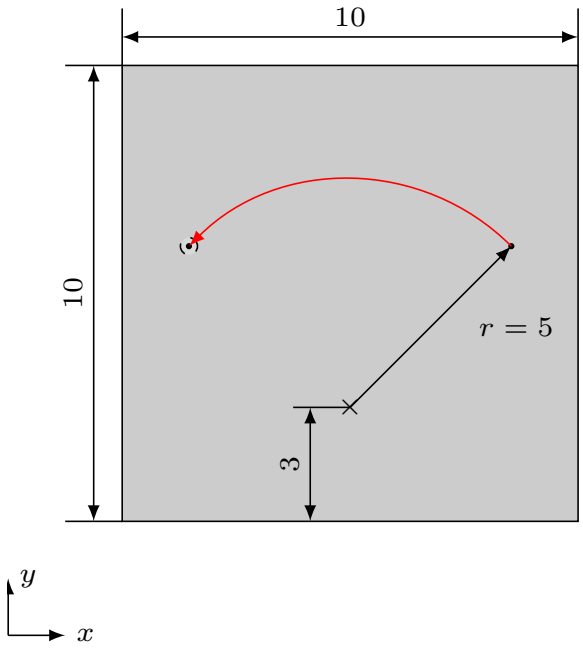

Figure 2.3: Circular arc scan track: Heat source moving on a circular arc, the red arrow indicates the scan path (all distances are in mm).

eight levels of refinement (adm. adap. $l = 7$ and adm. adap. $l = 8$) and their corresponding uniform meshes (unif. $2^6 \times 2^6$ and unif. $2^7 \times 2^7$), i.e. uniform meshes with elements of the same size of the smallest element in the adaptive mesh. It can be observed that the relative errors of the adaptive and the uniform discretization are almost identical for both cases, whereas, as shown in figure 2.4 (left), the adaptive schemes require almost two orders of magnitude less DOFs compared to uniform IGA meshes. We want to stress the fact that this difference increases together with the maximum refinement level, i.e. the more localized is the problem the smaller is the resulting linear system (and thus the memory consumption) compared to the uniform case for the same level of accuracy. A similar behavior can also be observed in figure 2.5, where the CPU time of the admissible adaptive discretization decreases considerably compared to the corresponding uniform discretization when the maximum level of refinement increases.

Finally, we investigate the behavior of the proposed algorithm with respect to the choice of the admissibility class m, defined in section 2.2.3. We also compare the obtained results with the ones for non-admissible grids, and for the function support balancing algorithm with the function support balancing parameter set to 1 (for further details see Lorenzo et al. [2017, Sec. 7]). To this end, we decrease the refinement Dörfler parameter α_r to 0.059 in the non-admissible case such that we can obtain a mesh with 8 levels of refinement at each time step also for this grid, which otherwise (keeping $\alpha_r = 0.1$) would return a coarser grid than the admissible one using the same number of time steps. Obviously, the same result for non-admissible meshes can also be obtained increasing the maximum number of iterations, but we prefer to modify the Dörfler parameter in an effort to obtain a fair comparison between the different discretizations.

Figure 2.6 presents the comparison between the four different cases in terms of total number

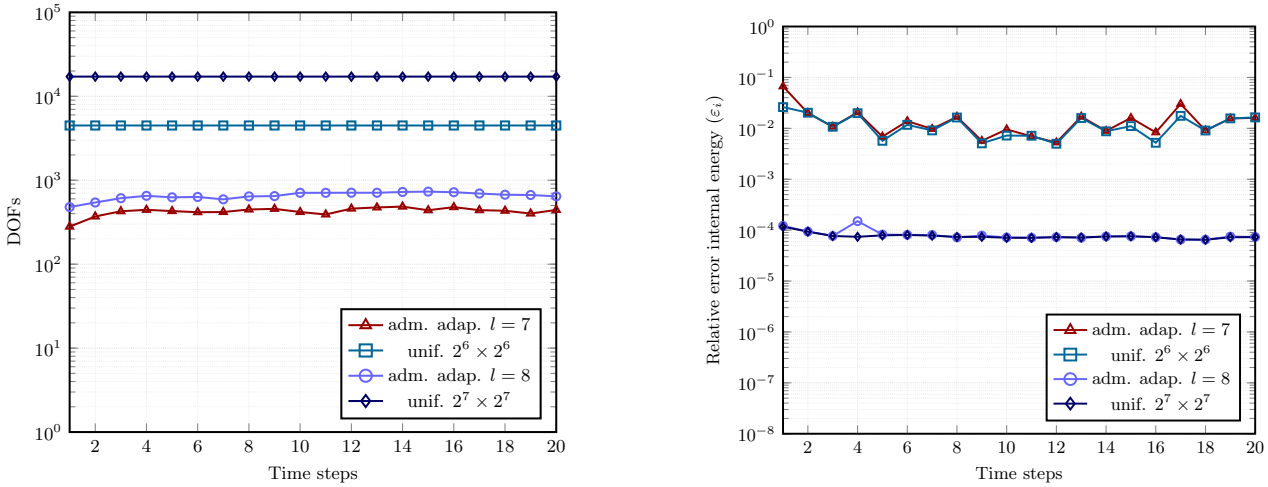

Figure 2.4: Circular arc scan track: DOFs (left) and relative errors (right) comparison at each time step for different levels of refinement using adaptive THB-splines and uniform tensor-product meshes.

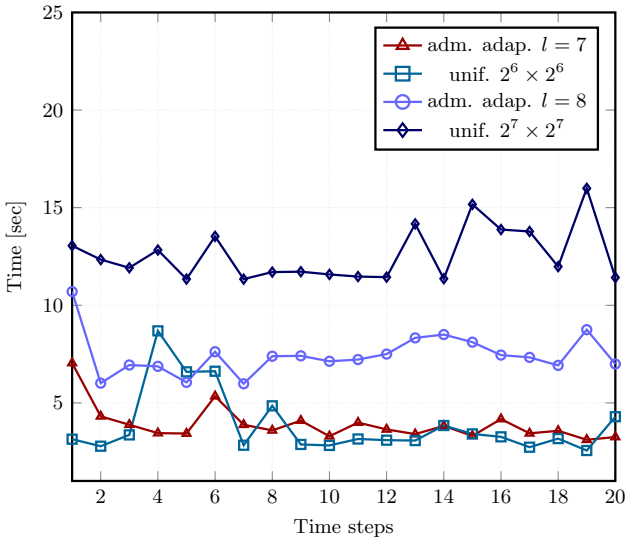

Figure 2.5: Circular arc scan track: CPU time comparison at each time step for different levels of refinement using adaptive THB-splines and uniform tensor-product meshes.

of DOFs and relative error at each time step, respectively. We can observe that both the function support balancing and the admissible adaptive discretization with $m = 2$ reach the same level of accuracy, while the non-admissible grid and the admissible discretization with $m = 3$ have a non constant behavior and present in many time steps a much higher error. We notice that increasing the parameter m reduces the number of DOFs, but it strongly affects the accuracy of the solution. Instead, the function support balancing provides the same accuracy than the admissible adaptive scheme with $m = 2$, but with a higher number of DOFs. Figure 2.7 reports the temperature distribution at different time steps using admissible grids, in this case we cannot graphically observe any substantial difference between the admissible and non-admissible results which is instead captured when we look at the relative energy error

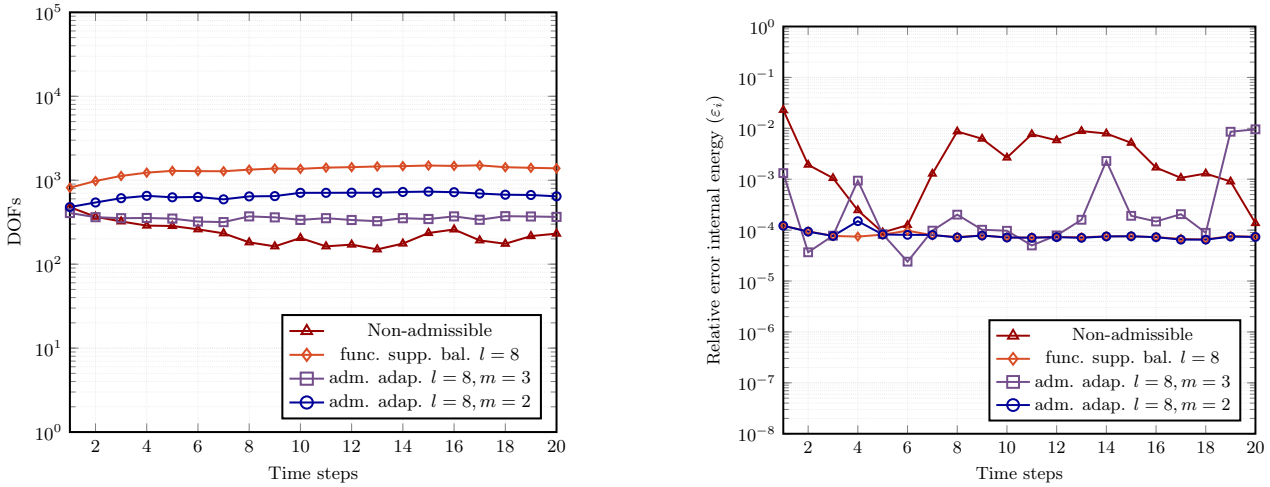

Figure 2.6: Circular arc scan track: DOFs (left) and relative errors (right) for the admissible adaptive mesh with $m = 2$ and $m = 3$, the function support balancing [Lorenzo et al., 2017] and a non-admissible mesh.

of figure 2.6. In any case we can observe how the steep temperature gradients in the proximity of the laser spot can be optimally captured by means of high-order and highly continuous approximation schemes, while the locality of the solution naturally calls for an adaptive discretization. The comparison of figure 2.8 between admissible and non-admissible grids shows that we obtain much more graded meshes if admissibility requirements are matched. We can conclude that the proposed algorithm leads to an excellent trade-off between accuracy and number of DOFs (and consequently memory consumption and computational efficiency). In fact, we obtain an error comparable with the uniform grid drastically reducing the total number of DOFs, while the function support balancing algorithm leads to a similar accuracy but with almost two times more DOFs per time step. Finally, we want to remark that we observe a similar behavior in terms of DOFs per time step also for hierarchical meshes with a higher degree.

Alternate scan directions

In this second example we consider a moving heat source traveling along multiple, adjacent, 8 mm long tracks in alternate directions on a surface of 10×10 mm^2, as depicted in figure 2.9. The external heat source is again defined using the Gaussian distribution of equation (2.11), but here we consider a two times smaller radius. This scale ratio (between the domain and the heat source radius) is close to the typical one we can find in LPBF applications. We set the laser scan distance between two consecutive tracks (hatch distance) equal to the laser radius, this is a typical choice in LPBF processes since it avoids gaps between solidified material regions. For this example we set $\alpha_r = 0.08$ and $\alpha_c = 0.25$, while the other problem parameters are reported in table 2.2.

We now compare an admissible adaptive mesh with 9 levels of refinement (adm. adap. $l = 9$) with respect to a non-admissible adaptive mesh with the same maximum level of refinement (non-adm. adap. $l = 9$) and the corresponding uniform mesh (unif. $2^8 \times 2^8$). Analogously to what we did in the previous section, we set a different Dörfler parameter for the non-admissible

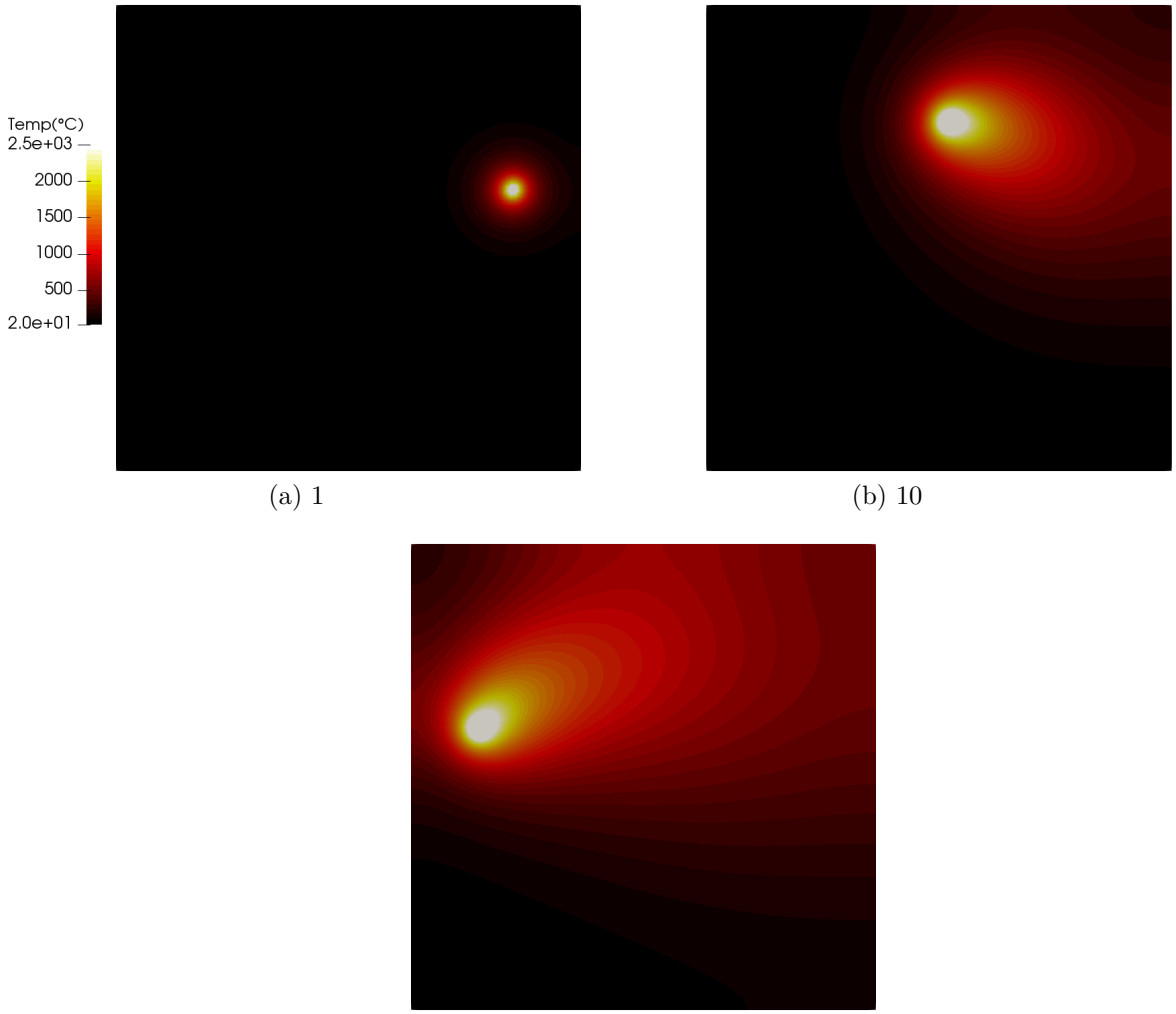

(a) 1 (b) 10

(c) 20

Figure 2.7: Circular arc scan track: Evolution of the temperature distribution for admissible meshes with $m = 2$ at time steps 1, 10 and 20.

discretization ($\alpha_r = 0.07$). Figure 2.10 shows the CPU time and the total number of DOFs at each time step for three considered grids. We can observe that, compared to the uniform mesh, in both cases we obtain a remarkable advantage when employing an adaptive mesh. This improvement in terms of both DOFs and CPU time is not affecting the quality of the solution and it is considerably higher than in the previous example due to the higher refinement level required to capture a more localized heat source. In fact, as shown in figure 2.11, the values of both the internal and the total energy at each time step do not present any substantial difference between the uniform and the admissible adaptive case. On the other side, when we adopt a non-admissible mesh, the internal energy value strongly oscillates from the reference value, while we have a limited advantage in terms of both CPU time and number of DOFs compared to the admissible mesh.

Finally, figures 2.12 and 2.13 report the temperature distributions and the corresponding discretizations at different positions of the heat source along the path, comparing admissible and non-admissible results. We note that, even if the solution is extremely localized, the

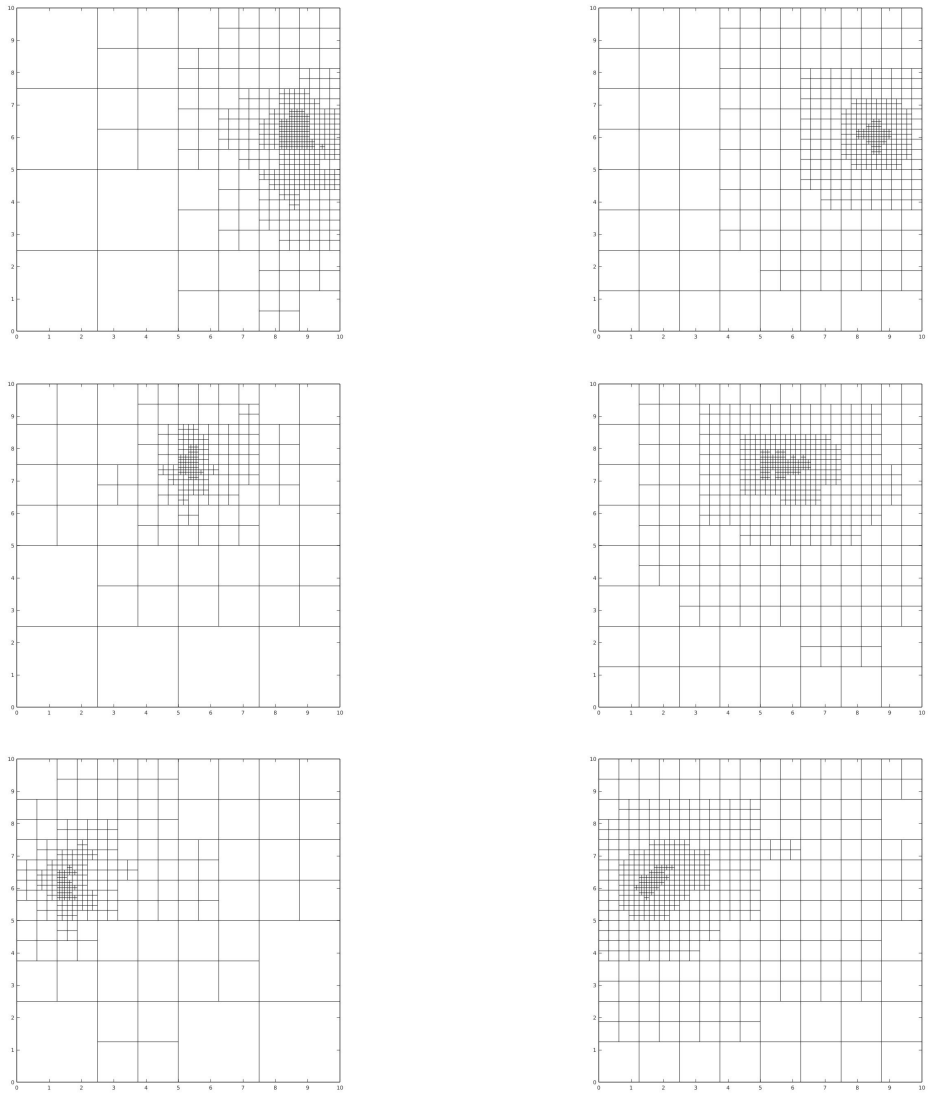

Figure 2.8: Circular arc scan track: Evolution of the non-admissible (left) and admissible with $m = 2$ (right) adaptive meshes at time steps 1, 10, 20 (from top to bottom).

admissible adaptive scheme allows to avoid any undesired oscillation in the solution, while this feature is not maintained throughout the entire simulation when we adopt a non-admissible discretization. In particular, see the solution at time steps 40 and 330 in figure 2.12.

2.6 Summary and further outlooks

We introduced a complete set of algorithms to perform admissible refinement and coarsening using THB-splines, and we successfully applied it to solve heat transfer problems with a moving heat source. The numerical examples clearly show the advantages of the presented admissible adaptive discretization, in terms of both memory consumption and computational efficiency, with respect to uniform IGA mesh with the same level of accuracy. Moreover, we demonstrated the importance of employing admissible meshes for these kinds of problems in

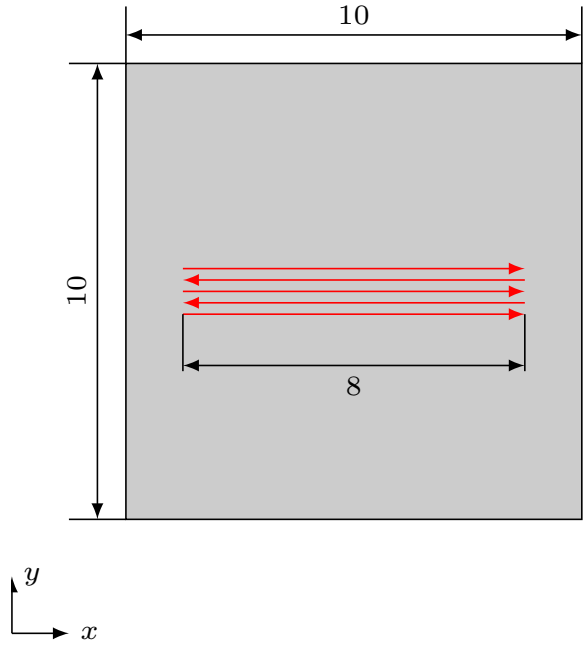

Figure 2.9: Alternate scan directions: Heat source moving on multiple adjacent tracks (in red) with alternate directions.

order to avoid undesired oscillations which might lead to nonphysical results. We also observed that the proposed algorithms lead to an excellent trade-off between the accuracy of the numerical results and the total number of DOFs of the system, showing better performances compared to other schemes with different refinement and coarsening algorithms, with or without taking into account grading parameters. Finally, the error estimator, together with a robust admissible discretization, is able to capture the influence of multiple adjacent tracks on the final temperature distribution, matching one of the main requisites required by LPBF applications. As further outlooks of the presented results, we plan to extend the application of the presented discretization to 3D, non linear, and multi-physics problems in order to efficiently perform reliable simulations of AM processes.

Parameters	**Values**
Laser power P	190[W]
Laser speed	0.8 [m/sec]
Absorptivity η	0.33
Laser radius r_h	50 [μm]
Conductivity k	29.0×10^{-3} [W/m/K]
Specific heat capacity C_p	650.0 [J/kg/K]
Density ρ	8440.0 [kg/m^3]
Initial temperature θ_0	25.0 [°C]
Hatch distance	50 [μm]

Table 2.2: Alternate scan directions: Process and material parameters.

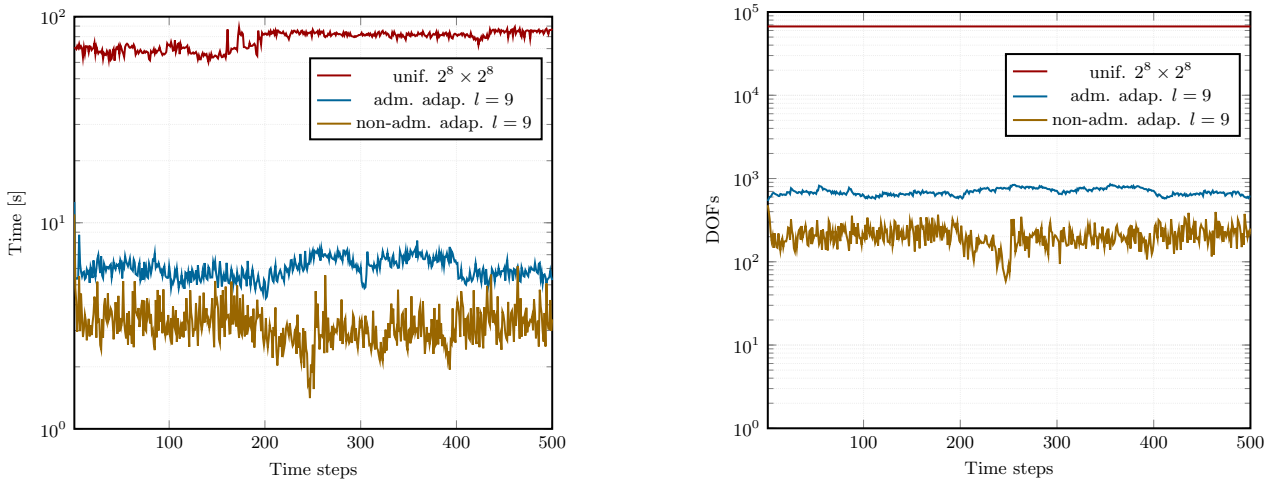

Figure 2.10: Alternate scan directions: CPU time (left) and DOFs (right) comparison at each time step between uniform, admissible and non-admissible adaptive meshes with 9 levels of refinements.

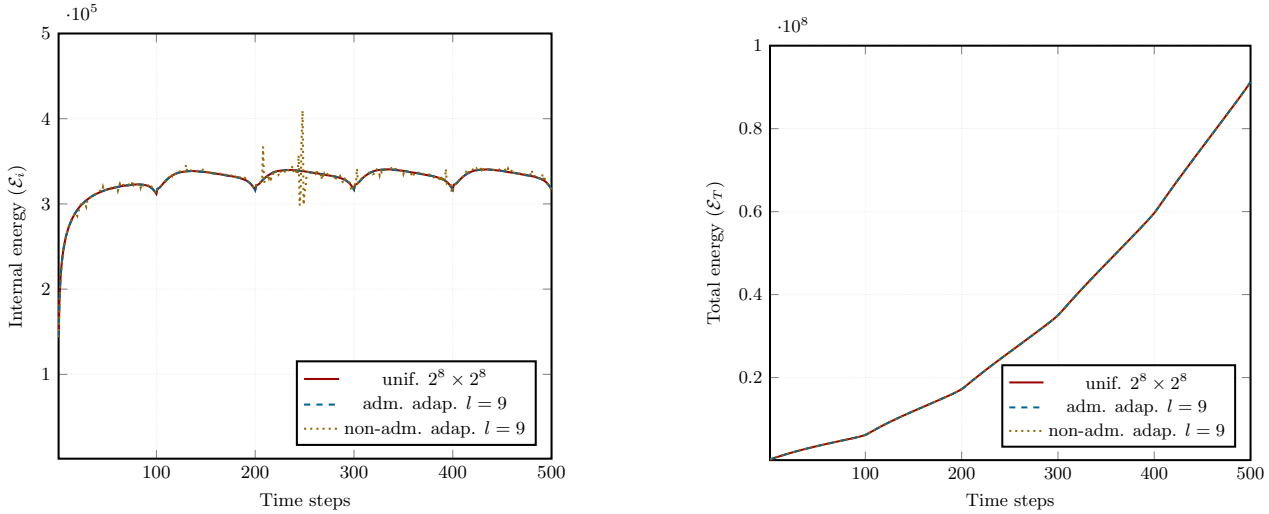

Figure 2.11: Alternate scan directions: Internal (left) and total (right) energy of the system at each time step between uniform, admissible and non-admissible adaptive meshes with 9 levels of refinements.

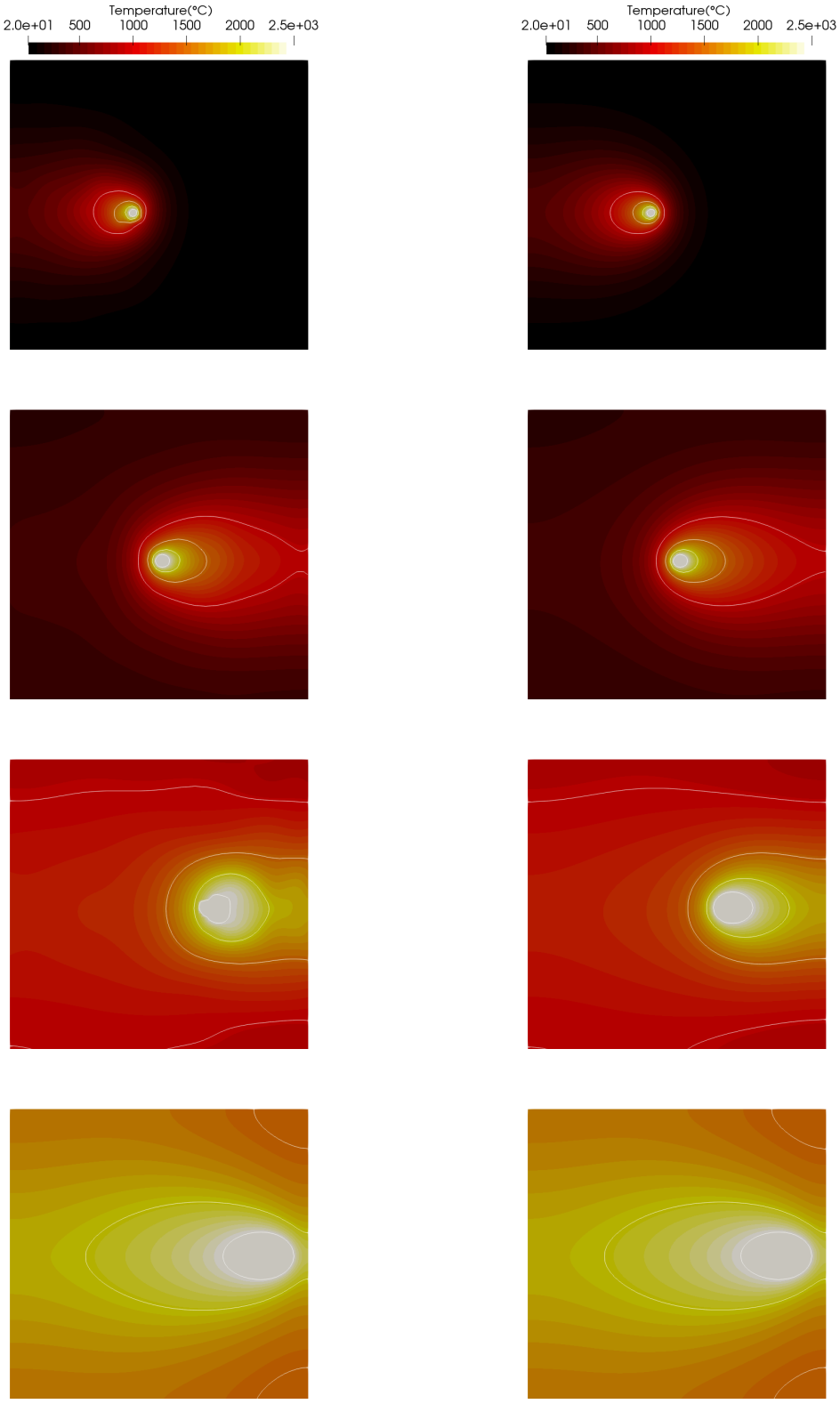

Figure 2.12: Alternate scan directions: Evolution of the non-admissible (left) and admissible (right) temperature distributions at time steps 40, 150, 330, and 500 (from top to bottom) with contour lines at 1000, 1500, 2000 and 2500°C.

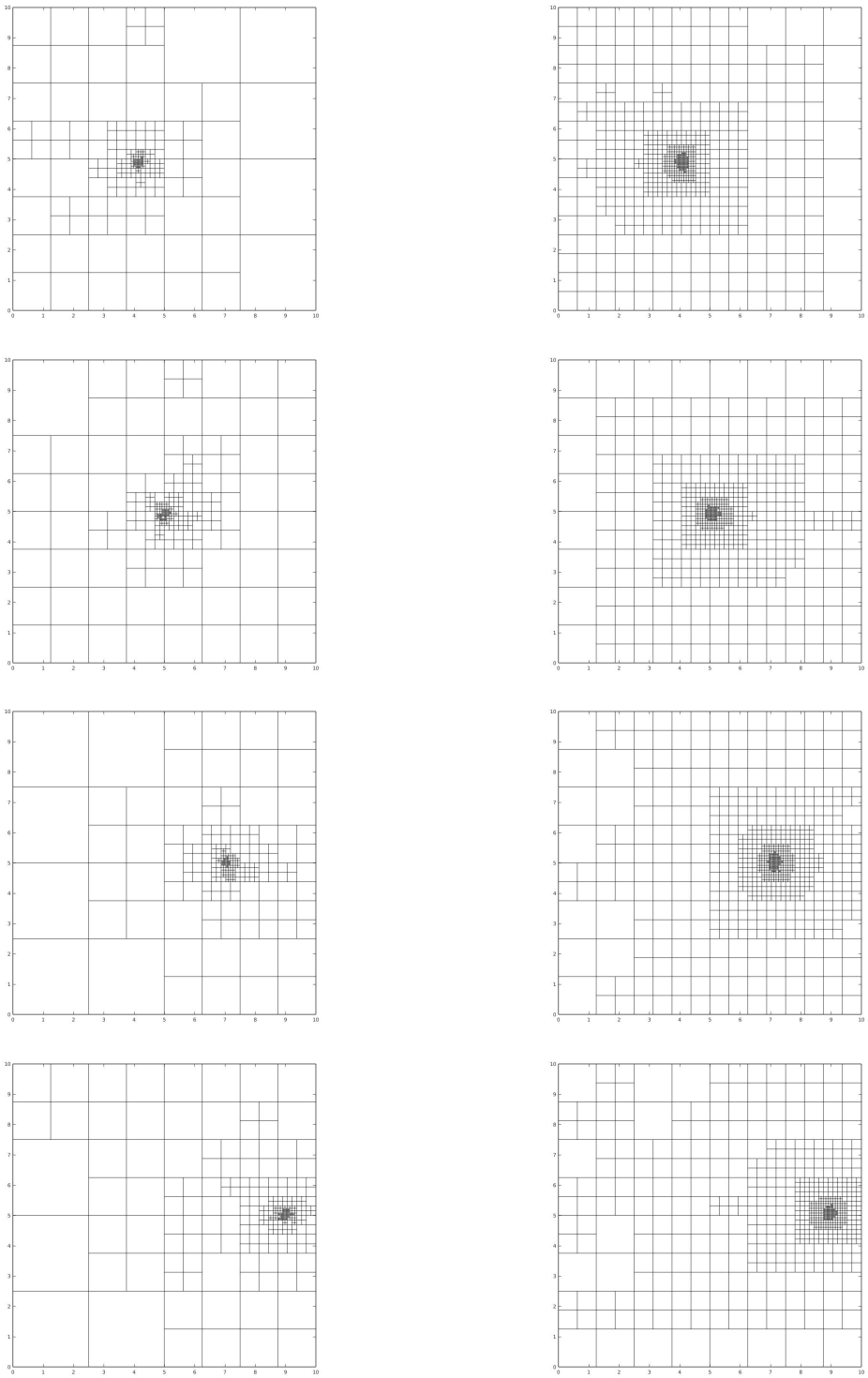

Figure 2.13: Alternate scan directions: Evolution of the non-admissible (left) and admissible (right) adaptive meshes at time steps 40, 150, 330, and 500 (from top to bottom).

Chapter 3

Numerical Modelling and Experimental Validations

The shape and thermal history of the melt pool are key ingredient to determine the physical properties of an artifact generated through a welding process. Therefore, the prediction of weld pool dynamics has been a subject of intensive research in the last decades in both the experimental and the numerical modeling community of welding; e.g., recent reviews of this subject are provided in Fotovvati et al. [2018]; Svenungsson et al. [2015]. Furthermore, it is fundamental to observe that process-structure-property relationships are also tightly interlinked and strongly determined by the characteristics of the weld pool in laser LPBF technologies (see e.g., Smith et al. [2016]). Therefore, an accurate thermal analysis is a key ingredient in the numerical simulations and predictions of LPBF processes as well.

To this end, many physical models have been proposed to obtain accurate and reliable numerical approximations of melt pools. Although different in scale, the basic phenomena in LPBF technology are similar to those in arc welding processes, see Goldak and Akhlaghi [2005]; Lindgren [2007]; Tanaka [2004] for an overview. Recent summaries more specific to LPBF processes are published in Megahed et al. [2016]; Schoinochoritis et al. [2017]; Smith et al. [2016].

While particle based models [Khairallah et al., 2016] as well as Lattice Boltzmann type approaches [Körner et al., 2011] exist, most common are continuum models based on the conservation of mass, momentum and energy [Yan et al., 2018]. Continuum approaches allow for modeling the transient evolution of primal variables (temperatures, pressures, and velocities) taking into account a large number of effects, such as the convection inside the melt pool, also including the one caused by a gradient in the surface tension (Marangoni effect as well as capillary effects), vaporization, momentum losses in mushy zones due to porous media effects, etc.

All these models may deliver very accurate results, but the more effects they include, the more computational power they require. Additionally, the abundance of models comes along with a wealth of parameters: these may be material viscosity, density, thermal conductivity and capacity, latent heat, etc., most of which show a non-negligible temperature dependence, such that their accurate, experimental determination may be both crucial and critical. Further modeling parameters, such as emissivity or absorptivity or even the geometry of powder particles, may come into play and they can be introduced in the model as boundary or ini-

tial conditions. However, accurate measurements of many of the listed parameters are not publicly available. This is even true for the most basic parameters, such as heat capacity or thermal conductivity, that are not published for the temperatures involved in metal based LPBF processes. All this drought of information results in the fact that even the evaluation of several parameters may itself often rely on models which, in turn, need to be calibrated against further observations.

The dilemma of choosing a correct model for the case of limited data is an important issue in statistics. As an example, George Box [Box, 1976] stated, somewhat drastically in his well known aphorism, that all models are wrong and that, therefore, the most complicated model is not necessarily the best. Instead, it is recommended to follow the lines of William of Occam, in which an economical description of the observations is sought which 'is as simple as possible, but not simpler'.

Following this line of thought, in Kollmannsberger et al. [2019] we introduce and validate an economical model able to replicate the results obtained by the benchmark measurements of a single line laser stroke on a bear metal plate of IN 625 published in www.nist.gov/ambench [2018]. In this chapter, an extended version of the model and results discussed in Kollmannsberger et al. [2019] is presented.

3.1 Governing equations

We use a non-linear heat transfer equation as a physical model to describe the evolution of temperature $T = T(t, \mathbf{x})$ as a function of space and time. Given a spatial domain Ω and a time interval $\mathcal{T} = [0, t_{end})$, the heat transfer equation can be written as follows:

$$\rho c \frac{\partial T}{\partial t} + \rho L \frac{\partial f_{pc}}{\partial t} - \nabla \cdot (k \nabla T) = 0 \qquad \text{in} \quad \Omega \times \mathcal{T}. \tag{3.1}$$

Therein ρ and L describe the density and the latent heat of the material, $c = c(T, \mathbf{x})$ and $k = k(T, \mathbf{x})$ are the temperature dependent heat capacity and thermal conductivity of the material, while $f_{pc} = f_{pc}(T)$ is the phase-change function describing the solid-to-liquid phase transition of the material. Therefore, beside the non linear contribution of the heat capacity and thermal conductivity, the latent heat term of equation (3.1) introduces a further nonlinearity into the problem.

Equation (3.1) is completed by the initial condition at time $t = 0$:

$$T(\mathbf{x}, 0) = T_0 \qquad \text{in} \quad \Omega, \tag{3.2}$$

as well as Neumann boundary conditions:

$$k \nabla T \cdot \mathbf{n} = q^r + q^l \qquad \text{on} \quad \Gamma_N \times \mathcal{T}. \tag{3.3}$$

Herein, T_0 is the initial temperature of the body, $\mathbf{n}$ is the unit normal vector, q^l is the heat flux input and q^r is the radiation boundary condition defined as:

$$q^r = \sigma \epsilon \left(T^2 + T_e^2\right) \left(T_e^2 - T^2\right). \tag{3.4}$$

In equation (3.4) σ is the Stefan-Boltzmann constant, ϵ is the emissivity of the material, and T_e is the ambient temperature. In our model, convection boundary conditions are neglected. Further details, specifically the adopted finite element formulation, are provided in Celentano et al. [1994] and Kollmannsberger et al. [2018].

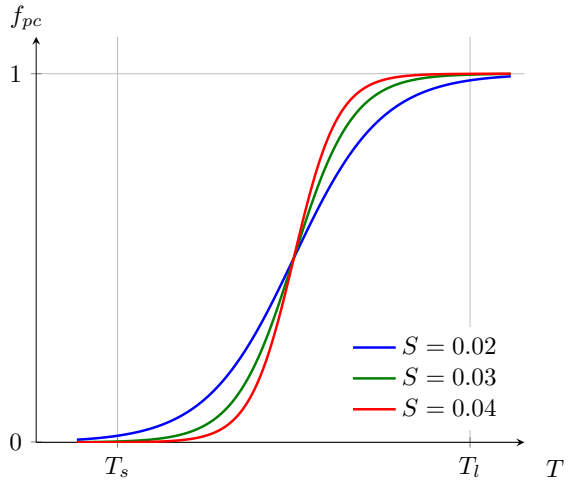

Figure 3.1: Phase change function for different values of the parameter S.

Phase-change model

For iso-thermal phase changes, the function f_{pc} exhibits a jump at the melting temperature T_m, as the temperature changes the material state from solid to liquid. Since the phase-change for metals is actually non-isothermal, we regularize this sudden jump between two temperatures: a solidification temperature T_s and a liquid temperature T_l, with $T_s < T_l$. We can now define the phase change function f_{pc}, such as:

$$f_{pc}(T) = \frac{1}{2}\left[\left(S\frac{2}{T_l - T_s}\left(T - \frac{T_s + T_l}{2}\right)\right) + 1\right], \tag{3.5}$$

where the parameter S in equation (3.5) is initially estimated such that the bulk of the phase change actually occurs between T_s and T_l (see Figure 3.1). Nevertheless, since this value cannot be measured, it requires calibration.

Heat flux model

In the sequel we consider two variants of the heat flux input q^l. The first variant is the double elliptical model introduced by Goldak et al. [1984] and depicted in figure 3.2. The front quadrant is defined by:

$$q^l = \frac{2P\eta f_f}{\pi a c_f}\exp\left(-2((z^{'} - z_0^{'})/c_f^2 + (x - x_0)/a^2)\right), \tag{3.6}$$

while in the rear quadrant it takes the form:

$$q^l = \frac{2P\eta f_r}{\pi a c_r}\exp\left(-2((z^{'} - z_0^{'})/c_r^2 + (x - x_0)/a^2)\right). \tag{3.7}$$

Herein, P is the laser power and η is the absorptivity of the material. The geometrical parameters $z_0^{'}$ and x_0 define the center of the laser beam on the upper surface at time t, while f_f and f_r are the fraction of heat deposited in the front and the rear quadrant respectively, which have the side condition that $f_r + f_f = 2$ (see [Goldak et al., 1984] for further details).

The second variant the heat source q^l which we consider in this work is not a model. In fact, q^l is directly provided to equation (3.3) as given by corresponding measurements.

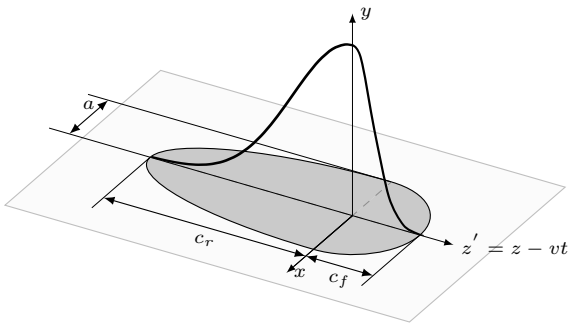

Figure 3.2: Goldak model for the heat flux input. The model consists in a double-ellipse on which a gaussian profile is defined.

3.2 Model Verification

The computational model was verified against the series of analytical or semi-analytical solutions defined in Kollmannsberger et al. [2018], where a multi-level *hp*-discretization was used. The computational model utilized in the present work is slightly different, as it uses the IGA discretization described in chapter 2, wherein multi-level Bézier extraction is applied to construct an efficient discretization which is refined locally in the vicinity of the laser beam. This implementation was verified in D'Angella et al. [2018] in two dimensions as well as in three dimensions using the same series of problems which were also used for the verification of the multi-level *hp*-basis in Kollmannsberger et al. [2018]. Since the focus of the present chapter is the validation of the model, we will not repeat these extensive verification studies. Instead, in the next section of this chapter, we will use the capabilities of the proposed discretization to directly evaluate the validity of the physical model given in section 3.1.

3.3 Model Validation

As a preamble to this section we want to highlight the fact that there are situations (e.g. the presence of highly complex phenomena, problem physics still unclear, model uncertainties and difficulties in ascertain its effectiveness, inability to measure all the model parameters) in which model validation must consist of two steps. In the first step (calibration step) the indeterminacy of the physical model is investigated and calibrated against a first set of experimental evidences; in the second step (validation step) the numerical results are compared against a different set of experimental evidences in order to define the range of validity and the robustness of the numerical model. The case under investigation is characterized by the inability to measure all the model parameters, in particular we have limited information on the absorptivity, emissivity, thermal conductivity and heat capacity of the material at high temperature, justifying the choice of the previously defined two-step model validation process.

In section 3.3.1 we will shortly describe and report the experimental benchmarks published in www.nist.gov/ambench [2018]. Following the previously described steps of the validation procedure, first, in section 3.3.2, we calibrate the isotropic model of section 3.1 using the

double ellipsoidal heat source introduced by Goldak et al. [1984] and then we validate the isotropic model using the two heat fluxes described in section 3.1. For the case in which an accurate measurement of the laser power distribution is given, we observe that the isotropic material assumption has a very limited range of validity. These findings serve as a motivation to extend the physical model by introducing anisotropic conductivities. This extended model is then presented in section 3.3.3 where it will be demonstrated that it predicts weld pool shapes with an improved accuracy.

3.3.1 Benchmark cases

All benchmark cases are thoroughly defined in the laser additive manufacturing benchmarks published in www.nist.gov/ambench [2018], including a detailed report on the measurements. The benchmarks are obtained through a traveling laser beam on a bare metal plate of nickel-based alloy IN625. The experimental quantities we will use to validate our model are: width,

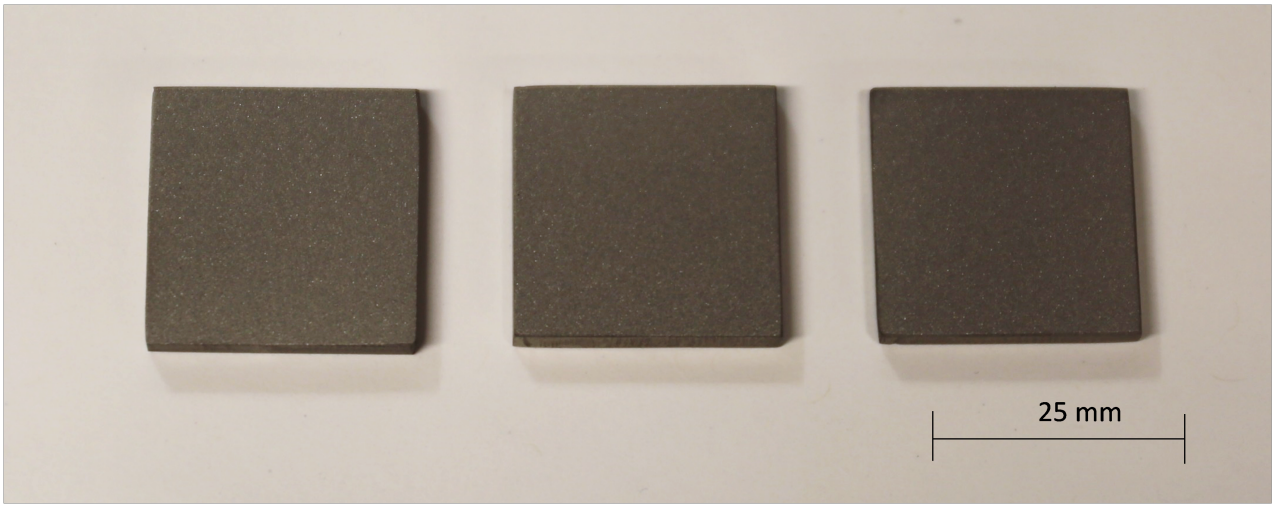

Figure 3.3: Bare plates of IN625 used for AMBench experiments. Courtesy of NIST.

length, and depth of the melt pool as defined in CHAL-AMB2018-02-MP of the above reference. We also report on the cooling rates defined in CHAL-AMB2018-02-CR, although they are not the primal focus in the work at hand. The experimental raw data for both melt pool and cooling rate are tabulated in appendix A. The benchmarks cited above and reported in www.nist.gov/ambench [2018] were performed on two different machines: an EOS M270, which in this work will be referred to using the designation commercial build machine (CBM) and the NIST-built additive manufacturing metrology testbed (AMMT) machine of figure 3.4. On each one of the two machines a set of ten measurements was carried out for three different cases (labeled A, B, and C), i.e. for varying laser power and speed. These cases are specified in table 3.1 for the CBM machine and table 3.2 for the AMMT machine. The averages of the experimental measurements for the CBM machine are reported in table 3.3, while average measurements for the AMMT machine are reported in table 3.4. In the CBM case the cooling rate is defined as:

$$CR_{CBM} = \frac{1290\,[^{\circ}\mathrm{C}] - 1000\,[^{\circ}\mathrm{C}]}{\Delta d[mm]} \times v\left[\frac{mm}{sec}\right],$$

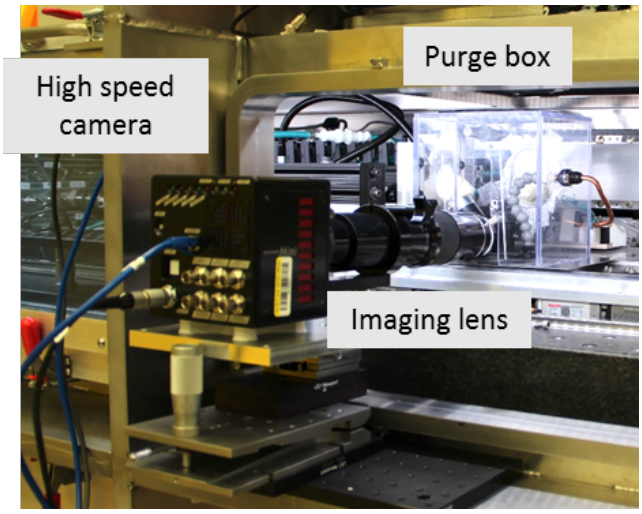

Figure 3.4: Additive Manufacturing Metrology Testbed (AMMT) and its thermography setup, which uses a long distance microscope and angled first-surface mirror mounted in an argon purge box. Courtesy of NIST.

Parameter values	A	B	C
laser power [W]	150	195	195
laser speed [mm/s]	400	800	1200
laser spot diameter $D4\sigma[\mu m]$	100	100	100

Table 3.1: CBM machine: parameter values.

with v laser speed and Δd distance in the direction of the laser path, while in the AMMT case as:

$$CR_{AMMT} = \frac{1290\,[°\mathrm{C}] - 1190\,[°\mathrm{C}]}{\Delta d[mm]} \times v\left[\frac{mm}{sec}\right].$$

For the exact definition of v and Δd, as well as for further details on the experimental benchmarks we refer to the original website which continues to be updated as further measurements become available www.nist.gov/ambench [2018].

3.3.2 Isotropic conductivity model

The calibration step of the isotropic model is carried out for case B on the CBM machine, as given in table 3.1, which is exactly the same configuration as case 7 in Ghosh et al. [2018]. The

Parameter values	A	B	C
laser power [W]	137.9	179.2	179.2
laser speed [mm/s]	400	800	1200
laser spot diameter $D4\sigma[\mu m]$	170	170	170

Table 3.2: AMMT machine: parameter values.

case	length $[\mu m]$	cooling rate $[\frac{^\circ C}{sec}]$
A	659	6.20×10^5
B	782	9.35×10^5
C	754	1.28×10^6

Table 3.3: CBM machine: experimental measurements according to www.nist.gov/ambench [2018], CHAL-AMB2018-02-MP.

case	length $[\mu m]$	width $[\mu m]$	depth $[\mu m]$	cooling rate $[\frac{^\circ C}{sec}]$
A	300	147.9	42.5	1.16×10^6
B	359	123.5	36	1.08×10^6
C	370	106	29.5	1.90×10^6

Table 3.4: AMMT machine: experimental measurements according to www.nist.gov/ambench [2018], CHAL-AMB2018-02-MP.

validation step is obtained comparing the calibrated model to the cases A, B and C of table 3.3 and table 3.4. For all the numerical simulations the IN625 material parameters are taken from literature (Mills [2002] and www.specialmetals.com [2019]) as reported in appendix B. It is noteworthy that material and process parameters, necessary to run the numerical simulation, are not experimentally available for the effective temperatures occurring in LPBF processes. For example, measurements of the thermal conductivity k is only available up to 871°C, but the melting range for IN625 is 1290-1350°C. Likewise, the melting temperature interval the value of k can only be extrapolated. It is important to note that this extrapolation itself represents a physical model which, in turn, needs to be calibrated. This circumstance is used in section 3.3.3 to better describe the conductivity of the material and, consequently, improve the accuracy of the predicted melt pool geometry. Further coefficients, whose measurements are only available up to a certain temperature, are the absorptivity η and the emissivity ϵ. The latter necessary to define the radiation boundary condition given in equation (3.3).

In case of the CBM machine, the benchmark defines the laser spot radius equal to $50\mu m$. We utilize this value for both parameters c_f and a of the double elliptical model (see figure 3.2). However, our model also contains the radius ratio c_r/c_f as a model parameter as well as the power fraction f_f/f_r. Both these parameters are additional, potential candidates to calibrate the physical model.

Model Calibration

Model calibration first requires to identify the sensitivities of the quantities of interest, i.e., length, width, depth, and cooling rate at the wake of the melt pool w.r.t. the modeling parameters η, ϵ, f_f/f_r and c_r/c_f given by the physical model presented in section 3.1. To this end, four studies were carried out, and for each study a single parameter is varied while

the others stay fixed. Figure 3.5 presents the variation of the length, width, depth, and

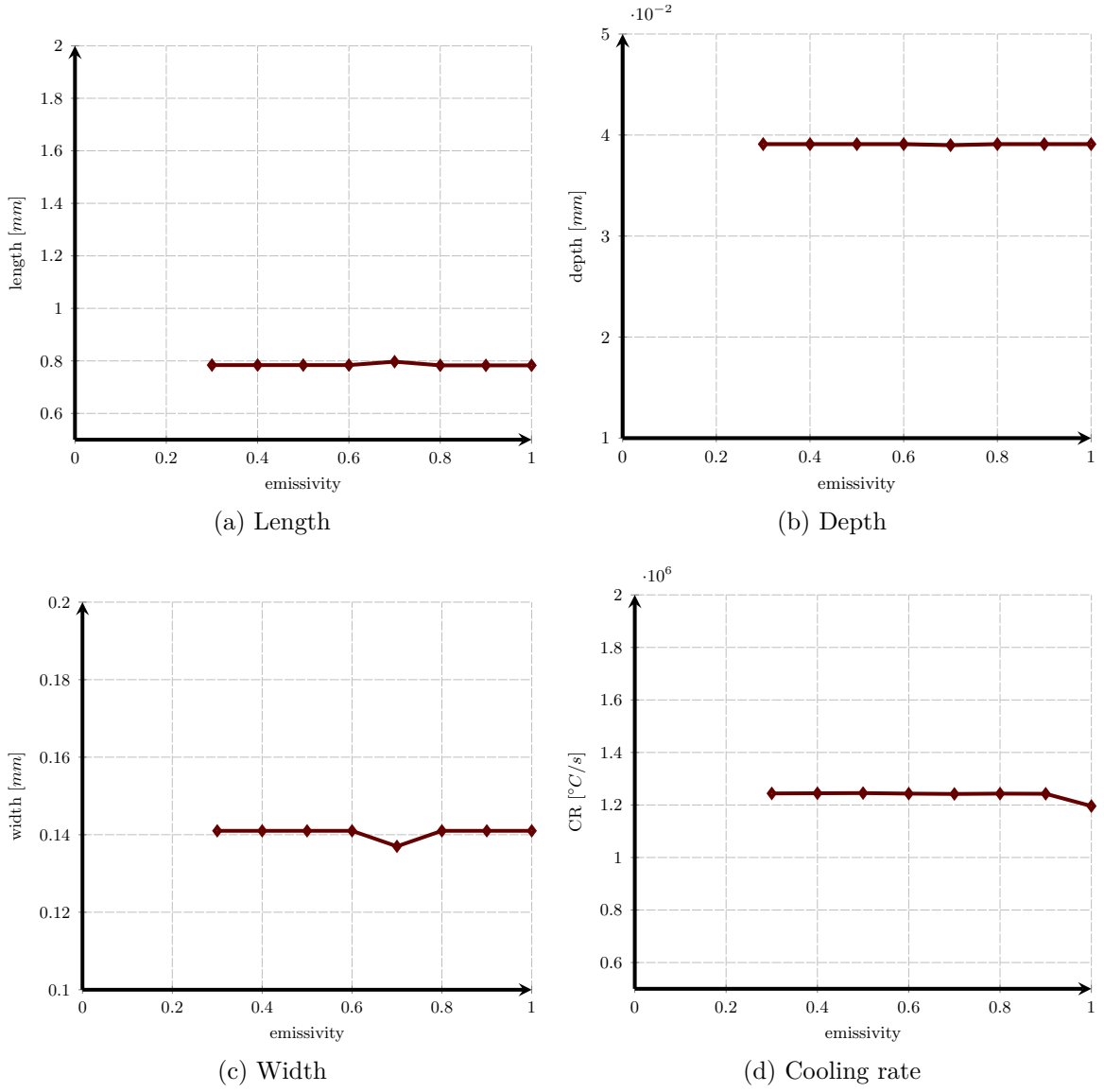

(a) Length (b) Depth

(c) Width (d) Cooling rate

Figure 3.5: CBM machine. Sensitivity studies w.r.t. the emissivity of the material ϵ.

cooling rate w.r.t. the emissivity values. The study clearly suggests that there is practically no influence of the emissivity on the quantities of interest. At first sight this result comes as a surprise because the model of the boundary conditions suggests an influence of fourth order in the temperature, something that for sure can not be neglected. Indeed, numerous authors explicitly include this boundary condition to obtain good results, see for example Lu et al. [2018] and the references cited therein. However, the investigation at hand considers the temperature directly under or in close vicinity to the laser and, therefore, the contribution of the radiation boundary condition is marginal. To illustrate this effect, we consider the flux caused by radiation at the melting temperature $T_m = 1290°\text{C} = 1563.15\text{K}$, with an ambient

temperature of $T_e = 20°\text{C} = 293.15\text{K}$. The corresponding power loss is

$$5.67 \times 10^{-8} \times 0.47 \left(T_m^2 + T_e^2\right)\left(T_e^2 - T_m^2\right) = 1.59 \times 10^5 \left[\frac{\text{W}}{m^2}\right] = 0.16 \left[\frac{\text{W}}{mm^2}\right], \tag{3.8}$$

which represents a negligible quantity compared to the peak power density of $q^l = 2.33 \times 10^4\,[W/mm^2]$ in the center of the laser beam. Clearly, under these conditions, radiation itself may be neglected for studies of temperature fields in close proximity to the laser source. To the contrary, the absorptivity has a large influence (see figure 3.6), as do the power fraction and the radius ratio, as depicted in figure 3.7 and figure 3.8, respectively. An iterative calibration delivers the final choice of the parameters: $\varepsilon = 0.47$, $\eta = 0.38$, $f_f/f_r = 0.053$ and $c_r/c_f = 0.167$.

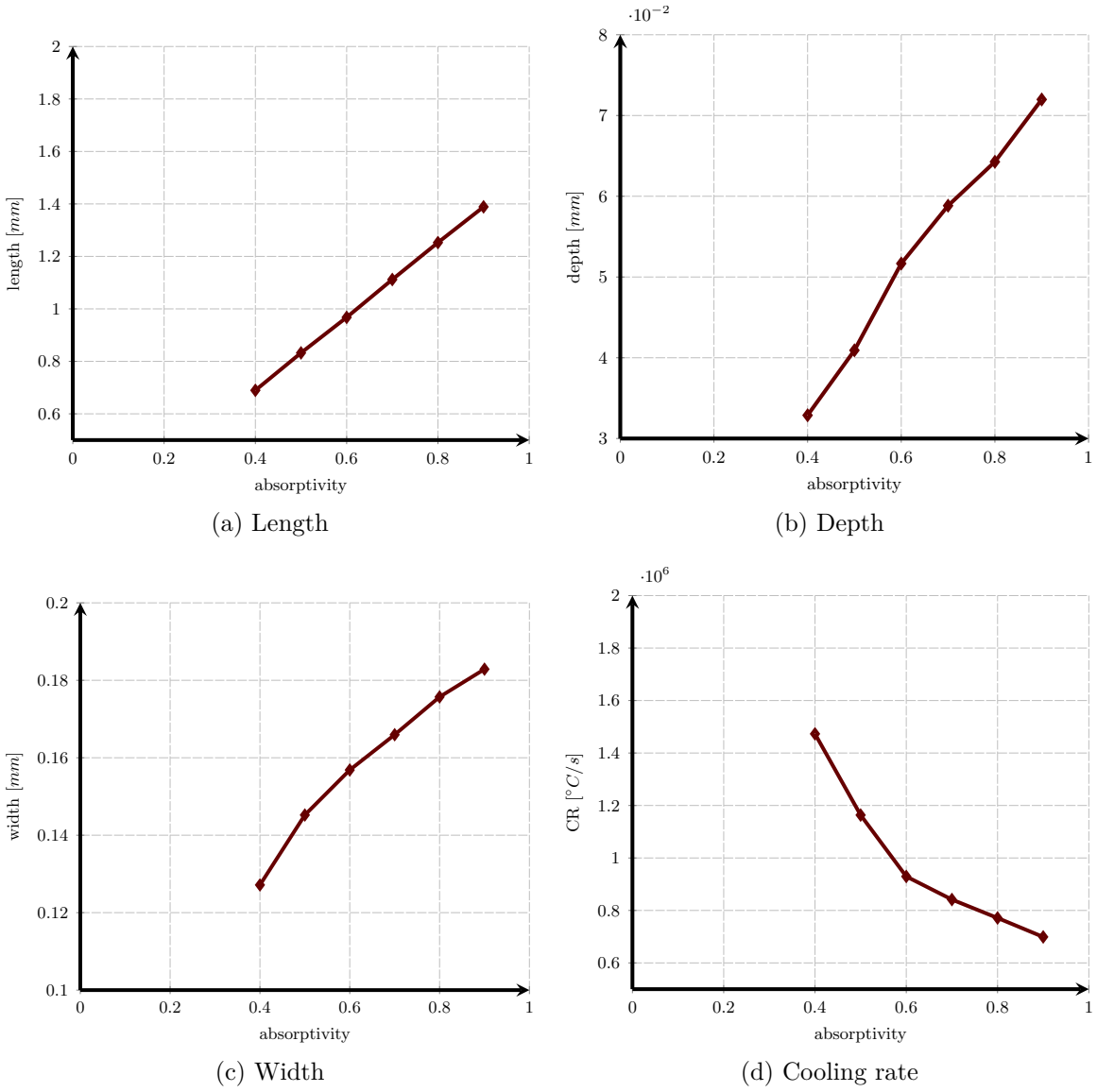

(a) Length

(b) Depth

(c) Width

(d) Cooling rate

Figure 3.6: CBM machine. Sensitivity studies w.r.t. the absorptivity of the material η.

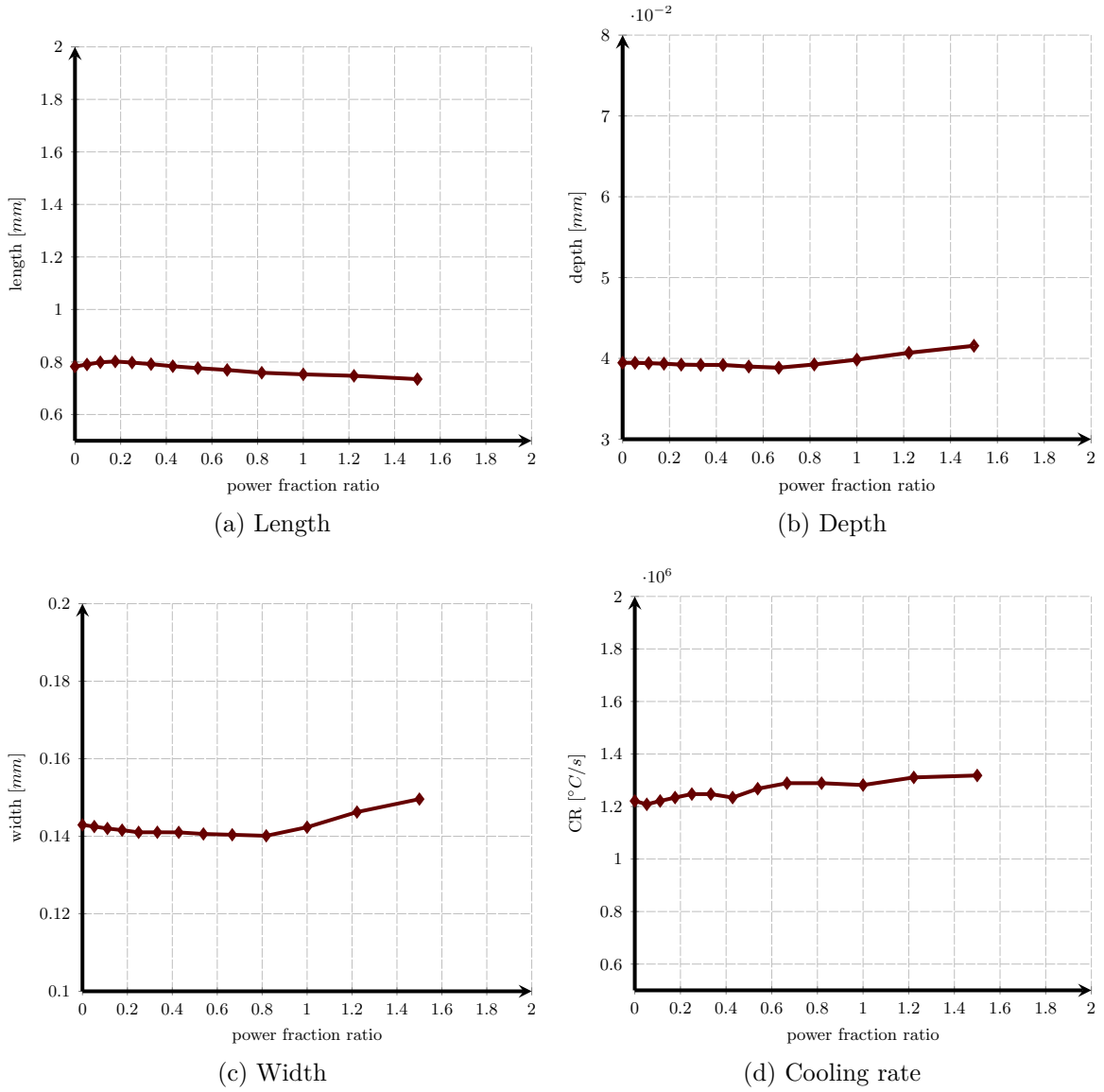

(a) Length (b) Depth

(c) Width (d) Cooling rate

Figure 3.7: CBM machine. Sensitivity studies w.r.t. the power fraction f_f/f_r.

Numerical results for calibration

Numerically computed temperature curves along the laser path are depicted in figure 3.9. The figure reports also the experimentally measured temperature, carried out using *in-situ* thermography, as described in Ghosh et al. [2018]. The different curves labeled $2mm$, $6mm$ and $12mm$ indicate at which position the zero of the abscissa of the plot coincides with the laser path. A steady state is reached already after only $2mm$. We specifically note that the calibration was carried out to best capture the temperature range around the melting temperature. Larger, even unphysical deviations, are tolerated outside this region. This kind of calibration towards a process window is justifiable not only due to the fact that merely the region of interest needs to be captured with accuracy by the computations, but also because

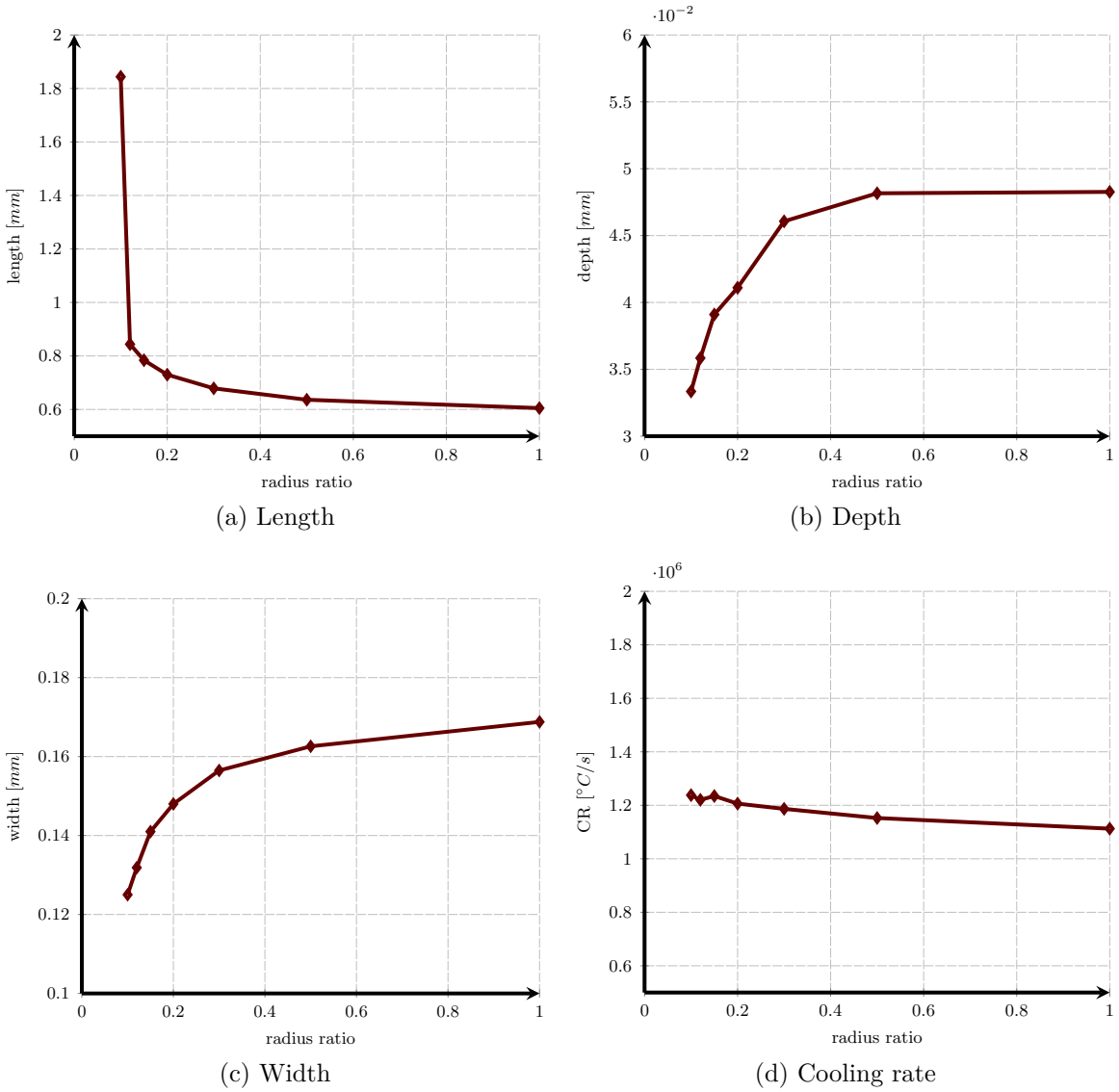

(a) Length (b) Depth

(c) Width (d) Cooling rate

Figure 3.8: CBM machine. Sensitivity studies w.r.t. the radius ratio c_r/c_f.

the camera itself delivers its most accurate measurements in that range. The plot also directly shows where the numerical model is not valid, namely directly inside the melt pool. Here, the temperature drastically overshoots to unrealistically high values. The very good agreement of the computation in the range of the melting zone is further confirmed in figure 3.10. This figure overlays the image of the cross section of the track taken by an ex-situ measurement of a confocal laser scanning microscope (CLSM) with the calibrated computation. Both figures 3.9 and 3.10 demonstrate that it is possible to obtain an excellent agreement with the experiment using the simple physical model presented in section 3.1, if η, f_f/f_r, and c_r/c_f serve as model calibration parameters.

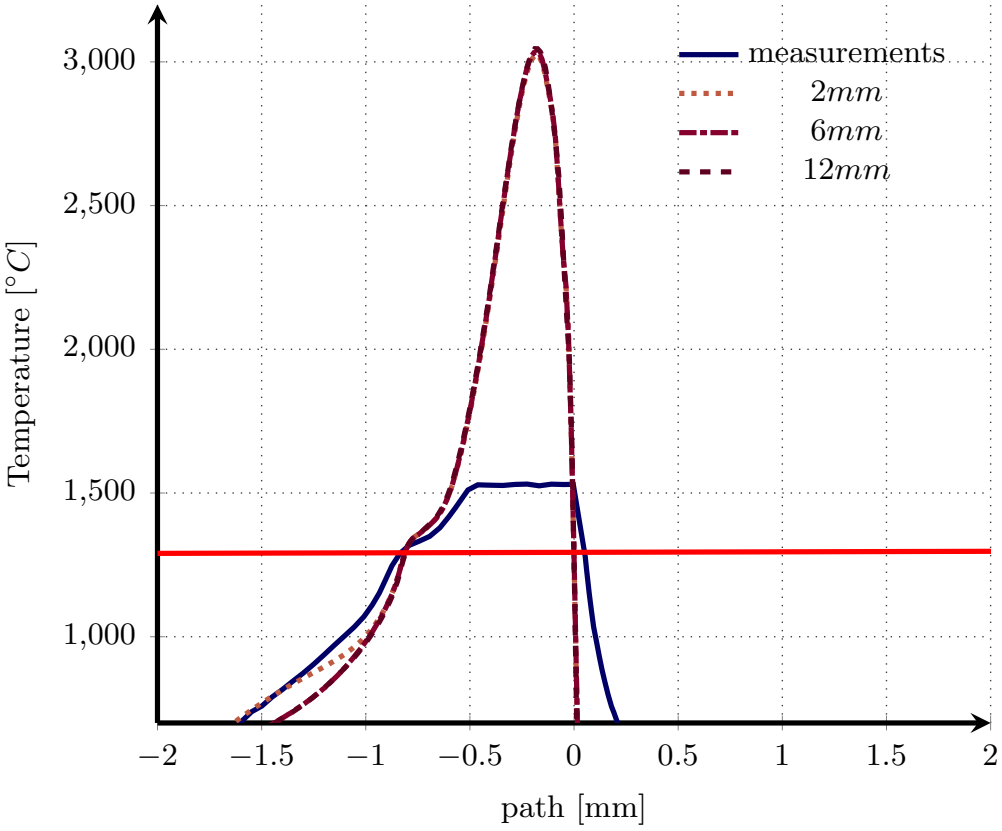

Figure 3.9: Computation of the temperature profile calibrated to case 7 in Ghosh et al. [2018].

Model validation for the CBM machine

The calibrated model delivers the results depicted in table 3.5. It can readily be concluded

case	meas. l[μm]	num. l[μm]	Δ [%]	meas. CR[$\frac{°C}{sec}$]	num. CR [$\frac{°C}{sec}$]	Δ [%]
A	659	707	7.3	6.20×10^5	8.79×10^5	41.8
B	782	812	3.8	9.35×10^5	1.35×10^6	44.3
C	754	772	2.4	1.28×10^6	2.09×10^6	63.3

Table 3.5: CBM machine: obtained weld pool length l and cooling rates CR.

that the model is able to predict the length of the weld pool up to at least 7.3% accuracy in the parameter range covered by cases A to C. The prediction of cooling rates is approximately one order less accurate. In fact, the cooling rate is a derived variable (we directly compute only the temperature) and thus less accuracy is naturally expected; moreover, since our model treats both the liquid and the solid as homogeneous media, the temperature predicted within the melt pool are strongly inaccurate and this surely affects also the cooling rate results in the solid region.

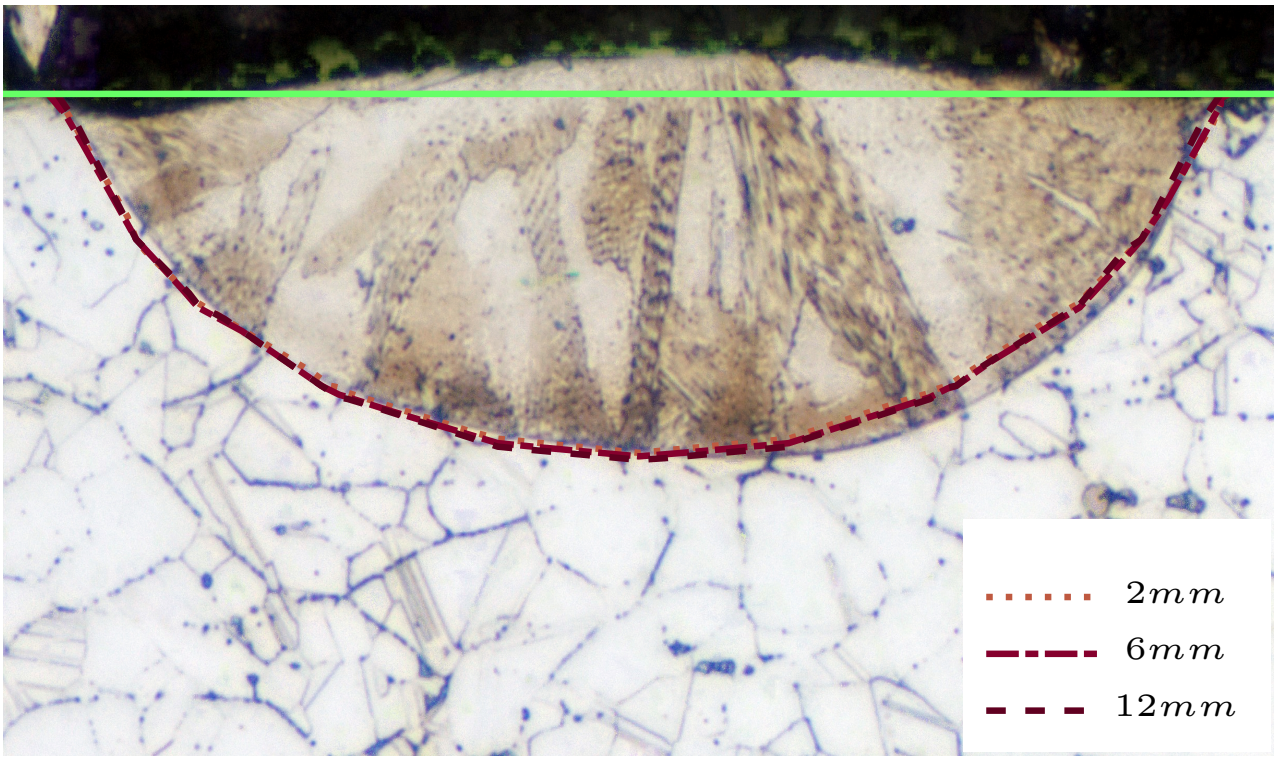

Figure 3.10: Computation of cross section (red line) calibrated to case 7 in Ghosh et al. [2018].

It is interesting to note that the measured length in Ghosh et al. [2018], i.e., the length towards which the model was calibrated was $813[\mu m]$, provided with a tolerance of $\pm 79[\mu m]$. However, measurements performed during for AMBench considering exactly the same case (case B) were more accurate and are given as $782 \pm 21[\mu m]$, see also table 3.5. Thus, a re-calibration of the model to case B will likely deliver more accurate predictions for the cases A and C. However, this was not carried out because even more accurate measurements are available for the AMMT which lead to the development of the extended physical model presented in section 3.3.3.

Model validation for the AMMT machine

Surprisingly, very different experimental results were obtained with the same scan parameters at the AMMT as compared to the CBM. Due to this reason, more thorough studies were carried out on the AMMT. These include measurements of the actual laser profile itself (see figure 3.11). These measurements, now published in www.nist.gov/ambench [2018], enable their direct application as the Neumann boundary condition q^l in equation (3.3). Thus, the physical model presented in section 3.1 is more tightly defined. This generates an interesting situation from the perspective of model validation because two (influential) calibration parameters, the power fraction f_f/f_r and the radius ratio c_r/c_f are now fixed and, therefore, can not be used for calibration. Given that the emissivity ϵ has practically no influence, the absorptivity η is the only parameter left for a re-calibration. For $\eta = 0.086$ we obtain the nu-

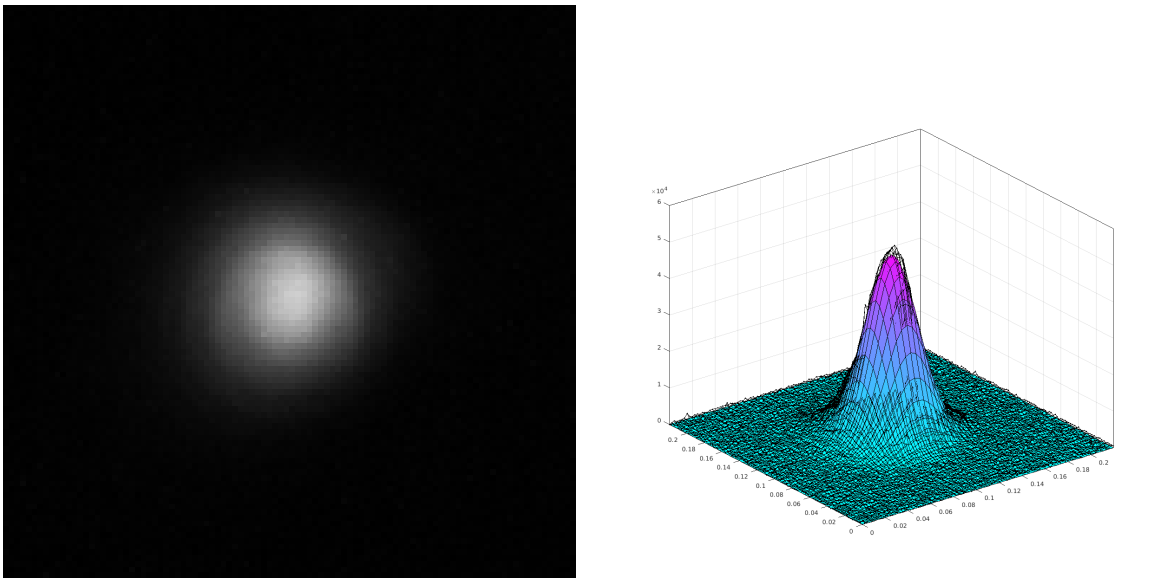

(a) Measured power density (b) Gaussian interpolation of the measured data

Figure 3.11: Power density profile.

merical results provided in table 3.6. The corresponding deviations are provided in table 3.7.

case	length $[\mu m]$	width $[\mu m]$	depth $[\mu m]$	cooling rate $[\frac{^\circ C}{sec}]$
A	301	119	52	0.91×10^6
B	360	103	42	1.33×10^6
C	348	91	32	2.18×10^6

Table 3.6: AMMT machine: computed values.

While the deviations in the length are still at a maximum of approx. 6%, width and depth

case	length $\Delta[\%]$	width $\Delta[\%]$	depth $\Delta[\%]$	cooling rate $\Delta[\%]$
A	0.47	19.3	18.6	21.6
B	0.11	16.4	15.8	23.1
C	5.9	14.2	10.1	14.7

Table 3.7: AMMT machine: deviations from experimental values.

are only predicted to an accuracy of 20%. No further calibration is possible as there is only one parameter to calibrate but three values of interest to fit (excluding the cooling rate). This clearly shows the boundaries of validity of the model presented in section 3.1 and motivates the development of the model discussed in the next section.

3.3.3 Anisotropic conductivity model

Two possible modifications are readily imaginable: a) a definition of an absorptivity field instead of a scalar value η and b) the definition of an anisotropic conductivity. The former could be motivated by the fact that the melt pool surface will surely cause the absorption of the laser energy to be non-constant. However, to the authors opinion a good model should be as simple as possible, yet replicate the observed effects as accurately as possible. With this objective in mind, the definition of an anisotropic conductivity is a more attractive choice. The only change necessary is that the scalar value k in equation (3.1) changes to $\mathbf{k}$, a diagonal matrix with the entries $diag(k_x, k_y, k_z)$. Further, we set $\epsilon = 0$.

The physical motivation for this model is that the (transient) diffusion equation given by equation (3.1) does by no means include the effects caused by convective heat transfer inside the weld pool. This flaw has already inspired other authors e.g., Lu et al. [2018] to use a strongly increased conductivity k inside the melt pool to model convective effects. We now extend this idea by choosing anisotropic values. For simplicity, we introduce the scaling factor ϑ_i where $i = \{x, y, z\}$ such that $\mathbf{k} = diag(k\vartheta_x, k\vartheta_y, k\vartheta_z)$. The values for ϑ_i deviate from 1 only after the last obtainable measurement (at $T = 871°C$) of the conductivity as depicted in figure 3.12. After calibration to the AMMT machine B we obtain the set

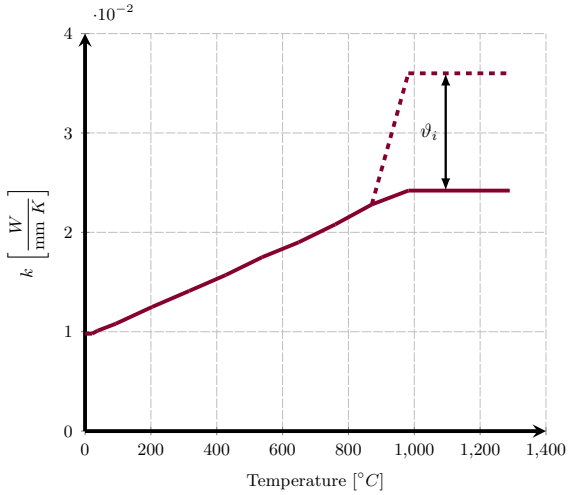

Figure 3.12: Scaling of the conductivity in direction $i = x, y, z$.

$\vartheta_x = 1.0, \vartheta_y = 1.4, \vartheta_z = 0.9$. This delivers very well matching weld pool geometries. While the effect of the scaling of k is marginal in a temperature plot along the length (because here $\vartheta_x = 1.0$), its effect in the cross-section is quite pronounced (see figure 3.13 for a direct overlay of the melt pool geometry over the cross section). In the validation step, we keep the calibration parameters fixed, i.e., $\vartheta_x = 1.0$, $\vartheta_y = 1.4$, and $\vartheta_z = 0.9$ and we compute cases A and C of the AMMT machine. The computed values are provided in table 3.8 and the corresponding deviations are provided in table 3.9. We observe that for the anisotropic model the maximum deviation of length, width and depth is 6.49% at worst while, for the isotropic conductivity model it was merely 19.3%. Even the forecast of the cooling rates has improved sightly.

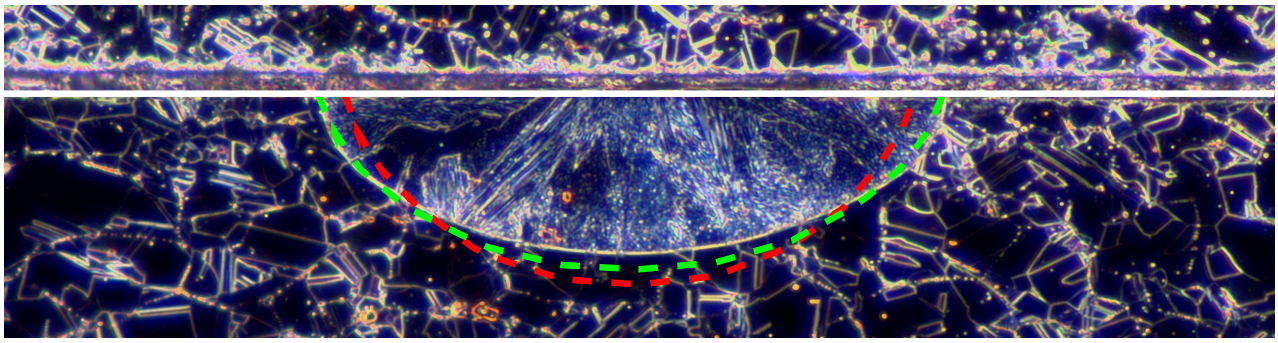

Figure 3.13: Melt pool cross section micrograph image 50×DF (from `https://phasedata.nist.gov/rest/blob?id=5b102edd4407e700870ff13e`) over computed cross sections using isotropic (dashed red line) and anisotropic conductivity (dashed green line).

case	length $[\mu m]$	width $[\mu m]$	depth $[\mu m]$	cooling rate $[\frac{^\circ C}{sec}]$
A	304	146.4	44.6	0.82×10^6
B	362	123.7	36.1	1.23×10^6
C	346	105.1	27.3	1.88×10^6

Table 3.8: Anisotropic conductivity model: computed values.

3.4 Summary and further outlooks

In this chapter we used the standard heat diffusion model to predict the length, width and depth of the melt pool in the laser additive manufacturing benchmarks CHAL-AMB2018-02-MP published in [www.nist.gov/ambench, 2018]. The physical model included a latent heat term as published e.g., in Celentano et al. [1994] along with a radiation boundary condition. Within this model we found the radiation boundary condition to have little to no influence upon the quantities of interest. This is due to the fact that in close proximity of the laser beam impact region, the power lost by radiation is much lower than the applied laser energy itself.

As a first approach we assumed the laser source to possess the well known double elliptical shape as proposed for welding by Goldak et al. [1984]. We demonstrated that this model is well suited to predict the shape of the weld pool as it delivered a maximum deviation from

case	length $\Delta[\%]$	width $\Delta[\%]$	depth $\Delta[\%]$	cooling rate $\Delta[\%]$
A	1.33	1.0	2.5	29.3
B	0.84	0.02	0.2	13.9
C	6.49	0.8	5.1	1.3

Table 3.9: Anisotropic conductivity model: deviations of computed values from experimental values.

the measurements of 7.3%. However, in case the shape of the laser source is given by a measurement, the standard, transient heat diffusion model only provides accuracies of 19.1% for the investigated benchmark cases. This renders it practically invalid.

We then extended the isotropic thermal model by introducing anisotropic conductivities. Their physical interpretation is to model anisotropic convection inside the melt pool. This slight extension enabled the model to deliver at worst 6.49% deviations in length, width and depth of the melt pool. Therefore, we conclude that the introduction of an anisotropic conductivity is a simple, yet effective way to improve the physical model based on transient heat equation including phase changes and remark that the added computational effort for this extension is marginal.

As further outlooks, we aim at validating a numerical model including powder. Nevertheless, this task is not straightforward since measurements of melt pool shapes in presence of a powder bed are extremely challenging. We want to finally stress out the fact that the presented model is meant to provide, once thoroughly calibrated, a reliable model for multi-track and eventually multi-layer thermal simulations, while it is not valid to predict temperature distribution within the melt pool.

Chapter 4

Real-time Feed Forward Control using a-priori Simulation Results

Laser powder bed fusion (LPBF) additive manufacturing (AM) technology can be employed to produce a wide range of products, delivering a high surface finiture and geometric quality of the final artifact. Moreover, metal components obtained using LPBF AM have been observed to be almost fully dense and to reach together mechanical properties equivalent or even higher than traditional manufacturing processes [Craeghs et al., 2010].

Even if the attention on this AM technology has known an exponential growth, LPBF cannot be considered a mature manufacturing process yet. In fact, the lack of reproducibility of a single part together with the inability to guarantee uniform material properties strongly limit the adoption of LPBF systems in wide scale productions. The quality of an LPBF process is influenced by hundreds of controllable and uncontrollable parameters. The former can be estimated by means of either experimental measurements or numerical simulations and optimized consequently in order to achieve the desired accuracy of the final artifact. Nevertheless, due to the high complexity of the physical phenomena involved, many uncontrollable factors can occur during the process.

To this end, research in developing a reliable and effective process control have been considered crucial "to achieve predictable and repeatable operations" [National Institute of Standards and Technology, 2013]. In fact, an efficient control system is required to capture deviations from the predicted (expected) behavior and, if possible, perform *real-time* corrections of process parameters, in order to minimize those errors.

The aim of this chapter is to present a *real-time* process control scheme employing *a-priori* numerical simulations as reference. The outline of the chapter is organized as follows: in the first section, laser systems for LPBF machines are shortly described, in the second section different control strategies are discussed and, finally, in section 4.3 a *real-time* process control scheme based on numerical simulations is presented. All these results have been obtained during a research stay of two month (November-December 2018) at the Engineering Laboratory of the National Institute of Standard and Technology, Gaithersburg (MD, USA) under the supervision of Dr. Brandon Lane.

4.1 Laser system

Before going into the details of control strategy in LPBF processes, we shortly describe the laser system mounted on the additive manufacturing metrology testbed (AMMT) machine described in the previous chapter (see figure 3.4). As in every LPBF machine the laser beam is directed by a couple of mirrors driven by direct current (DC) motors, namely galvo motors (see figure 4.1), to achieve a two-dimensional x-y scan path. The galvos are rotated by electromagnetic force proportional to the current flow in the motor coild and controlled by a closed-loop servo control realized using an internal encoder in the motor shaft. A digital protocol, the so-called xy2-100, provides the two-dimensional position of the laser with a frequecy of 100 kHz. Therefore, the rotation of the galvo mirrors is updated every 10 μs, while the time constant for power adjustment on the AMMT machine is approximately 50 μs. This high temporal resolution of the laser beam system, gives a very precise control of the process in terms of both velocity and power, leading to the possibility to develop a real-time control strategy on such a machine.

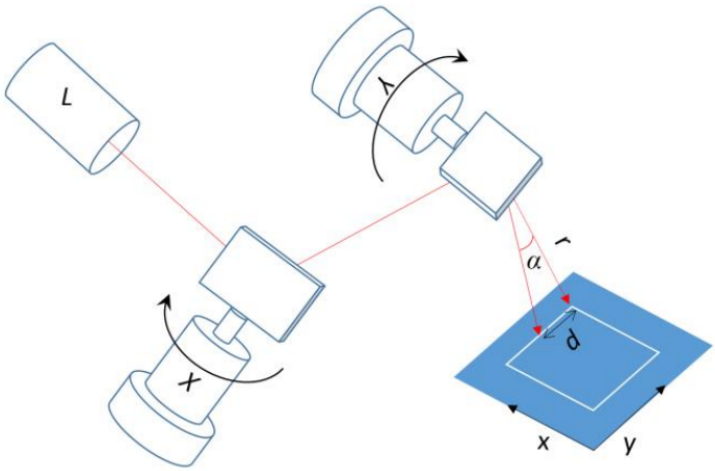

Figure 4.1: Typical scheme of a two-dimensional (x-y) optical scan system [Yeung et al., 2016].

4.2 Control strategies for laser powder bed fusion technology

Mani et al. [2015] define as *process signature* the dynamic characteristics of the power heating, melting, and solidification process as they occur during the building process. They categorize process signatures into two groups:

1. *observable or measurable* (e.g., melt-pool shape and surface temperature);
2. *derived*, i.e., determined by means of numerical models and simulations (e.g., melt-pool depth and residual stress).

Process signatures determine the final product quality; in particular, they have found correlations not only between laser beam controllable parameters (diameter, power, and velocity)

and melt-pool geometry, but also between melt-pool geometry and part quality features such as geometric precision of the final artifact, number of unmelted particles, and voids. Such a study proof that, in principle, it is possible to partially control the geometric precision of the product measuring the melt-pool shape and adjusting controllable laser parameters consequently. This findings motivated the work presented in the following sections.

4.2.1 Laser scan control strategies

In the recent work of Yeung et al. [2018] is presented the implementation of an advanced laser control strategies suitable for LPBF technologies, which allows to obtain complicated scan strategies. In particular, they distinguish the resulting scan strategies based on two categories, namely: *laser path modes* and *laser power modes*. They define three possible laser path modes and three laser power modes, such that the combination of both uniquely define the laser scan strategy.

Laser path modes

1. Exact stop: complete stop of the laser at the end of each track;
2. Constant build speed: the laser velocity is kept constant when the laser is on;
3. Continuous: the end and the start velocity of two consecutive movements are equal.

Laser power modes

1. Constant power: laser power is kept constant during each laser move;
2. Constant density power: the power/speed ratio is constant;
3. Thermal adjust: this mode adjust the power to match reference thermal properties or feedback from real-time monitoring.

In this chapter we will focus on thermal adjust mode in combination with any of the laser path modes. Our methodology employs as reference for the thermal adjust mode the numerical results obtained by means of high-fidelity simulations, using the physical model described in chapter 3.

4.2.2 Co-axial thermal camera signal

Fox et al. [2016] describes a feedback control strategy based on a co-axial melt-pool monitoring, where a reference solution is used to adjust the process parameters based on thermal camera measurements, see figure 4.2. Fox et al. [2016] also demonstrates that - due to the high velocity of the process - laser power is more likely to be manipulated to obtain a real-time control, while the galvanometers response controlling the laser speed is too slow and thus should be predefined. This observation confirm that a thermal adjust laser power mode in combination with any laser path mode can be a suitable choice for a real-time LPBF process control system.

4.2.3 Conversion to true temperature field

If we want to implement a real-time control system for LPBF process we need to take into account the time spent to convert the thermal camera signal to “true” temperature values.

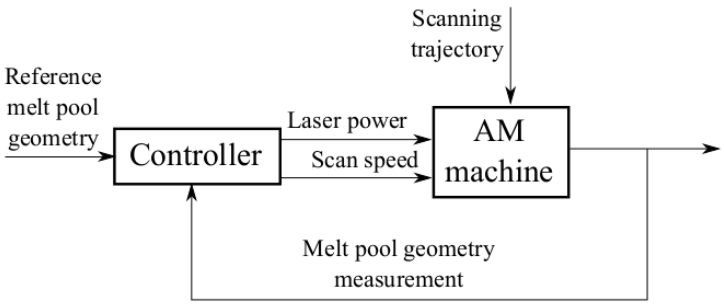

Figure 4.2: Block diagram feedback control from Fox et al. [2016].

This conversion process is described in figure 4.3 where the green arrow indicates the measurement process from the measured thermal camera signal to true temperature. During the measurement process, most of the required operation are extremely complex (e.g., deconvolution) or even impossible to achieve exactly (e.g. conversion from digital to continuous signal). Moreover, most of the input parameters required in this conversion process have to be estimated/calibrated, since they are very challenging to be measured (e.g., emittance). Contrary, the red arrow shows the "inverse" measurement process, i.e. from a ground truth solution (e.g., the solution we can obtain from numerical simulations and assume as reference) to measurement data. This inverse operation, even if not trivial, requires simpler operation than the direct measurement process.

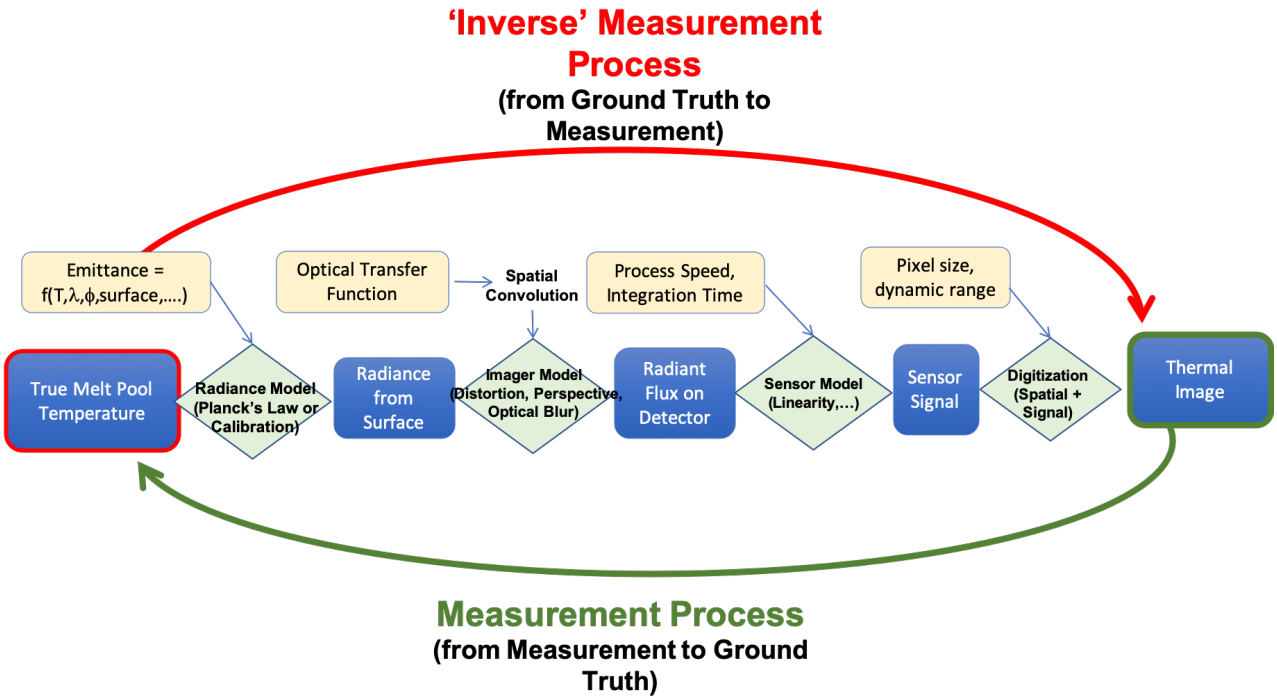

Figure 4.3: Block diagram describing measurement process. The blue squared blocks indicates the physical quantities, the green diamond blocks the conversion functions and the yellow squared blocks the input data required for each function.

4.3 Real-time process control

Starting from the above observations, we decide to employ a thermal digital signal obtained from numerical simulations as reference of our real time control loop. As described in figure 4.4, if we are able to extract from the numerical solution a digitalized image with the same co-axial field of view of the thermal camera, the controller can directly evaluate the deviation of the measured signal performing a simple pixel-by-pixel comparison operation.

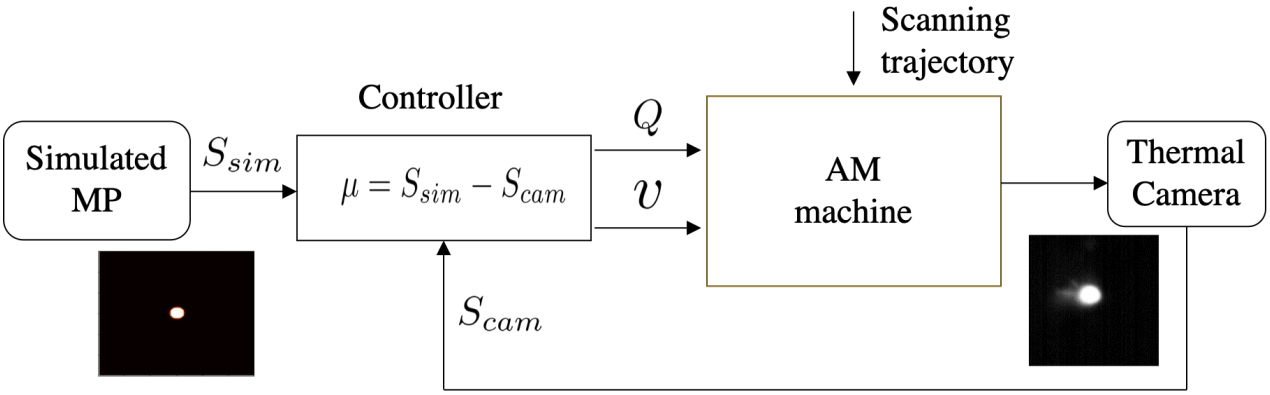

Figure 4.4: Block diagram feedback control employing as reference a digitalized numerical solution in the same co-axial field of view of the thermal camera, where Q is the laser power and v indicates the laser speed.

4.3.1 From simulated "true" temperatures to camera signal

To this end, we need to convert the simulated temperature field on a three dimensional domain into an equivalent digital signal in the co-axial field of view (FOV) of the thermal camera. First, we post-process the temperature on a moving surface always centered at the laser position, having the same size of the camera image. In our case, since we use the images obtained by the thermal camera mounted on the AMMT machine, we define a quadrilateral surface equivalent to the FOV of the thermal camera having a spatial resolution of $3.5\mu m$/pixel and 120×120 pixel.

Figure 4.5 describe the conversion process from the simulated temperature to an equivalent digital signal. In fact, for each time step of our thermal analysis we obtain the “true” temperature field F(T) on the upper surface of our domain in a neighborhood of the laser source (see figure 4.5 **A**). The first operation is to scale the evaluated temperature field by the temperature dependent emissivity value of the material ϵ(T) (figure 4.5 **a**), obtaining the corresponding radiant flux (figure 4.5 **B**). Applying the optical blur and the motion blur filters (steps **b** and **c** of figure 4.5) we obtain the continuous equivalent signal of figure 4.5 **D**. The last step constists in a 12bit digitalization which converts the continuous signal into digital level (figure 4.5 **E**). Since all these operations can be performed before the actual AM process starts, we can provide to the controller a reference of the melt pool shape which can be directly compared in real-time to the measured signal.

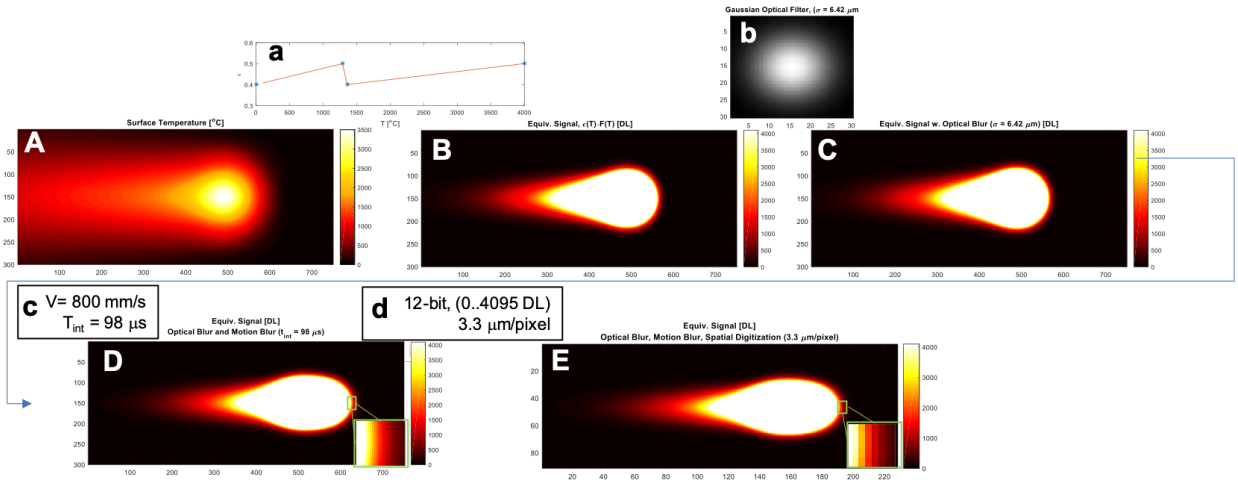

Figure 4.5: Conversion steps from simulated ground truth temperature in degree Celsius to camera signal in digital level.

4.3.2 Towards real-time control

In order to test the proposed method, a thermal camera measurement obtain for AMBench (cfr. chapter 3) is used as experimental reference. We recompute the thermal analysis described in the previous chapter following the procedure to convert simulated temperature to camera signal. Figure 4.6 represents a comparison between the simulated signal and the camera signal. The plot in the figure shows that above the melting temperature (in digital levels) the simulated and the measured signals diverge. This result was expected since the thermal model described in chapter 3 does not include melt pool dynamics, treating the liquid phase within the melt pool as a solid material with different properties. Contrary, below the melting temperature the thermal camera signal is well approximated by the simulated values. This preliminary results encourage us to perform further investigations in this direction, in order to move towards a reliable and effective real-time control system based on numerical thermal analysis of the process.

4.4 Summary and further outlooks

The presented results show that a real-time control scheme based on *a-priori* simulated results is possible thanks to to the possibility to convert continuous, numerical temperature field into digital signals in the thermal camera FOV. Clearly, there are still many issues which have to be solved before such a control strategy can become reality.

In particular, from a computational point of view, if we want to achieve real-time control of the entire manufacturing process, we need to be able to solve at the macro-scale the thermal problem described in chapter 3, i.e., we need to resolve the melt-pool length scale over the entire AM process. In the next chapter, we will see that at the moment it is not possible to compute an entire AM process problem at the melt-pool length scale, thus simplified strategy have to be considered if we want to perform a part-scale analysis. Nevertheless, the proposed control scheme open the possibility to a closer interaction between AM metrology and simulations. In fact, the presented conversion procedure to obtain digital signal from a *ground-truth*

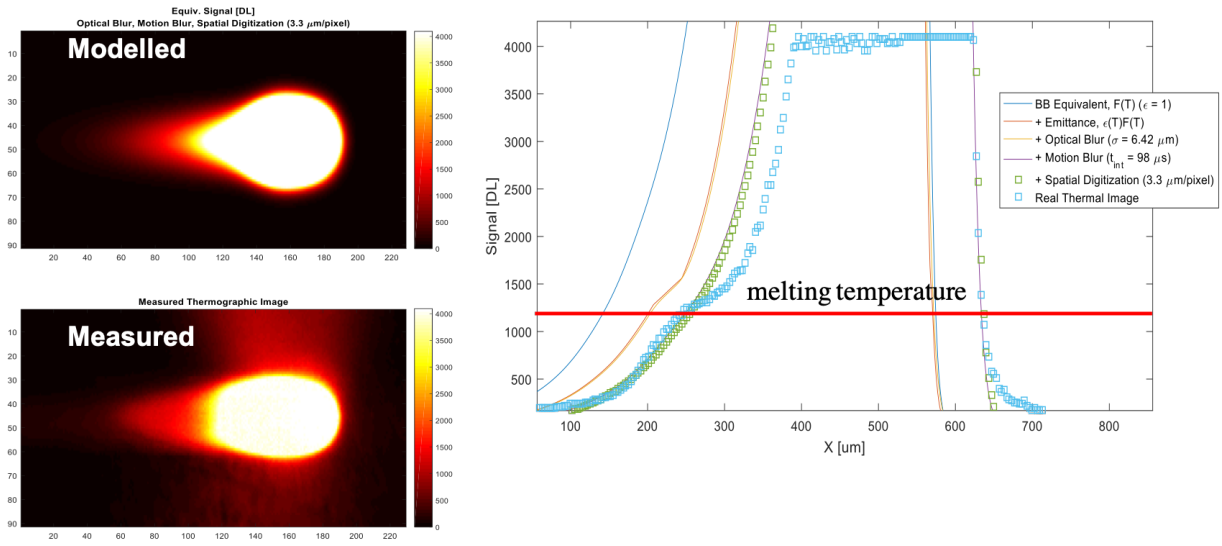

Figure 4.6: Comparison between simulated temperature signal and real thermal image.

temperature (the simulated temperature field) can be extremely useful to better understand the complex steps involved in the measurement process, i.e., when we convert thermal camera signal to true temperature values. Moreover, even localized control strategy, which do not necessarily include the complete process but only few critical spots, might be very important to improve the controllability of LPBF technology.

Chapter 5

Part-scale Additive Manufacturing Thermal Process Simulations using the Finite Cell Method

The aim of this chapter is to present a novel approach to perform part-scale thermal analysis of large components having complex geometry and produced using laser powder bed fusion (LPBF) additive manufacturing (AM) technology. Nowadays, as discussed in the previous chapter, the diffusion of LPBF system is limited by the lack of reproducibility of the process. In particular, we want to focus now on the possibility to capture macro-scale thermal effects (e.g., temperature overshoots due to geometrical features) which is the first step of to obtain residual stress predictions of complex parts. Hereby, we address numerical simulation of complete AM processes of metal components by LPBF technologies, such as Selective Laser Melting (SLM), Direct Metal Laser Sintering (DMLS) or Electron Beam Melting (EBM). All these technologies, can be modeled using the same numerical scheme, since they share the same layer-by-layer approach.

Typical LPBF processes occur within a closed chamber with a controlled atmosphere obtained either by an inert gas (e.g., Argon in SLM processes) or by high vacuum (e.g., in EBM processes). The process proceed incrementally following a layer-by-layer approach, i.e., at each step a roller spread a layer of powder which is locally melted by a laser (or electron) beam. Once the laser scan path of the layer is completed, a piston which control the base plate of the chamber is moved downwards such that a new powder layer can be added.

The manufacturing of a complex functional component by means of LPBF technology requires hundreds or even thousand of layers (typical layer thickness is $\approx 50\mu$m), moreover, the complete process can last hours or even days, while the melting-solidification process occurs within few milliseconds. Therefore, if we want to simulate a complete LPBF process, we cannot employ a physical model such as the one presented in chapter 3 , since it was meant to resolve the problem at the melt-pool length-scale.

To perform part-scale numerical analysis a very popular approach consist in a layer-by-layer activation. This approach usually follows a quite element procedure, where all the elements are created in a pre-processing stage and then selectively activated during the analysis (see, e.g., Michaleris [2014]). Recently, many authors have investigated a layer-by-layer activation approach, where an entire layer (or even a group of multiple layers) is activated simultaneously

(see, e.g., Chiumenti et al. [2017b]; Lindwall et al. [2018]; Lu et al. [2019]). This approach dramatically reduces the computational time and, at the same time, it is still able to capture average effects at the macroscale, while local effects are instead neglected. A layer-by-layer approach is also implemented in almost all the most popular AM commercial codes (e.g., ABAQUS® and ANSYS®) since it is an effective way to rapidly obtain an estimation of the temperature field and residual stresses in the final part.

One of the main drawback of this method is that it needs highly refined meshes to correctly describe complex geometrical features, which are standard for mechanical and structural components produced using AM technologies. The generation of such a mesh can be non-trivial and computationally very expensive, moreover it can easily lead to large system of equations and consequently to a massive memory usage.

The Finite Cell Method (FCM), first introduced in [Düster et al., 2008; Parvizian et al., 2007], allows instead to de-couple complex geometry description from the solution approximation space (the mesh). The geometry is embedded within a simple cartesian grid and resolved only at the integration level. In the following sections, after briefly recalling the key concepts of the method, we present a possible extension of FCM to part-scale thermal analysis of AM processes.

5.1 Thermal analysis

5.1.1 Governing equations

The numerical model described in section 3.1 is now modified in order to reproduce a complete LPBF process. Since the phase change transformation occurs within a very small time interval - which cannot be capture if we are interested in macro-scale effects - we neglect the latent heat term of the heat transfer equation 3.1. Given a spatial domain Ω and a time interval $\mathcal{T} = [0, t_{end})$, the heat transfer model at part-scale can be written as:

$$\rho c \frac{\partial T}{\partial t} - \nabla \cdot (k \nabla T) = Q \qquad \text{in} \quad \Omega \times \mathcal{T}. \tag{5.1}$$

With $\rho = \rho(T)$ temperature dependent density of the material, $c = c(T)$ and $k = k(T)$ temperature dependent heat capacity and thermal conductivity of the material. Equation (5.1) is completed by the initial condition at time $t = 0$:

$$T(\mathbf{x}, 0) = T_0 \qquad \text{in} \quad \Omega, \tag{5.2}$$

Heat source model

The heat source term Q in equation (5.1) is evaluated considering an equivalent heat source contribution:

$$Q = \frac{\eta P}{HAV} \qquad \text{in} \quad \Omega, \tag{5.3}$$

where η is the absorptivity of the material, P is the nominal power of the laser beam, and HAV is the Heat Affected Volume (HAV), i.e. the component volume where the equivalent thermal load is applied within a single activation step. In our case the HAV corresponds to the volume of the layer (or the group of layers) which are heated in a given time step.

5.1.2 Boundary conditions

Build plate boundary condition

On the lateral surfaces of the build plate $\partial\Omega_{bpn}$ we apply convection boundary conditions, such that:

$$q^c_{bp} = h^c_{bp}\,(T_e - T) \qquad \text{on} \quad \partial\Omega_{bpn}, \tag{5.4}$$

while on the bottom of the base plate $\partial\Omega_{bpd}$ we apply Dirichlet boundary conditions, as follows:

$$T = T_{bp} \qquad \text{on} \quad \partial\Omega_{bpd}. \tag{5.5}$$

where T_e and T_{bp} are the external temperature and the prescribed temperature on the bottom of the base plate, respectively.

Powder bed conduction boundary condition

The lateral surface of the part geometry are immersed within the powder bed. Since in our model we do not include the powder surrounding the growing geometry, we model the heat loss through the powder by means of conduction boundary conditions, as follows:

$$q^c_{lat} = h^c_{lat}\,(T_e - T) \qquad \text{on} \quad \partial\Omega_{lat}. \tag{5.6}$$

where h^c_{lat} is the conduction coefficient through the powder.

Upper surface convection and radiation boundary conditions

On the upper surface of the powder bed the heat is dissipated by means of convection and radiation boundary conditions, where the former is defined as:

$$q^{conv}_{top} = h^{conv}_{top}\,(T_e - T) \qquad \text{on} \quad \partial\Omega_{top}, \tag{5.7}$$

while the latter, can be written as:

$$q^r_{top} = \sigma\epsilon\left(T^2 + T_e^2\right)\left(T_e^2 - T^2\right) \qquad \text{on} \quad \partial\Omega_{top}, \tag{5.8}$$

where h^{conv}_{top} is the convection coefficient due to the argon flux, σ is the Stefan-Boltzmann constant, and ϵ the emissivity of the material.

Following the approach proposed in Chiumenti et al. [2017b], radiation and convection boundary conditions can be written using a single parameter, such that:

$$q_{loss} = h_{loss}\,(T_e - T) \qquad \text{on} \quad \partial\Omega_{top}. \tag{5.9}$$

This way to model radiation and convection boundary conditions by means of a single expression is justify by the difficulty to measure these effects. Since the h_{loss} coefficient has not a direct physical meaning, it needs to be experimentally calibrated.

5.1.3 Time integration

In our implementation the time step size is evaluated differently for the heating and the cooling phase. The heating time step size Δt_h depends on the heated surface which is activated within that specific time step, therefore it requires to be evaluated at run time as follows:

$$\Delta t_h = \sum_{i=1}^{m} \frac{HAS_i}{h_d v}, \tag{5.10}$$

where HAS_i is the heat affected surface of the i^{th}-layer, h_d the hatch distance of the laser scan strategy, v the constant laser velocity, and m the number of layers activated in one single heating time step. The cooling time step size Δt_c is instead read from an external input file and defined by the user, it should take into account the time spent by the machine to spread a new layer of powder and the time spent to print the remaining components present on the building plate.

5.2 Numerical model for complex geometry part-scale simulation

5.2.1 Finite Cell Method

The main objective of the finite cell method is to avoid boundary conforming meshing of geometrically complex physical domains. To this end, a geometrically complex domain Ω_{phy} is extended by a fictitious domain Ω_{fict} such that the resulting domain Ω has a simple shape and can thus be meshed easily (see figure 5.1 and Düster et al. [2008]; Parvizian et al. [2007]).

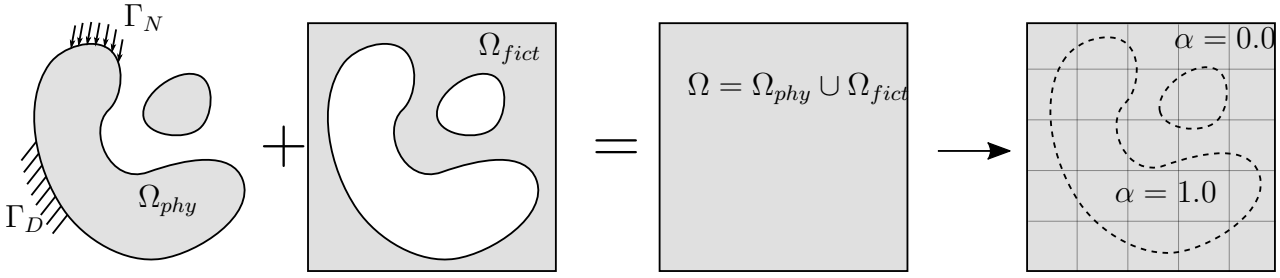

Figure 5.1: Concept of Finite Cell Method

In the simplest case, the mesh is a grid whose entities are called cells, henceforth the name finite cell method. It is on these cells where the shape functions are spanned. The original geometry of the domain is recovered at integration level by use of the following indicator function

$$\alpha = \begin{cases} 1 & \forall \mathbf{x} \in \Omega_{phy} \\ 10^{-g} & \forall \mathbf{x} \in \Omega_{fict} \end{cases} \tag{5.11}$$

where, ideally $g \to \infty$, although in practical applications it is usually sufficient to choose $g = 4$.

The discontinuity introduced by the α coefficent necessitates adaptive integration schemes, see e.g. Abedian et al. [2013]; Kudela et al. [2016] for a recent overview of possible schemes. To compute the following results we employ a simple yet effective integration scheme, where the geometry is voxelized in a pre-processing step and the voxel size is defined by the user. During the analysis, we distribute the Gauss points for the integration directly on the voxels, allowing in this way to capture even small geometrical features in an efficient way.

5.2.2 Multiple layer-by-layer element activation scheme

In this work we employ a m-layers-by-m-layers activation scheme. The proposed method, based on an FCM approach, consists of the following steps:

1. Define a given number of cells in x, y, and z direction such that each cell includes m powder layers in the building direction.
2. Create the integration voxels using $h \times k \times l$ voxels per cell (in this work we set $h = k = l$).
3. Generate the base plate cells.
4. Generate a new layer of cells (i.e., create m new layers of powder) in one single heating time step.
5. Perform an user defined number of cooling time steps, accounting for the time spent in melting other possible components present within the chamber and the time spent for spread m new layers of powder.
6. Repeat step 4 and 5 until the process is completed.

The main difference between the proposed scheme and other m-layers-by-m-layers activation approaches present in literature is the possibility to separate the resolution of the geometry description from the solution approximation. This de-coupling leads to a remarkable improvement in terms of memory consumption and computational time, opening the possibility to simulate the complete LPBF process of components having complex geometry on a standard desktop computer. Moreover, in this work the cells are newly generated at each layer activation, i.e. we do not employ a quite element procedure. This choice is justified by the fact that generating a cell layer in a cartesian grid structure is an extremely simple operation, in such a way we can concentrate the memory and the computational power only where is actually needed, without allocating any space for inactive elements. Another important feature of the presented methodology is that we can weakly apply the boundary condition directly on the original .stl geometry (see Kollmannsberger et al. [2015] for further details on the application of weak boundary condition in FCM).

5.3 Applications

In this section we apply the numerical model presented in this chapter to simulate an industrial component with a complex geometrical shape, namely the optimized GE bracket of figure 5.2, which is a classical benchmark model for AM applications, since many CAD models of this real industrial component are available open source. The following numerical simulation are obtained assuming as material stainless steel 316L, which thermal parameters are reported in appendix C.

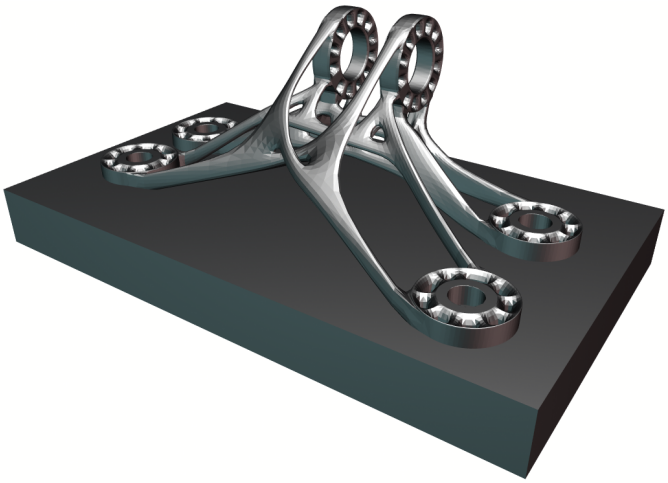

Figure 5.2: GE-bracket: CAD model of an optimized GE Bracket.

FCM at work

Once we obtain the geometrical model, we can directly apply the FCM procedure to perform thermal analysis of the process as described in figure 5.3.

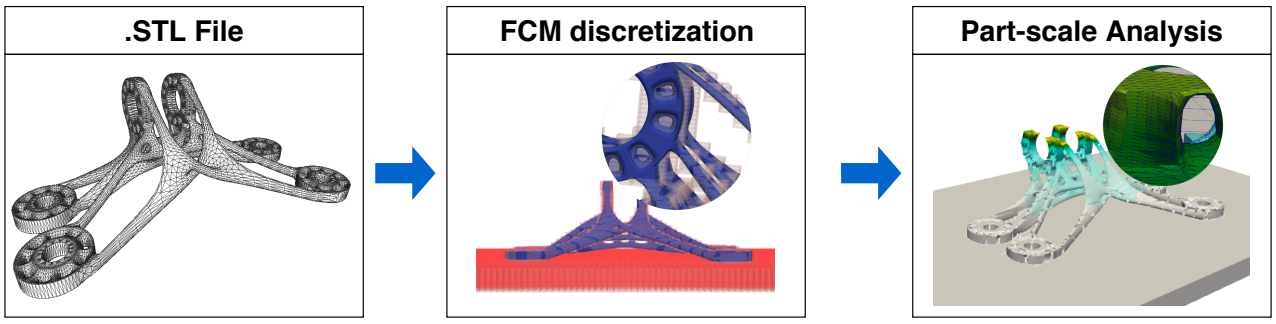

Figure 5.3: GE-bracket: FCM analysis procedure, the original .stl file is in a first step embedded within a cartesian grid (inactive cells are hidden in the figure) to construct the voxel integration grid, we can then perform a layer-by-layer thermal analysis where the BCs are applied directly on the .stl surfaces.

As described in section 5.2.2, we have two key elements which allows us to implicitly represent the complex geometrical shape: the cell, where the functions approximating the solution space are defined, and the voxels which are used to perform a refined Gauss integration; finally, the geometry is implicitly reconstructed by means of a simple inside-outside test performed directly on the .stl file. Figure 5.4a shows the complete problem domain - including the base plate of the building chamber - immersed within the cell grid (in figure 5.4 the cells completely outside the geometry are removed for sake of clarity). Thanks to the FCM concept, the cell grid and the voxel resolution used to integrate over boundaries are completely decoupled, allowing for a very accurate description of geometrical features (see figure 5.4b) employing instead a rather coarse discretization for the approximation of the solution space.

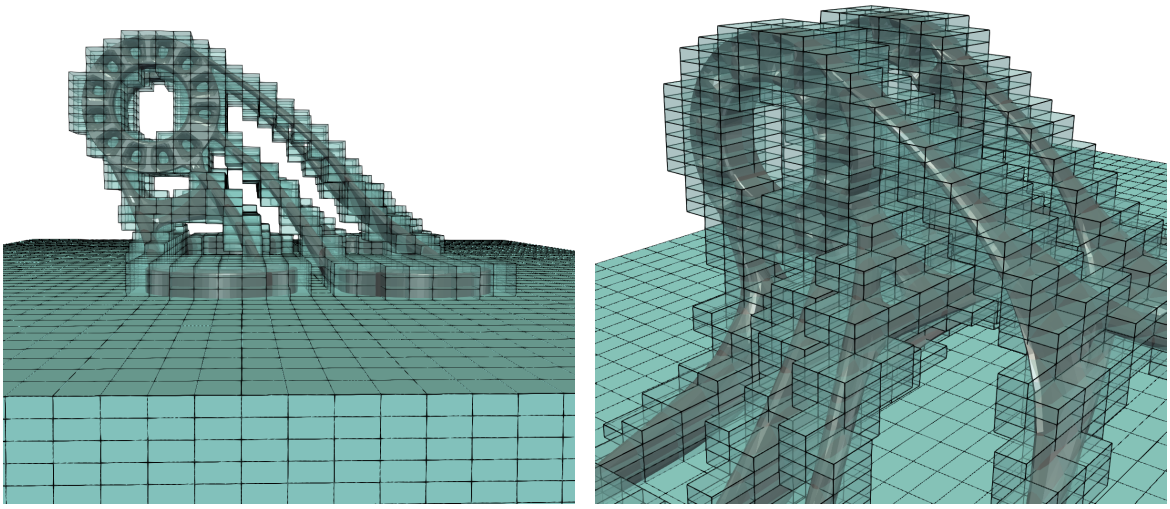

(a) FCM mesh side view. (b) FCM mesh detail.

Figure 5.4: GE-bracket: FCM grid embedding the CAD model.

Multi-layer thermal analysis results

To run our analysis we generate a cartesian grid of $60 \times 100 \times 72$ cells, each cell is subdivided by means of $4 \times 4 \times 4$ integration voxels. We split the process in 60 steps and in each step we perform a heating and a cooling time step, for a total of 120 time steps. At each time step a new layer of cells is generated, i.e., assuming a layer thickness of $50\mu m$ we activate $m = 5$ powder layers within a single step.

Figures 5.5 and 5.6 show the temperature distribution at different heating steps of the process. At time steps 10 and 20, we can observe an overheat in correspondence of dowfacing surfaces. This well known behavior is due to the lack of supports in the original .stl file, which leads to higher peak temperatures in downfacing areas, and is qualitatively captured by our numerical results. Finally, in figure 5.7 we can observe that geometrical information present in the .stl file are maintained during the analysis. In particular, we are able to impose the boundary conditions directly on the .stl surfaces, this feature allows us to correctly estimate the influence of complex geometries on the part-scale thermal analysis results.

5.4 Summary and further outlooks

In this chapter, we have introduced a numerical framework based on the finite cell method to simulate LPBF process at part-scale. Immersed methods, separating the geometry description from the mesh, turn out to be particularly effective in an AM context where we have to deal almost exclusively with complex geometrical shape components potentially very challenging to mesh. Combining an immersed approach together with a m-layer-by-m-layer activation procedure, we are able to perform a complete thermal analysis of LPBF processes employing a rather coarse discretization without any loss of geometrical information.

In this chapter, we have limited the numerical results to a qualitative study of the thermal problem. There are two main reasons for this limitation: first measuring an averaged temper-

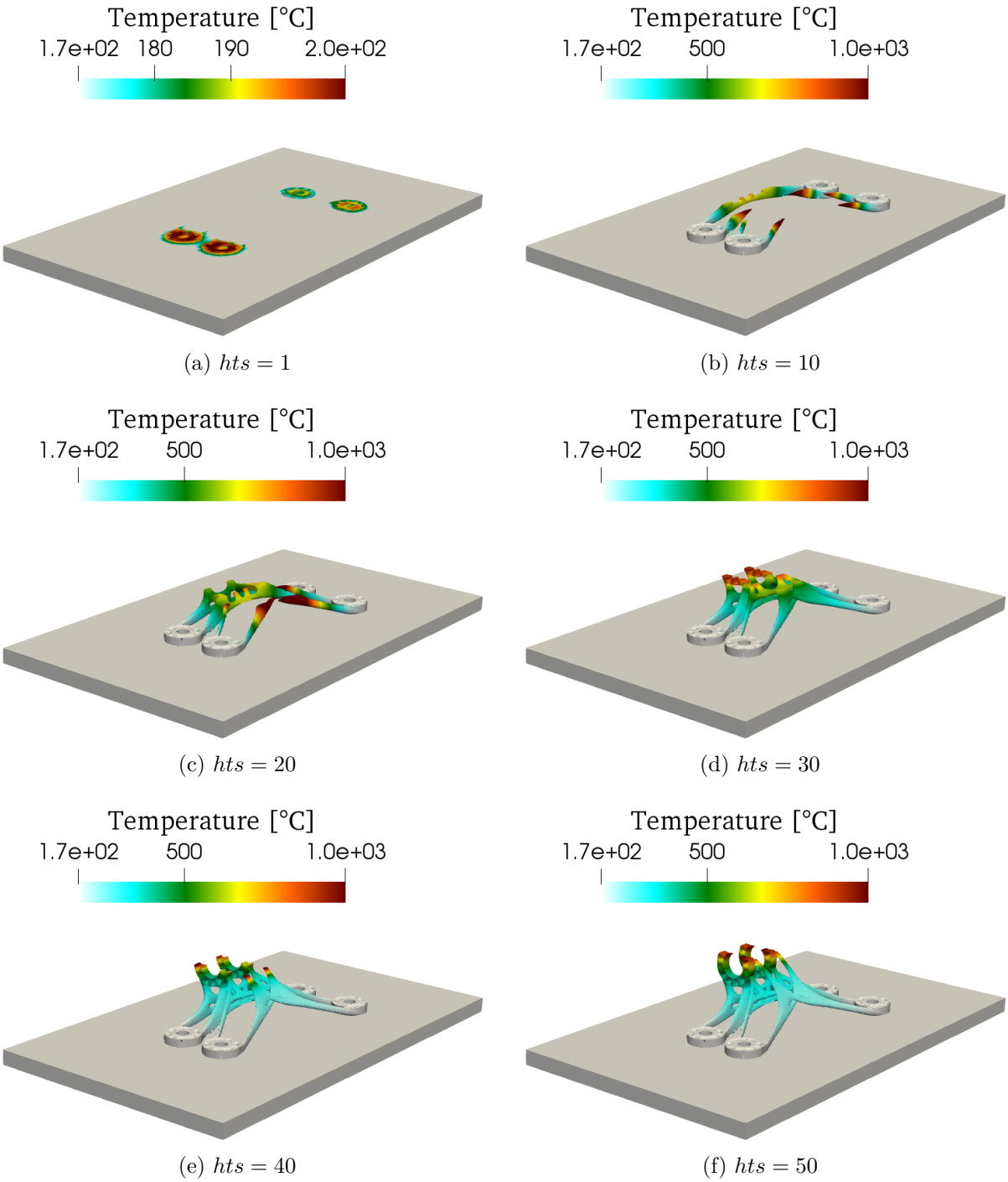

(a) $hts = 1$ (b) $hts = 10$

(c) $hts = 20$ (d) $hts = 30$

(e) $hts = 40$ (f) $hts = 50$

Figure 5.5: GE-bracket: Temperature distribution at different heating time steps hts.

ature by means of thermal cameras or thermocouples is not possible, i.e., we cannot obtain an experimental validation of the thermal analysis results; secondly, the numerical verification of the part-scale thermal analysis would require to solve the problem employing a high-fidelity model, such as the one described in chapter 3, which turns out to be computationally too expensive.

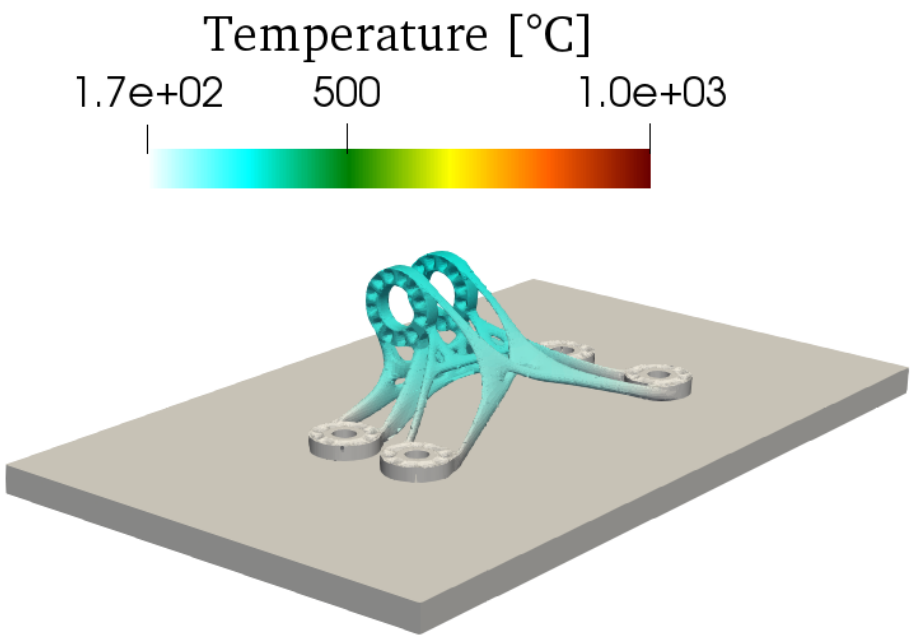

Figure 5.6: GE-bracket: Temperature distribution at the last time step ($ts = 120$).

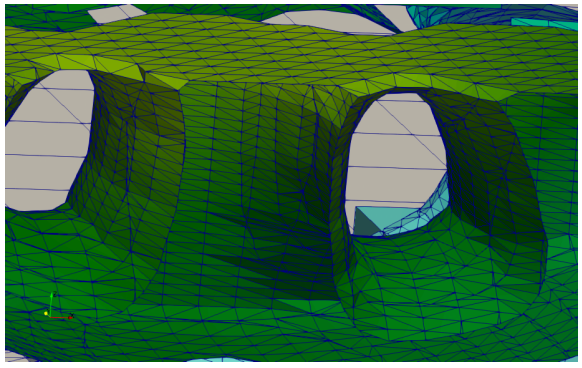

Figure 5.7: GE-bracket: Temperature distribution around a geometrical detail of the bracket.

As further outlooks for the presented work, we first aim at computing thermo-mechanical analysis of LPBF processes extending the presented procedure to include a mechanical problem with plasticity. Secondly, we aim at validating the simulated results by means of experiments: either comparing the numerical results w.r.t. distortion measurements of the manufactured component or comparing the predicted residual stresses with stress measurements obtained by means of neutron diffraction techniques.

Chapter 6

Functionally Graded Material Design for Additive Manufacturing

As defined in Oxman N. and Tsai [2011]: "Functionally Graded Materials (FGMs) are a class of advanced materials characterized by spatial variation in composition across the volume, contributing to corresponding changes in material properties in line with the functional requirements." This class of materials introduces a radical shift from contour modeling to performance modeling by having the performance-driven functionality built directly into the material [Loh et al., 2018]. Since the very beginning AM technologies drastically changed the approach to design. In fact, classical design for manufacturing (DFM) is not required anymore and the designer can now focus on the function of the component itself. FGM design can be seen as a result of this change in the design perspective, where the component is optimized with respect to its specific application starting from its material microstructure. Nevertheless, even if recent AM technologies allow this possibility, the development of numerical methods suitable to generate FGM components is still an open issue for researchers. Moreover, implementations of automatized workflows from numerical results to final products are still an active field of research.

In this chapter we discuss a numerical method to obtain topologically optimized FGM structures first introduced in Carraturo et al. [2019b], together with a possible pipeline to realize these kind of structures using AM technologies. In particular, we present a topology optimization routine based on phase field approach for FGM design together with a tentative workflow to produce the resulting optimized components by means of different AM technologies, extending a previously published work by Alaimo et al. [2019].

There are other methods in literature which allow to obtain similar structures, for example, we mention the landmark contribution of Cheng et al. [2019], where the method of moving asymptotes (MMA) is used to minimize the mass of the structure under stress constraints using an homogenized material definition. Contrary to this method, which can only distribute the material within a given domain, the phase-field approach proposed hereby allows to obtain structures where also regions of voids can be accounted for, substantially introducing an additional degree of freedom within the design process.

6.1 Topology Optimization: From origins to functionally graded material design

The history of topology optimization for continuum structures (see Bendsøe and Kikuchi [1988]; Sigmund and Petersson [1998] for reviews) goes back to the early '80s when the first works on numerical methods suitable to obtain topologically optimized structures appeared. Nowadays, this technology is widespread and it is available in many commercial software. In particular it has known an exponential growth within the engineering community since additive manufacturing technology has become available.

6.1.1 Original approach to structural topology optimization

The original problem of topology optimization aims at obtaining an optimal distribution of a given density function ϕ, defined over a design domain Ω, minimizing a given objective function f (e.g., compliance of the structure). The density function is distributed on Ω taking the value 1 in a domain $D \subset \Omega$ and 0 elsewhere, under a constraint on the maximum volume fraction $m = D/\Omega$. This approach is also called $0-1$ topology optimization and it can be written as follows:

$$\begin{aligned} &\min_{\phi} f(\phi), \\ &s.t. \int_{\Omega} \phi d\Omega \leq m, \\ &\phi(\mathbf{x}) = 0 \vee 1, \quad \forall \mathbf{x} \in \Omega. \end{aligned}$$

Subdividing the design domain Ω into N finite elements and applying Galerkin method to discretize the solution space, we can write the discrete version of the topology optimization problem as:

$$\begin{aligned} &\min_{\phi} f(\phi), \\ &\text{s.t.} \sum_{i=1}^{N} \phi_i v_i \leq m, \\ &\phi_i = 0 \vee 1, \quad i = 1, ..., N, \end{aligned}$$

where ϕ_i and v_i are the element density and volume respectively. It is well know, that the $0-1$ topology optimization suffers of numerical issues (see Sigmund and Petersson [1998] for a detailed review of the argument). They can be subdivided into three classes of problems:

1. Checkboards,
2. Mesh-dependency,
3. Local minima.

Checkboards

The resulting structures are characterized by alternating solid and void elements (see figure 6.1). The reason of this effect is that checkboard structures have artificially high stiffness,

as demonstarted in Diaz and Sigmund [1995]. Possible solutions to this problem are smoothing techniques, high-order finite elements, patches, and filters.

Figure 6.1: Example of checkboard pattern for simply supported beam problem from Sigmund and Petersson [1998].

Mesh-dependency

Ideally mesh refinement should lead to a better description of the boundaries of the structure without resulting in a qualitatively different topology; nevertheless, as shown in figure 6.2, this is not always the case. Sources of this problem can be either *non existence* of the solution or presence of multiple optimal solution, i.e., non uniqueness of the solution. This numerical issue can be solved using two different approaches, namely restriction methods and homogenization. The former includes four different techniques: perimeter control, global and local gradient constraint, and mesh-independent filtering. The latter is quite effective and robust but it leads to microstructure which are impossible to obtain using classical manufacturing techniques. This limit of the homogenization approach can be overcome by the most recent AM technologies (e.g., selective laser sintering and selective laser melting), which allow for a resolution able to produce almost any kind of structure at very small scales.

Figure 6.2: Example of mesh dependency for simply supported beam problem from Sigmund and Petersson [1998].

Local minima

This last numerical issue occurs when a non restricted $0-1$ topology optimization problem is considered. The reason can be found in flatness of the objective function, or, and probably more relevantly, in the numerical optimization scheme employed to solve the problem. Different solutions for local minima have been proposed. Beside many attempts present in literature we recall here only two example of possible solutions:

- *continuation methods*: first a greyscale structure is obtained by means of problem *relaxation* (i.e., the problem has a unique solution) and, after convergence, a penalization routine, which is instead a non-convex problem, is applied to obtain black and white results (see Allaire and Kohn [1993] and Allaire and Francfort [1993]) ;

- *mesh-independence filter approach*: it is a procedure based on a gradual decrement of a filter size which leads to a final 0-1 design (seen Sigmund [1997]).

In conclusion unless smoothness or topologycal constraints are taken into account the two-phase topology optimization problem do not have a unique solution. Unique solution can be instead achieved when homogenization methods are used to relax the original formulation and the problem is now represented as a composite/perforated material optimization problem. For example the popular Solid Isotropic Material with Penalization (SIMP) method, can be interpreted as an homogenization methods where the penalization of the intermediate greyscale region is implicit in the optimization scheme (see Bendsøe [2003]).

6.1.2 Phase field method in topology optimization

In order to overcome the aforementioned limitations of classical numerical methods in topology optimization different approaches have been investigated. The two most relevant are the level set method and the phase field method. The former is characterized by a level set function which describes the target configuration with its zero contour. Its main limitation consists in the function re-initialization which is necessary to achieve an appropriate numerical accuracy. Such a re-initialization is not an easy task and can be computationally expensive.

The phase field method was originally developed to represent the evolution of multi phase problems such as solid-liquid transition problems. Its origin can be traced back to the seminal works of Allen and Cahn [1979] and Cahn and Hilliard [1958]. Successively, the phase field method has been applied to simulate a wide range of problems from dendritic growth (see, e.g., Warren and Boettinger [1995]) to tumor growth (see, e.g., Lorenzo et al. [2017]). Interested readers are refered to Boettinger et al. [2002] for an extensive review of the method.

The method consists in defining a phase field function $\phi = \phi(\mathbf{x})$ over a domain Ω, such that:

$$\phi(\mathbf{x}) = \begin{cases} \phi = 1 & \text{if} \quad \mathbf{x} \in D_1, \\ 0 < \phi < 1 & \text{if} \quad \mathbf{x} \in \gamma, \\ \phi = 0 & \text{if} \quad \mathbf{x} \in D_0, \end{cases} \tag{6.1}$$

where $D_1, D_0 \subset \Omega$. In such a way we can easily represent two phases α and β (with $\alpha < \beta$) within the same domain. In the regions where $\phi = 0$, we assume to have pure phase α, while, where $\phi = 1$, we consider pure phase β. The boundary of each phase is represented as a smooth function, i.e., we have a *diffuse interface* representation of the boundaries. We can define the free energy functional of the system $\mathcal{F}(\phi)$ as:

$$\mathcal{F}(\phi) = \int_\Omega \left(\frac{\gamma}{2} \mid \nabla\phi \mid^2 + \frac{1}{\gamma}\psi_0(\phi) \right) d\Omega, \tag{6.2}$$

where the first term represents the interface energy and $\psi_0(\phi) = (\phi - \phi^2)^2$ is the double-well potential function. The objective of a general phase field problem is hence to minimize the total free energy of the system under given constraints.

The phase field method was first introduced in structural topology optimization by Bourdin and Chambolle [2003]. Starting from a classical topology optimization approach, the method iteratively updates an objective function (e.g., compliance) based on sensitivity analysis. Such

a method allows the nucleation of new holes during the optimization routine, leading to optimized structure very similar to the one we can obtain by means of SIMP approach avoiding most of its numerical drawbacks.

State equations

We consider a domain $\Omega \subset \mathbb{R}^d$ where a material is distributed by means of a scalar phase-field variable ϕ, representing a material density fraction, hence $\phi \in [0,1]$ with $\phi \equiv 0$ corresponding to a void (i.e., no material) and $\phi \equiv 1$ to a dense material. Adopting a linear elastic model, the state equations can be written as follows:

$$-\mathrm{div}\,(\boldsymbol{\sigma}) = \mathbf{f} \quad \text{in} \quad \Omega \tag{6.3}$$

$$\mathbf{u} = \mathbf{0} \quad \text{on} \quad \Gamma_D \tag{6.4}$$

$$\boldsymbol{\sigma} \cdot \mathbf{n} = \mathbf{g} \quad \text{on} \quad \Gamma_N \tag{6.5}$$

with

$$\boldsymbol{\sigma} = \mathbb{C} : \boldsymbol{\varepsilon}(\mathbf{u}) \quad \text{in} \quad \Omega \tag{6.6}$$

where $\mathbb{C} = \mathbb{C}(\phi)$ the fourth-order linear material tensor, $\mathbf{u}$ the displacement field vector, $\boldsymbol{\varepsilon}(\mathbf{u})$ the symmetric strain defined as $\boldsymbol{\varepsilon}(\mathbf{u}) = \nabla^S \mathbf{u} = \left(\nabla \mathbf{u} + \nabla \mathbf{u}^T\right)/2$, $\mathbf{g}$ the external load on the boundary $\Gamma_N \subset \partial\Omega$, and $\Gamma_D \subset \partial\Omega$, $\mid \Gamma_D \mid \neq 0$, the portion of the boundary where homogeneous Dirichlet boundary conditions are applied.

Assuming the material tensor $\mathbb{C}$ to depend on ϕ, the solution of the linear elastic problem depends on the distribution of the scalar field ϕ (i.e., $\mathbf{u} = \mathbf{u}(\phi)$). We treat the void as a *very soft* material, adopting the following expression for $\mathbb{C}$:

$$\mathbb{C}(\phi) = \mathbb{C}_b \phi^p + \mathbb{C}_v (1-\phi)^p$$

where $\mathbb{C}_b$ is the positive definite material tensor of the bulk material, $\mathbb{C}_v$ is the positive definite material tensor of an idealized very soft material (representing the voids), and p can be any positive value; for simplicity, we assume $\mathbb{C}_v = \gamma^2 \mathbb{C}_b$, with $\gamma \ll 1$, while, following [Bendsøe and Sigmund, 1999], we set $p = 3$.

The weak form of the linear elastic problem can be written as:

$$\int_\Omega \boldsymbol{\varepsilon}(\mathbf{u}) : \mathbb{C}(\phi)\boldsymbol{\varepsilon}(\mathbf{v}) \mathrm{d}\Omega = \int_{\Gamma_N} \mathbf{g} \cdot \mathbf{v} \mathrm{d}\Gamma. \tag{6.7}$$

with $\mathbf{v} \in \mathcal{H}^1_D(\Omega)$ a virtual displacement field. Referring to [Blank et al., 2014] we can prove that for any given $\mathbf{g} \in L^2(\Gamma_N)$ and $\phi \in L^\infty(\Omega)$, there exists a unique $\mathbf{u} \in H^1_D(\Omega)$ fulfilling equation (6.7), with $H^1_D(\Omega) := \{\mathbf{v} \in H^1(\Omega) \,:\, \mathbf{v} = \mathbf{0} \quad \text{on } \Gamma_D\}$.

Topology optimization as a minimization problem

The goal of our topology optimization process is to properly minimize the compliance of a given structure by optimally distributing a limited amount of material under a stress constraint.

To properly minimize the compliance, we introduce an objective functional $\mathcal{J}(\phi, \mathbf{u})$ defined as:

$$\begin{aligned}&\mathcal{J}(\phi, \mathbf{u}, \boldsymbol{\sigma}) = \\ &\kappa_g \int_{\Gamma_N} \mathbf{g} \cdot \mathbf{u} \mathrm{d}\Gamma + \kappa \int_\Omega \left[\frac{\gamma}{2} \parallel \nabla \phi \parallel^2 + \frac{1}{\gamma} \psi_0(\phi) \right] \mathrm{d}\Omega + \\ &\kappa_f \int_\Omega \phi \, (\mathbf{f} \cdot \mathbf{u}) \mathrm{d}\Omega + \kappa_\sigma \int_\Omega F(\boldsymbol{\sigma}) \mathrm{d}\Omega\end{aligned} \tag{6.8}$$

where the first integral represents a measure of the global system compliance, defined as the inverse of the stiffness, while, assuming $\kappa > 0$, the second integral is an approximation of the perimeter of the interfaces between regions with $\phi = 0$ and $\phi = 1$. In equation (6.8) γ corresponds to the thickness of the diffuse interface, i.e., the region where $0 < \phi < 1$, the term $\gamma/2 \mid \nabla \phi \mid^2$ penalizes jumps between $\phi = 0$ and $\phi = 1$, while $\psi_0(\phi)/\gamma$ represents the double-well potential function penalizing phases with ϕ different from 0 and 1. Let us point out that in the cost functional 6.8, we include the last term in order to possibly account for the stress constraint, which naturally appears in practical applications, e.g., in structural engineering problems where we require that the stress does not exceed some material dependent threshold value. In the ideal case, we would like to impose a maximum stress ratio based on a given stress criterion (e.g., von Mises, Tresca, Hill, ...), such that

$$\sigma_{max} = \max \left(\frac{\sigma_e}{\sigma_y} \right), \tag{6.9}$$

where σ_e is the equivalent stress depending on the chosen criterion and σ_y the material dependent yield stress. Since this function is not differentiable, a very popular solution in the literature of topology optimization with stress constraints (cf., e.g. Le et al. [2010]; Lee et al. [2012]; Zhou and Sigmund [2017]) is to employ the p-norm of the stresses defined as:

$$\sigma_{PN} = \left(\int_\Omega \left(\frac{\sigma_e}{\sigma_y} \right)^p \right)^{1/p},$$

where the parameter p controls the level of smoothness of the function, with $p \to \infty$ leading to the max function of equation (6.9). Finally, the function F can be taken as

$$F(\boldsymbol{\sigma}) = \mid \sigma_{PN} - 1 \mid .$$

We remark that following [Blank et al., 2014] we choose the same scaling parameter γ to penalize the sharp interface region and to define the void soft material; this choice is justified by the assumption that when one of the two values goes to zero also the other one has to vanish.

The minimization of the functional in equation (6.8) is imposed under the assumption of distributing a limited constant quantity of material inside the domain, hence, we introduce the constraint:

$$\int_\Omega \phi \mathrm{d}\Omega = m \mid \Omega \mid$$

with $0 < m \leq 1$ representing a target domain volume fraction. Clearly, the displacement field $\mathbf{u}(\phi)$ solving the topology optimization problem should also be solution of the linear elastic problem of equation (6.7).

In conclusion, the minimization problem we aim to solve is the following.
Problem ($\mathcal{P}$):

$$\min_{\phi} \quad \mathcal{J}(\phi, \mathbf{u}, \boldsymbol{\sigma})$$

such that the following constraints are satisfied:

$$\int_{\Omega} \boldsymbol{\sigma} \colon \boldsymbol{\varepsilon}(\mathbf{v}) \mathrm{d}\Omega = \int_{\Omega} \mathbf{f} \cdot \mathbf{v} \mathrm{d}\Omega + \int_{\Gamma_N} \mathbf{g} \cdot \mathbf{v} \mathrm{d}\Gamma. \tag{6.10}$$

$$\mathcal{M}(\phi) = \int_{\Omega} \phi \mathrm{d}\Omega - m \mid \Omega \mid = 0, \tag{6.11}$$

with $\phi \in H^1(\Omega)$ satisfying the constraint:

$$0 \leq \phi \leq 1 \qquad \text{a.e. in } \Omega. \tag{6.12}$$

Following the argument by [Blank et al., 2014], we can prove that the minimum constrained problem ($\mathcal{P}$) has at least one solution (cf. [Blank et al., 2014, Thm. 4.1]). In particular, to solve problem ($\mathcal{P}$) we introduce the Lagrangian functional $\mathcal{L}$, defined as:

$$\mathcal{L}(\phi, \lambda, \mathbf{u}, \boldsymbol{\sigma}, \mathbf{U}, \boldsymbol{\Sigma}) = \mathcal{J}(\phi, \mathbf{u}, \boldsymbol{\sigma}) + \lambda \mathcal{M}(\phi) + \mathcal{S}(\phi, \mathbf{u}, \boldsymbol{\sigma}, \mathbf{U}, \boldsymbol{\Sigma}), \tag{6.13}$$

where λ is the Lagrange multiplier introduced to impose the volume constrain of equation (6.11) and $\mathcal{S}$ is the adjoint problem operator defined as follows:

$$\begin{aligned} &\mathcal{S}(\phi, \mathbf{u}, \boldsymbol{\sigma}, \mathbf{U}, \boldsymbol{\Sigma}) = \\ &- \int_{\Omega} \boldsymbol{\sigma} \colon \boldsymbol{\varepsilon}(\mathbf{U}) \mathrm{d}\Omega + \int_{\Gamma_N} \mathbf{g} \cdot \mathbf{U} \mathrm{d}\Gamma + \int_{\Omega} \mathbf{f} \cdot \mathbf{U} \mathrm{d}\Omega + \int_{\Omega} \left(\boldsymbol{\sigma} - \mathbb{C}(\phi) \colon \boldsymbol{\varepsilon}(\mathbf{u}) \right) \boldsymbol{\Sigma} \mathrm{d}\Omega, \end{aligned}$$

which we introduce together with the adjoint variables $\mathbf{U}$ and $\boldsymbol{\Sigma}$.

The solution of problem ($\mathcal{P}$) is equivalent to the minimization of equation (6.13) subjected to the constraint of equation (6.12); this last problem can be seen as an optimal control problem, with solutions $(\bar{\phi}, \bar{\lambda}, \bar{\mathbf{u}}, \bar{\boldsymbol{\sigma}}, \bar{\mathbf{U}}, \bar{\boldsymbol{\Sigma}})$ that have to satisfy the first order optimality conditions defined by:

$$D_{\phi} \mathcal{L}(\bar{\phi}, \bar{\lambda}, \bar{\mathbf{u}}, \bar{\boldsymbol{\sigma}}, \bar{\mathbf{U}}, \bar{\boldsymbol{\Sigma}})(\phi - \bar{\phi}) \geq 0 \qquad \forall \phi \in \Phi_{ad},$$

where Φ_{ad} is the set of admissible controls defined as follows:

$$\Phi_{ad} := \{\phi \in H^1_D(\Omega) \, : \, 0 \leq \phi \leq 1 \quad \text{a.e. in } \Omega\}.$$

Thus, to get minimizers we consider the partial derivatives of the lagrangian w.r.t. $\mathbf{u}$ and $\boldsymbol{\sigma}$, $\mathcal{L}_{\mathbf{u}}$ and $\mathcal{L}_{\boldsymbol{\sigma}}$ respectively, and impose that they are equal to zero. From these relations,

it is straightforward, also by definition of $\mathcal{J}$, to derive the so-called adjoint equations. In particular, we get

$$\operatorname{div}(\mathbb{C}^T(\bar{\phi})\boldsymbol{\Sigma}) = \kappa_f \bar{\phi}\mathbf{f} \qquad \text{a.e. in } \Omega \tag{6.14}$$

$$\mathbb{C}^T(\bar{\phi})\boldsymbol{\Sigma}\cdot\mathbf{n} = \kappa_g \mathbf{g} \qquad \text{a.e. on } \Gamma_N \tag{6.15}$$

$$\boldsymbol{\Sigma} = \boldsymbol{\varepsilon}(\mathbf{U}) - \kappa_\sigma F_{\boldsymbol{\sigma}}(\bar{\boldsymbol{\sigma}}) \qquad \text{a.e. in } \Omega. \tag{6.16}$$

To obtain a more compact formulation, we define here the energy density of the system and its derivative w.r.t. the scalar field ϕ as:

$$\mathcal{E}(\phi, \mathbf{u}) = \boldsymbol{\varepsilon}(\mathbf{u}) : \mathbb{C}(\phi)\boldsymbol{\varepsilon}(\mathbf{u}),$$

and

$$\frac{\partial \mathcal{E}(\phi, \mathbf{u})}{\partial \phi} = \boldsymbol{\varepsilon}(\mathbf{u}) : \frac{\partial \mathbb{C}(\phi)}{\partial \phi}\boldsymbol{\varepsilon}(\mathbf{u}).$$

To discretize our continuous problem we employ a gradient flow dynamics, namely Allen-Cahn gradient flow [Allen and Cahn, 1979], a steepest descent pseudo-time stepping method with a time-step increment τ. Thus the optimal control problem $(\mathcal{P})$ can be now rewritten as follows:

$$D_\lambda \mathcal{L}\, v_\lambda = \mathcal{M} v_\lambda = 0, \tag{6.17}$$

$$\frac{\gamma}{\tau}\int_\Omega (\phi_{n+1} - \phi_n) v_\phi \mathrm{d}\Omega = -D_\phi \mathcal{L}\, v_\phi, \tag{6.18}$$

where

$$D_\phi \mathcal{L} = \frac{\partial \mathcal{J}}{\partial \phi} + \lambda \frac{\partial \mathcal{M}}{\partial \phi} + \frac{\partial \mathcal{S}}{\partial \phi},$$

with $v_\lambda \in \mathbb{R}$ and $v_\phi \in \Phi_{ad}$.

The optimal control problem $(\mathcal{P})$ can be finally written in the following weak extended formulation:

$$\int_\Omega v_\lambda(\phi_{n+1} - m)\mathrm{d}\Omega = 0, \tag{6.19}$$

$$\begin{aligned}\frac{\gamma}{\tau}\int_\Omega (\phi_{n+1} - \phi_n) v_\phi \mathrm{d}\Omega + \kappa\gamma \int_\Omega \nabla\phi_{n+1}\cdot\nabla v_\phi \mathrm{d}\Omega \\ + \lambda\int_\Omega v_\phi \mathrm{d}\Omega - \int_\Omega v_\phi \frac{\partial \mathcal{E}(\phi_n, \mathbf{u}_n)}{\partial \phi}\mathrm{d}\Omega + \frac{\kappa}{\gamma}\int_\Omega \frac{\partial \psi_0(\phi_n)}{\partial \phi} v_\phi \mathrm{d}\Omega = 0,\end{aligned} \tag{6.20}$$

which we solve by means of the finite element method.

Finite element formulation

We derive here a finite element approximation of the phase-field topology optimization problem previously defined. To this end, we discretize the physical domain Ω employing three triangular meshes $\mathcal{T}_u$, $\mathcal{T}_\phi$,and $\mathcal{T}_U$, one for each variable of the problem. At the nodes of each

triangular element we interpolate, by means of piecewise linear basis functions, the corresponding variables $\mathbf{u}$, ϕ, and $\mathbf{U}$ together with their variations $\mathbf{v}$, v_ϕ,and $\mathbf{v_U}$, obtaining the following finite element expansions:

$$\begin{aligned} \mathbf{u} &\approx \mathbf{N_u}\tilde{\mathbf{u}}, & \mathbf{v} &\approx \mathbf{N_u}\tilde{\mathbf{v}}, \\ \phi &\approx \mathbf{N}_\phi\tilde{\boldsymbol{\phi}}, & v_\phi &\approx \mathbf{N}_\phi\tilde{\mathbf{v}}_\phi, \\ \mathbf{U} &\approx \mathbf{N_U}\tilde{\mathbf{U}}, & v_U &\approx \mathbf{N_U}\tilde{\mathbf{v}}_\mathbf{U}, \end{aligned}$$

where $\mathbf{N_u}, \mathbf{N}_\phi, \mathbf{N_U}$ are the piecewise linear shape function vectors and matrices which interpolate the nodal degrees of freedoms $\tilde{\mathbf{u}}, \tilde{\boldsymbol{\phi}}, \tilde{\mathbf{U}}$ and their variations $\tilde{\mathbf{v}}, \tilde{\mathbf{v}}_\phi, \tilde{\mathbf{v}}_\mathbf{U}$. Finally, the Lagrange multiplier λ - used to constrain the volume - is applied using a constant scalar value on the domain Ω.

We can now write the discretized version of the optimal control problem $(\mathcal{P})$, as follows:

$$\frac{1}{\tau}\begin{bmatrix} \mathbf{0} & \mathbf{0} & \mathbf{0} & \mathbf{0} \\ \mathbf{0} & \mathbf{0} & \mathbf{0} & \mathbf{0} \\ \mathbf{0} & \mathbf{0} & \mathbf{M}^{\phi\phi} & \mathbf{M}^{\phi\lambda} \\ \mathbf{0} & \mathbf{0} & \mathbf{M}^{\lambda\phi} & 0 \end{bmatrix} \begin{bmatrix} \tilde{\mathbf{u}} \\ \tilde{\mathbf{U}} \\ \tilde{\boldsymbol{\phi}} \\ \tilde{\lambda} \end{bmatrix} + \begin{bmatrix} \mathbf{K^{uu}} & \mathbf{0} & \mathbf{0} & \\ \mathbf{0} & \mathbf{K^{UU}} & \mathbf{0} & \mathbf{0} \\ \mathbf{0} & \mathbf{0} & \mathbf{K}^{\phi\phi} & \mathbf{0} \\ \mathbf{0} & \mathbf{0} & \mathbf{0} & 0 \end{bmatrix} \begin{bmatrix} \tilde{\mathbf{u}} \\ \tilde{\mathbf{U}} \\ \tilde{\boldsymbol{\phi}} \\ \tilde{\lambda} \end{bmatrix} = \begin{bmatrix} \mathbf{f} \\ \mathbf{F} + \mathbf{q}^\sigma \\ \mathbf{q}^\phi + \mathbf{q}^s + \mathbf{q}^\psi \\ q^\lambda \end{bmatrix} \tag{6.21}$$

with the matrix and vector terms defined as:

$$\begin{aligned} \mathbf{K^{uu}} &= \int_\Omega \nabla\mathbf{N_u}^T \mathbb{C} \nabla\mathbf{N_u}\, d\Omega, \\ \mathbf{K^{UU}} &= \int_\Omega \nabla\mathbf{N_U}^T \mathbb{C} \nabla\mathbf{N_U}\, d\Omega, \\ \mathbf{M}^{\phi\phi} &= \gamma_\phi \int_\Omega \mathbf{N}_\phi^T \mathbf{N}_\phi\, d\Omega, \\ \mathbf{K}^{\phi\phi} &= \kappa\gamma_\phi \int_\Omega \nabla\mathbf{N}_\phi^T \nabla\mathbf{N}_\phi\, d\Omega, \\ \mathbf{M}^{\lambda\phi} &= \tau \int_\Omega \mathbf{N}_\lambda^T \mathbf{N}_\phi d\Omega = \left(\mathbf{M}^{\phi\lambda}\right)^T, \\ \mathbf{f} &= \int_{\Gamma_N} \mathbf{N_u}^T \mathbf{g}\, d\Gamma, \\ \mathbf{F} &= \int_{\Gamma_N} \mathbf{N_U}^T \mathbf{g}\, d\Gamma, \\ \mathbf{q}^\sigma &= \kappa_\sigma \int_\Omega \mathbf{N_U}^T F_{\boldsymbol{\sigma}}(\boldsymbol{\sigma}_{n+1})\, d\Omega, \\ \mathbf{q}^\phi &= \frac{\gamma_\phi}{\tau} \int_\Omega \left(\mathbf{N}_\phi^T \mathbf{N}_\phi\right) \tilde{\boldsymbol{\phi}}_n\, d\Omega = \mathbf{M}^{\phi\phi}\tilde{\boldsymbol{\phi}}_n, \\ q^\lambda &= \int_\Omega m\, d\Omega, \\ \mathbf{q}^s &= \int_\Omega \mathbf{N}_\phi^T \frac{\partial\mathcal{E}(\phi, \mathbf{u})}{\partial\phi}\, d\Omega, \\ \mathbf{q}^\psi &= \frac{\kappa}{\gamma_\phi} \int_\Omega \mathbf{N}_\phi^T \frac{\partial\psi_0(\phi)}{\partial\phi}\, d\Omega. \end{aligned}$$

To obtain a topologically optimized structure, we solve the problem in equation (6.21) employing a staggered iterative approach as described in algorithm 6. In fact, the linear system in equation (6.21) can be split into three linear systems which we solve separately: the state equation system

$$\mathbf{K}^{\mathbf{uu}}\tilde{\mathbf{u}} = \mathbf{f}, \tag{6.22}$$

the adjoint problem system

$$\mathbf{K}^{\mathbf{UU}}\tilde{\mathbf{U}} = \mathbf{F} + \mathbf{q}^{\sigma}, \tag{6.23}$$

and the phase-field system

$$\frac{1}{\tau}\begin{bmatrix}\mathbf{M}^{\phi\phi} & \mathbf{M}^{\phi\lambda}\\ \mathbf{M}^{\lambda\phi} & 0\end{bmatrix}\begin{bmatrix}\tilde{\boldsymbol{\phi}}\\ \tilde{\lambda}\end{bmatrix} + \begin{bmatrix}\mathbf{K}^{\phi\phi} & \mathbf{0}\\ \mathbf{0} & 0\end{bmatrix}\begin{bmatrix}\tilde{\boldsymbol{\phi}}\\ \tilde{\lambda}\end{bmatrix} = \begin{bmatrix}\mathbf{q}^{\phi} + \mathbf{q}^{s} + \mathbf{q}^{\psi}\\ q^{\lambda}\end{bmatrix}. \tag{6.24}$$

which can be solved with either a direct or an iterative solver. The `phase-field optimization` routine defined in algorithm 6 presents an iterative procedure where we first solve the state equation system 6.22 to get the solution vector $\tilde{\mathbf{u}}_{n+1}$, secondly we solve the adjoint system 6.23, and finally we evaluate the phase-field system 6.24 to obtain the phase-field solution vector $\tilde{\boldsymbol{\phi}^*}_{n+1}$ together with the Lagrange multiplier $\tilde{\lambda}_{n+1}$. Every iteration ends calling the function `rescale`, as defined in algorithm 7 to impose the constraints on the phase-field variable ϕ directly at the nodal values. The `phase-field optimization` routine is then repeated until either the maximum number of iteration (max_{iter}) is reached or the L^2-norm of the phase-field variable increment $\Delta_\phi = \| \boldsymbol{\phi}_{n+1} - \boldsymbol{\phi}_n \|_{L^2}$ is below a given tolerance (tol).

Algorithm 6 `phase-field optimization`

Input: $\mathcal{T}_U$, $\mathcal{T}_\phi$, $\mathcal{T}_u$, $\boldsymbol{\phi}_0$
Output: Optimal topology

$\boldsymbol{\phi}_n \leftarrow \boldsymbol{\phi}_0$
while ($\Delta_\phi \geq tol$) and $n \leq max_{iter}$ **do**
  $\tilde{\mathbf{u}}_{n+1} \leftarrow$ `solve` 6.22
  $\tilde{\mathbf{U}}_{n+1} \leftarrow$ `solve` 6.23
  $(\tilde{\boldsymbol{\phi}}^*_{n+1}, \tilde{\lambda}_{n+1}) \leftarrow$ `solve` 6.24
  $\tilde{\boldsymbol{\phi}}_{n+1} \leftarrow$ `rescale` $\left(\tilde{\boldsymbol{\phi}}^*_{n+1}, [0,1]\right)$
  `update`(Δ_ϕ)
  $\boldsymbol{\phi}_n \leftarrow \boldsymbol{\phi}_{n+1}$
end while

6.1.3 Functionally graded material design optimization

In this section we want to develop a new phase field formulation to obtain graded material structures. Such a kind of structure is tightly connected with AM technologies since the high flexibility introduced into manufacturing processes allows to vary the material properties in an almost continuous fashion. This AM feature leads to a change in the design and manufacturing paradigms, shifting the focus of design from a manufacturing oriented design, also

Algorithm 7 `rescale`

Input: $\boldsymbol{\omega}$, $[a, b]$
Output: Constrained solution vector

```
for all ω_i ∈ ω do
    if ω_i < a then
        ω_i = a
    else if ω_i > b then
        ω_i = b
    else
        do nothing
    end if
end for
```

known as *design for manufacturing*, to the so called *functional design*, where the objective of design is now the functionality of the component and not anymore its manufacturability. In particular, in this section we focus on a particular type of functional design, the so called *functionally graded material design* (FGMD). This kind of design aims at obtaining structures with mechanical properties which are similar to fully dense material structure, but employing less material. In this sense, we exploit the possibility to obtain local voids and/or lattice microstructures given by the most recent AM processes. Such a result can be achieved by means of a topology optimization routine which is able to optimally distribute a varying material density parameter within the structure. In this work, we first develop and implement a phase field topology optimization procedure suitable for FGMD, then we build a complete computational framework to convert numerical results to 3D printable models.

Asymptotic Homogenization

FGM may be obtained creating a microstructure into the solid part of the component to form a cellular medium. One way of creating such microstructures is the introduction of regularly spaced holes. More in details, square cells with centrally-placed squared holes are considered in this work (see figure 6.3).

We assume that the solid part of the microstructure is an isotropic material of elastic modulus E and Poisson ratio ν. We also introduce a density field variable $\chi \in [0, 1]$ that is a measure of the dimension of the squared hole a with respect to the dimension of the side l of the cell, as shown in Figure 6.3 :

$$\chi = 1 - \frac{a}{l}. \tag{6.25}$$

Because of the squared holes, the cellular medium can be considered an orthotropic material, for which the (homogenized) elastic tensor $\mathbb{C}^H(\chi)$ at the macroscale is expressed, under the hypothesis of plane stress state, as follows:

$$\mathbb{C}^H(\chi) = \begin{bmatrix} C^H_{11}(\chi) & C^H_{12}(\chi) & 0 \\ C^H_{12}(\chi) & C^H_{22}(\chi) & 0 \\ 0 & 0 & C^H_{66}(\chi) \end{bmatrix}. \tag{6.26}$$

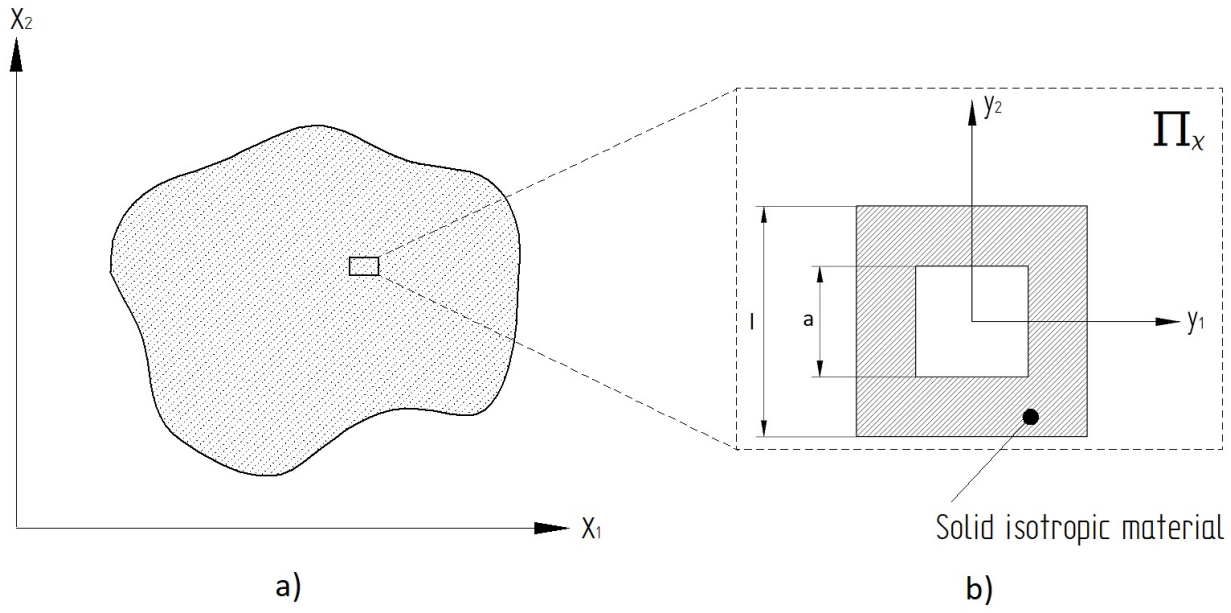

Figure 6.3: a) Schematic representation of the FGM; b) microstructure consisting of square cells with centrally-placed squared holes (RVE).

Given a value of χ, we evaluate the components of $\mathbb{C}^H(\chi)$ considering an asymptotic homogenization procedure for which the Representative Volume Element (RVE) is the square cell with the squared hole. The RVE is denoted in the following by Π_χ and its area by Y_χ. A Cartesian coordinate system $\{y_1, y_2, y_3\}$ is introduced in Π_χ, with the origin in the center of the RVE.

According to the relation of equation (6.26), only three components of $\mathbb{C}^H(\chi)$ have to be evaluated, namely $C^H_{11}(\chi)$, $C^H_{12}(\chi)$ and $C^H_{66}(\chi)$, since from symmetry considerations it results that $C^H_{11}(\chi) = C^H_{22}(\chi)$. The equations that allow to obtain the homogenized material tensor components, under the hypotheses of linear elastic behavior and small strain approximation used for the RVE are:

$$C^H_{11} = C^H_{22} = \frac{1}{Y_\chi}\frac{E}{1-\nu^2}\int_{\Pi_\chi}\left[1-\tilde{\varepsilon}_{11}(\mathbf{y})-\nu\tilde{\varepsilon}_{22}(\mathbf{y})\right]d\mathbf{y} \tag{6.27a}$$

$$C^H_{12} = \frac{1}{Y_\chi}\frac{E}{1-\nu^2}\int_{\Pi_\chi}\left[\nu-\tilde{\varepsilon}_{11}(\mathbf{y})-\nu\tilde{\varepsilon}_{22}(\mathbf{y})\right]d\mathbf{y} \tag{6.27b}$$

$$C^H_{66} = \frac{1}{Y_\chi}\frac{E}{2(1+\nu)}\int_{\Pi_\chi}\left[1-\tilde{\gamma}_{12}(\mathbf{y})\right]d\mathbf{y} \tag{6.27c}$$

In equation (6.27) $\tilde{\varepsilon}_{11}(\mathbf{y})$, $\tilde{\varepsilon}_{22}(\mathbf{y})$ and $\tilde{\gamma}_{12}$, are the microscopic strain fields occurring in the RVE, with applied periodicity boundary conditions, and resulting from the application of specific macroscopic strain histories $\bar{\varepsilon}_{ij}$. More in detail, the strain histories $\bar{\varepsilon}_{11}$, $\bar{\varepsilon}_{22}$ and $\bar{\gamma}_{12}$ applied for equations (6.27a) to (6.27c) respectively, are shown in figure 6.4. Equation (6.27) have been numerically solved by Finite Element Analises (FEA) in Hassani and Hinton [1998].

In FGM the value of the density field variable χ is allowed to continuously vary on the whole structure. In order to perform topology optimization using the model involving a material with

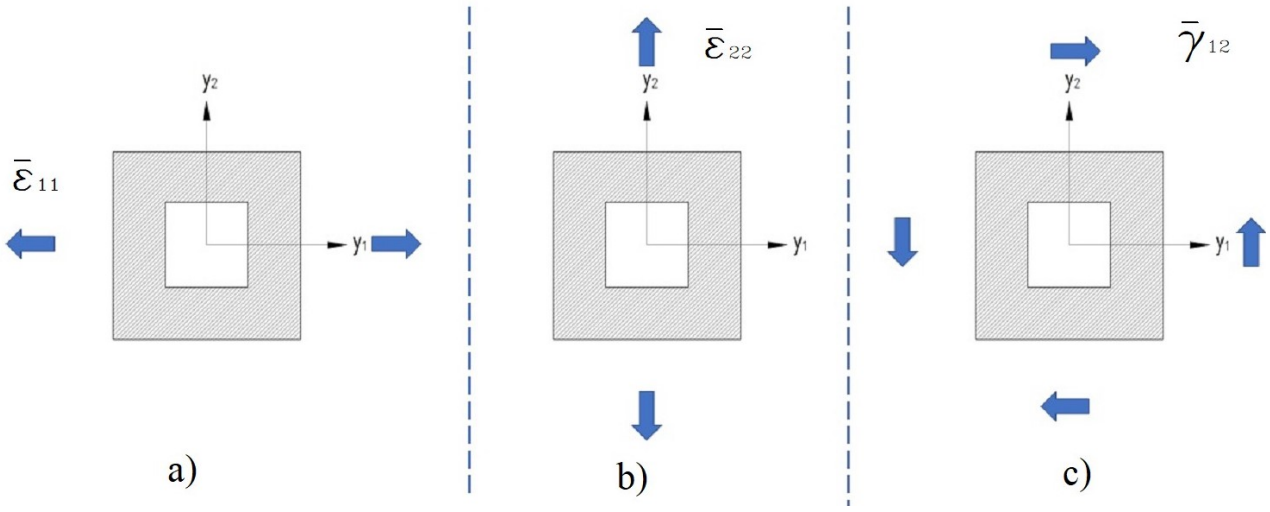

Figure 6.4: Macroscopic strain histories applied to the RVE for the evaluation of the components of the homogenized material tensor $\mathbb{C}^H(\chi)$. a) $\bar{\varepsilon}_{11}$, b) $\bar{\varepsilon}_{22}$, c) $\bar{\gamma}_{12}$

square micro cells, we need to determine the functional relationship between the constitutive matrix $\mathbb{C}^H$ components and the field variable χ, i.e. to construct $\mathbb{C}^H(\chi)$. To this aim, a table of 11 equally spaced sampling points representing 11 values of χ was extracted from Hassani and Hinton [1998]. Finally, we use a least squares approximation polynomial fitting to find the elements of the homogenized elasticity matrix $\mathbb{C}^H(\chi)$ in a continuous form, relying on the discrete values obtained at the sampling points.

State Equation

Let us consider a domain, $\Omega \subset \mathbb{R}^d$ where a material is distributed by means of two phase field variables: $\phi \in [0,1]$ and $\chi \in [0,\phi]$, where $\phi \equiv 0$ corresponds to voids and $\phi \equiv 1$ indicates bulk material, while χ continuously varies within the structure such that it can be considered as a measure of the relative density in the domain regions ($\phi \neq 0$).

We aim at solving a linear elastic problem formulated as follows:

$$\operatorname{div}(\boldsymbol{\sigma}(\phi,\chi)) = \mathbf{0} \quad \text{in} \quad \Omega \tag{6.28a}$$
$$\mathbf{u} = \mathbf{0} \quad \text{on} \quad \Gamma_D \tag{6.28b}$$
$$\boldsymbol{\sigma}(\phi,\chi)\cdot\mathbf{n} = \mathbf{g} \quad \text{on} \quad \Gamma_N \tag{6.28c}$$
$$\boldsymbol{\varepsilon}(\mathbf{u}) = \operatorname{sym}(\nabla\mathbf{u}) \quad \text{in} \quad \Omega \tag{6.28d}$$
$$\boldsymbol{\sigma}(\phi,\chi) = \mathbb{C}(\phi,\chi)\colon \boldsymbol{\varepsilon}(\mathbf{u}) \quad \text{in} \quad \Omega \tag{6.28e}$$

with $\mathbf{g}$ external load vector, $\mathbf{n}$ the unit normal vector, and with the material tensor $\mathbb{C}(\phi,\chi)$ defined as follows:

$$\mathbb{C}(\phi,\chi) = \mathbb{C}^H(\chi)\phi^3 + \gamma_\phi^2\mathbb{C}^H(\chi)(1-\phi)^3 \tag{6.29}$$

with $\gamma_\phi > 0$.

Graded-material topology optimization as a minimization problem

We want now to define an objective functional which optimizes a structure with an inhomogeneous material distribution. This new graded-material objective functional $\mathcal{J}^M(\phi,\chi,\mathbf{u}(\phi,\chi))$ can be defined as:

$$\mathcal{J}^M(\phi,\chi,\mathbf{u},\boldsymbol{\sigma}) = \int_{\Gamma_N} \mathbf{g}\cdot\mathbf{u}(\phi,\chi)\mathrm{d}\Gamma + \int_\Omega \mathbf{f}\cdot\mathbf{u}(\phi,\chi)\mathrm{d}\Omega$$
$$\kappa_\phi \int_\Omega \left[\frac{\gamma_\phi}{2} \mid \nabla\phi \mid^2 + \frac{1}{\gamma_\phi}\psi_0(\phi)\right]\mathrm{d}\Omega + \kappa_\chi \int_\Omega \frac{\gamma_\chi}{2} \mid \nabla\chi \mid^2 \mathrm{d}\Omega + \kappa_\sigma \int_\Omega F(\boldsymbol{\sigma})\mathrm{d}\Omega,$$

with $\kappa_\phi, \kappa_\chi > 0$ and $\gamma_\chi > 0$. The difference with respect to equation (6.8) consists only in the additional integral term $\gamma_\chi/2\,(\mid \nabla\chi \mid)^2$, which is introduced to penalize the gradient of the density scalar field χ.

Following the same approach described for the single-material case, the global graded-material minimization problem (**CP**) can be now written as follows:

$$\min_{\phi,\chi} \quad \mathcal{J}^M(\phi,\chi,\mathbf{u},\boldsymbol{\sigma}),$$
$$\int_\Omega \boldsymbol{\sigma} \colon \boldsymbol{\varepsilon}(\mathbf{v})\mathrm{d}\Omega = \int_\Omega \mathbf{f}\cdot\mathbf{v}\mathrm{d}\Omega + \int_{\Gamma_N} \mathbf{g}\cdot\mathbf{v}\mathrm{d}\Gamma,$$
$$\mathcal{M}(\phi) = \int_\Omega \phi\mathrm{d}\Omega - m \mid \Omega \mid = 0,$$

where $\phi, \chi \in H^1(\Omega)$, under the constraint

$$0 \le \phi \le 1 \qquad \text{a.e. in } \Omega,$$

and the additional constraint on χ:

$$0 \le \chi \le \phi \quad \text{a.e. in } \Omega.$$

We can now define the graded-material Lagrangian $\mathcal{L}^M$ as:

$$\mathcal{L}^M(\phi,\chi,\lambda,\mathbf{u},\boldsymbol{\sigma},\mathbf{U},\boldsymbol{\Sigma}) =$$
$$\mathcal{J}^M(\phi,\chi,\mathbf{u},\boldsymbol{\sigma}) + \lambda\mathcal{M}(\phi) + \mathcal{S}^M(\phi,\chi,\mathbf{u},\boldsymbol{\sigma},\mathbf{U},\boldsymbol{\Sigma}),$$

where, the adjoint operator $\mathcal{S}^M$ for the graded-material formulation is calculated as:

$$\mathcal{S}^M(\phi,\chi,\mathbf{u},\boldsymbol{\sigma},\mathbf{U},\boldsymbol{\Sigma}) =$$
$$-\int_\Omega \boldsymbol{\sigma}\colon\boldsymbol{\varepsilon}(\mathbf{U})\mathrm{d}\Omega + \int_{\Gamma_N}\mathbf{g}\cdot\mathbf{U}\mathrm{d}\Gamma + \int_\Omega \mathbf{f}\cdot\mathbf{U}\mathrm{d}\Omega + \int_\Omega \left(\boldsymbol{\sigma} - \mathbb{C}(\phi,\chi)\colon\boldsymbol{\varepsilon}(\mathbf{u})\right)\boldsymbol{\Sigma}\mathrm{d}\Omega,$$

Analogously to the previously introduced set of admissible controls Φ_{ad} for the phase-field variable ϕ, we define now the set of admissible controls Ξ_{ad} for the grading variable χ as:

$$\Xi_{ad} := \{\chi \in H^1(\Omega) \,:\, 0 \le \chi \le \phi \quad \text{a.e. in } \Omega\}.$$

Clearly, also in the graded-material case we want that the optimal control solutions $\bar{\phi}$ and $\bar{\chi}$ have to satisfy the first order necessary optimality conditions, which can be derived as:

$$D_\phi\mathcal{L}^M(\bar{\phi},\bar{\chi},\bar{\mathbf{u}},\bar{\boldsymbol{\sigma}},\bar{\mathbf{U}},\bar{\boldsymbol{\Sigma}})\left(\phi-\bar{\phi}\right) \le 0 \quad \forall\phi\in\Phi_{ad}$$

and

$$D_\chi \mathcal{L}^M(\bar{\phi}, \bar{\chi}, \bar{\mathbf{u}}, \bar{\boldsymbol{\sigma}}, \bar{\mathbf{U}}, \bar{\boldsymbol{\Sigma}})\,(\chi - \bar{\chi}) \leq 0 \quad \forall \chi \in \Xi_{ad},$$

where $\bar{\mathbf{u}}$ and $\bar{\mathbf{U}}$ are solutions of the graded-material state equation (6.28) and of the corresponding adjoint problem, respectively. For a complete analysis of necessary first order optimality conditions we refer to the results reported in appendix D.

Analogously to the single-material case, we can define the energy density of the system and its derivatives w.r.t. both the material phase-field variable ϕ and the density variable χ as:

$$\mathcal{E}^M(\phi, \chi, \mathbf{u}) = \boldsymbol{\varepsilon}(\mathbf{u}) : \mathbb{C}(\phi, \chi)\boldsymbol{\varepsilon}(\mathbf{u}),$$

$$\frac{\partial \mathcal{E}^M(\phi, \chi, \mathbf{u})}{\partial \phi} = \boldsymbol{\varepsilon}(\mathbf{u}) : \frac{\partial \mathbb{C}(\phi, \chi)}{\partial \phi}\boldsymbol{\varepsilon}(\mathbf{u}),$$

and

$$\frac{\partial \mathcal{E}^M(\phi, \chi, \mathbf{u})}{\partial \chi} = \boldsymbol{\varepsilon}(\mathbf{u}) : \frac{\partial \mathbb{C}(\phi, \chi)}{\partial \chi}\boldsymbol{\varepsilon}(\mathbf{u}).$$

The optimal control problem can be solved as in the single-material case by means of the Allen-Cahn gradient flow, leading to the following set of equations:

$$\begin{aligned}\frac{\gamma_\phi}{\tau}\int_\Omega (\phi_{n+1} - \phi_n) v_\phi \mathrm{d}\Omega + \kappa_\phi \gamma_\phi \int_\Omega \nabla\phi \cdot \nabla v_\phi \mathrm{d}\Omega + \int_\Omega v_\phi \lambda \mathrm{d}\Omega \\ - \int_\Omega v_\phi \frac{\partial \mathcal{E}^M(\phi_n, \chi_n, \mathbf{u}_n)}{\partial \phi}\mathrm{d}\Omega + \frac{\kappa_\phi}{\gamma_\phi}\int_\Omega \frac{\partial \psi_0(\phi_n)}{\partial \phi} v_\phi \mathrm{d}\Omega = 0,\end{aligned} \tag{6.30}$$

$$\frac{\gamma_\chi}{\tau}\int_\Omega (\chi_{n+1} - \chi_n) v_\chi \mathrm{d}\Omega + \kappa_\chi \gamma_\chi \int_\Omega \nabla\chi \cdot \nabla v_\chi \mathrm{d}\Omega - \int_\Omega v_\chi \frac{\partial \mathcal{E}^M(\phi_n, \chi_n, \mathbf{u}_n)}{\partial \chi}\mathrm{d}\Omega = 0, \tag{6.31}$$

to be solved under the volume constraint

$$\int_\Omega v_\lambda (\phi - m)\mathrm{d}\Omega = 0. \tag{6.32}$$

In order to estimate the total amount of material in the structure, we define a material density fraction index m_χ as:

$$m_\chi = \frac{1}{|\,\Omega\,|}\int_\Omega \chi \mathrm{d}\Omega,$$

which can be considered as a measure of the global amount of material used to print the structure. Correspondingly, we define m_ϕ as the volume fraction index, such that:

$$m_\phi = m = \frac{1}{|\,\Omega\,|}\int_\Omega \phi \mathrm{d}\Omega.$$

Graded-material finite element formulation

We aim now at obtaining a discrete formulation for the graded-material phase-field topology optimization problem. To this end, the displacement field $\mathbf{u}$, the adjoint variable $\mathbf{U}$, the phase-field variable ϕ, the Lagrange multiplier λ and their corresponding variations are approximated using the same discretization already defined in section 6.1.2. Additionally, we need to discretize the material grading variable χ on the domain Ω; such a discretization is obtained introducing an additional mesh $\mathcal{T}_\chi$, such that the material grading variable χ and its variation v_χ can be written as:

$$\chi \approx \mathbf{N}_\chi \tilde{\boldsymbol{\chi}} \qquad \text{and} \qquad v_\chi \approx \mathbf{N}_{v_\chi} \tilde{\mathbf{v}}_\chi,$$

where $\mathbf{N}_\chi$ and $\mathbf{N}_{v_\chi}$ are the piecewise linear shape functions which interpolate the nodal degrees of freedoms $\tilde{\boldsymbol{\chi}}$ and $\tilde{\mathbf{v}}_\chi$, respectively.

The discrete form of equations (6.30) to (6.32) can thus be written in a compact notation as:

$$\frac{1}{\tau}\begin{bmatrix} \mathbf{0} & \mathbf{0} & \mathbf{0} & \mathbf{0} & \mathbf{0} \\ \mathbf{0} & \mathbf{0} & \mathbf{0} & \mathbf{0} & \mathbf{0} \\ \mathbf{0} & \mathbf{0} & \mathbf{M}^{\phi\phi} & \mathbf{0} & \mathbf{M}^{\phi\lambda} \\ \mathbf{0} & \mathbf{0} & \mathbf{0} & \mathbf{M}^{\chi\chi} & \mathbf{0} \\ \mathbf{0} & \mathbf{0} & \mathbf{M}^{\lambda\phi} & \mathbf{0} & 0 \end{bmatrix} \begin{bmatrix} \tilde{\mathbf{u}} \\ \tilde{\mathbf{U}} \\ \tilde{\boldsymbol{\phi}} \\ \tilde{\boldsymbol{\chi}} \\ \tilde{\lambda} \end{bmatrix} + \begin{bmatrix} \mathbf{K}^{\mathbf{uu}} & \mathbf{0} & \mathbf{0} & \mathbf{0} & \\ \mathbf{0} & \mathbf{K}^{\mathbf{UU}} & \mathbf{0} & \mathbf{0} & \mathbf{0} \\ \mathbf{0} & \mathbf{0} & \mathbf{K}^{\phi\phi} & \mathbf{0} & \mathbf{0} \\ \mathbf{0} & \mathbf{0} & \mathbf{0} & \mathbf{K}^{\chi\chi} & \mathbf{0} \\ \mathbf{0} & \mathbf{0} & \mathbf{0} & \mathbf{0} & 0 \end{bmatrix} \begin{bmatrix} \tilde{\mathbf{u}} \\ \tilde{\mathbf{U}} \\ \tilde{\boldsymbol{\phi}} \\ \tilde{\boldsymbol{\chi}} \\ \tilde{\lambda} \end{bmatrix} = \begin{bmatrix} \mathbf{f} \\ \mathbf{F} + \mathbf{q}^\sigma \\ \mathbf{q}^\phi + \mathbf{q}^s + \mathbf{q}^\psi \\ \mathbf{q}^\chi + \mathbf{q}^{s\prime} \\ q^\lambda \end{bmatrix} \tag{6.33}$$

where the newly defined matrix and vector terms are:

$$\mathbf{M}^{\chi\chi} = \gamma_\chi \int_\Omega \mathbf{N}_\chi^T \mathbf{N}_\chi \mathrm{d}\Omega,$$
$$\mathbf{K}^{\chi\chi} = \kappa_\chi \gamma_\chi \int_\Omega \nabla \mathbf{N}_\chi^T \nabla \mathbf{N}_\chi \mathrm{d}\Omega,$$
$$\mathbf{q}^\chi = \frac{\gamma_\chi}{\tau} \int_\Omega \mathbf{N}_\chi^T \mathbf{N}_\chi \tilde{\boldsymbol{\chi}}_n \mathrm{d}\Omega,$$
$$\mathbf{q}^{s\prime} = \int_\Omega \mathbf{N}_\chi^T \frac{\partial \mathcal{E}^M(\tilde{\boldsymbol{\phi}}_n, \tilde{\boldsymbol{\chi}}_n, \tilde{\mathbf{u}}_n)}{\partial \chi} \mathrm{d}\Omega,$$

To obtain a topologically optimized structure with continuously varying material properties, we solve the problem in equation (6.33) employing a staggered iterative approach as described in algorithm 8. In fact, the linear system in equation (6.33) can be split into three linear systems which we solve separately:
the state equation system

$$\mathbf{K}^{\mathbf{uu}} \tilde{\mathbf{u}} = \mathbf{f}, \tag{6.34}$$

the adjoint problem system

$$\mathbf{K}^{\mathbf{UU}}\tilde{\mathbf{U}} = \mathbf{F} + \mathbf{q}^{\sigma}, \tag{6.35}$$

and the phase-field system

$$\frac{1}{\tau}\begin{bmatrix}\mathbf{M}^{\phi\phi} & \mathbf{0} & \mathbf{M}^{\phi\lambda}\\ \mathbf{0} & \mathbf{M}^{\chi\chi} & \mathbf{0}\\ \mathbf{M}^{\lambda\phi} & \mathbf{0} & 0\end{bmatrix}\begin{bmatrix}\tilde{\boldsymbol{\phi}}\\ \tilde{\boldsymbol{\chi}}\\ \tilde{\lambda}\end{bmatrix} + \begin{bmatrix}\mathbf{K}^{\phi\phi} & \mathbf{0} & \mathbf{0}\\ \mathbf{0} & \mathbf{K}^{\chi\chi} & \mathbf{0}\\ \mathbf{0} & \mathbf{0} & 0\end{bmatrix}\begin{bmatrix}\tilde{\boldsymbol{\phi}}\\ \tilde{\boldsymbol{\chi}}\\ \tilde{\lambda}\end{bmatrix} = \begin{bmatrix}\mathbf{q}^{\phi} + \mathbf{q}^{s} + \mathbf{q}^{\psi}\\ \mathbf{q}^{\chi} + \mathbf{q}^{s\prime}\\ q^{\lambda}\end{bmatrix}. \tag{6.36}$$

Algorithm 8 describes the iterative procedure to obtain the graded-material optimized structure discussed so far. The adopted solution scheme is very similar to algorithm 6 but in this case we have to solve at each iteration the graded-material linear system defined in equation (6.36) to obtain the material phase-field solution vector $\tilde{\boldsymbol{\phi}}_{n+1}$ and the density field solution vector $\tilde{\boldsymbol{\chi}}_{n+1}$.

Algorithm 8 `graded-material optimization`

Input: $\mathcal{T}_U$, $\mathcal{T}_\phi$, $\mathcal{T}_u$, $\mathcal{T}_\chi$, $\boldsymbol{\phi}_0$, $\boldsymbol{\chi}_0$
Output: Optimal topology

$\boldsymbol{\phi}_n \leftarrow \boldsymbol{\phi}_0$
$\boldsymbol{\chi}_n \leftarrow \boldsymbol{\chi}_0$
while ($\Delta_\phi \geq tol$ or $\Delta_\chi \geq tol$) and $n \leq max_{iter}$ **do**
  $\tilde{\mathbf{u}}_{n+1} \leftarrow$ `solve` 6.34
  $\tilde{\mathbf{U}}_{n+1} \leftarrow$ `solve` 6.35
  $(\tilde{\boldsymbol{\phi}}^*_{n+1}, \tilde{\boldsymbol{\chi}}^*_{n+1}, \tilde{\lambda}_{n+1}) \leftarrow$ `solve` 6.36
  $\tilde{\boldsymbol{\phi}}_{n+1} \leftarrow$ `rescale` $\left(\tilde{\boldsymbol{\phi}}^*_{n+1}, [0,1]\right)$
  $\tilde{\boldsymbol{\chi}}_{n+1} \leftarrow$ `rescale` $\left(\tilde{\boldsymbol{\chi}}^*_{n+1}, [0,\phi]\right)$
  `update`(Δ_ϕ)
  $\boldsymbol{\phi}_n \leftarrow \boldsymbol{\phi}_{n+1}$
  $\boldsymbol{\chi}_n \leftarrow \boldsymbol{\chi}_{n+1}$
end while

6.2 Numerical and Experimental Results

In this section, we first present a verification benchmark to asses the accuracy of the assumptions made for asymptotic homogenization. Secondly, we discuss numerical end experimental results obtained for a classical benchmark example of topology optimization literature, namely the MBB-beam problem. We also report numerical results for two three-dimensional examples, the 3D MBB-beam and the L-bracket problem. In the 3D examples the asymptotic homogenization described in section 6.1.3 is not used, instead the bulk material tensor is simply linearly scaled using the density variable χ, such that:

$$\mathbb{C}(\phi, \chi) = \chi\mathbb{C}_b\left(\phi^3 + \gamma_\phi^2(1-\phi)^3\right). \tag{6.37}$$

The presented results are obtained using an *in-house* developed software written in FEniCS, an open source library to automate the solution of mathematical models based on differential equations, we refer to Logg et al. [2012] for further information on FEniCS framework.

6.2.1 Verification of the asymptotic homogenization assumption

To estimate the modeling error introduced by asymptotic homogenization we study the simple numerical benchmark described in figure 6.5. We apply a load $g = 100[N/mm]$ and we evaluate the compliance and the maximum displacement in x-direction $u_{x,max}$ of the specimen. We consider domains with microstructure having different cell size (see figure 6.6) and the corresponding homogenized structure. Table 6.1 reports the results obtained for three different density fraction $\rho_f = \rho_{str}/\rho_{bulk} = 0.25, 0.5$ and 0.75, where $\rho_{bulk} = 7850[N/m^3]$ is the density of the bulk material and ρ_{str} the actual density of the structure. It can be observed that for lower density fraction the error of the homogenized model increases. This effect is due to both boundary effects and an intrinsic modeling error which we introduced with the asymptotic homogenization assumptions. Nevertheless, due to the extremely high computational costs of simulations resolving a time evolving microstructure domain, we can consider the homogenized model a sufficiently good trade-off between accuracy and computational efforts.

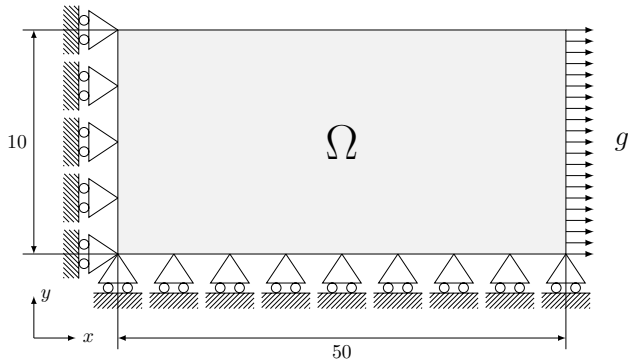

Figure 6.5: One-quarter traction test. All units are in mm.

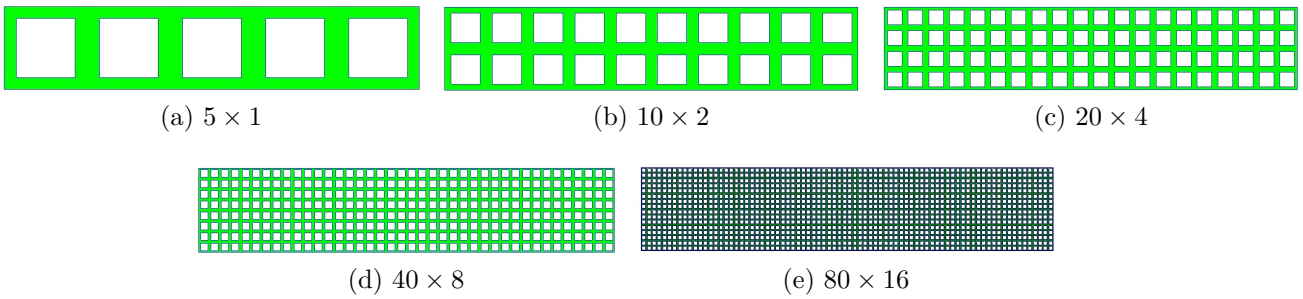

(a) 5×1 (b) 10×2 (c) 20×4

(d) 40×8 (e) 80×16

Figure 6.6: Microstructure domains with different cell sizes and density fraction $\rho_f = 0.5$.

Table 6.1: Compliance and max. displacement value of different microstructures and corresponding homogenized material.

ρ_f	0.25			0.75			0.5		
♯cells	♯DOFs	$\mathcal{C}$	$u_{x,max}$	♯DOFs	$\mathcal{C}$	$u_{x,max}$	♯DOFs	$\mathcal{C}$	$u_{x,max}$
5x1	30346	496.0	0.78	26288	48.1	5.31E-02	59564	103.0	1.29E-01
10x2	30788	295.5	0.45	82262	46.5	4.91E-02	58482	89.0	1.04E-01
20x4	36376	203.4	0.24	252262	45.8	4.71E-02	60544	82.9	8.99E-02
40x8	144558	188.44	0.21	333984	45.3	4.60E-02	66082	79.2	8.21E-02
80x16	819714	185.4	0.20	339608	44.5	4.48E-02	111350	76.6	7.86E-02
hom	402402	169.0	0.17	402402	44.8	4.47E-02	402402	79.7	7.97E-02

6.2.2 Two dimensional MBB

We apply the phase-field topology optimization procedure described in section 6.1 to the MMB-beam problem described in figure 6.7. We set $g = 25$ N and we consider the RGD851 rigid polymer from Stratasys, having elastic modulus $E = 2300$ MPa and a Poisson ratio $\nu = 0.3$. The volume filling ratios are $m_\phi = 0.7$ and $m_\chi = 0.4$. In order to satisfy the machine manufacturing constraints, which do not allow to print infinitely small thicknesses, we set a minimum value for the density parameter $\chi_{min} = 0.29$, such that $\chi \in [\chi_{min}, \phi]$ where $\phi \neq 0$. The evolution of the density phase-field variable χ at different time steps is shown in figure 6.8.

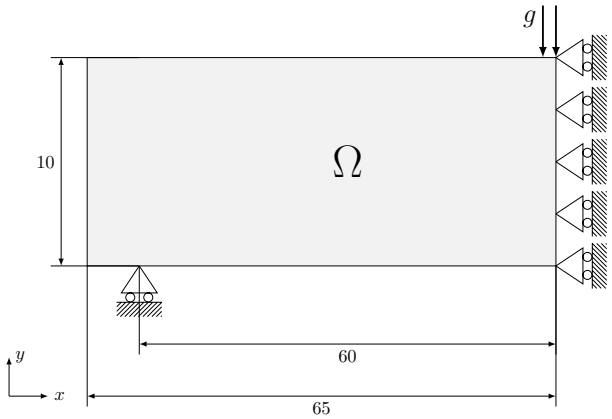

Figure 6.7: Two dimensional MBB: half-domain setup.

From numerics to 3D printing

In order to convert the result of figure 6.8f into printable data we implemented the following procedure:

1. Choose the shape and the size of the microstructure cells. In this work we choose squared cells with dimensions fulfilling technological requirements such as the minimum print-

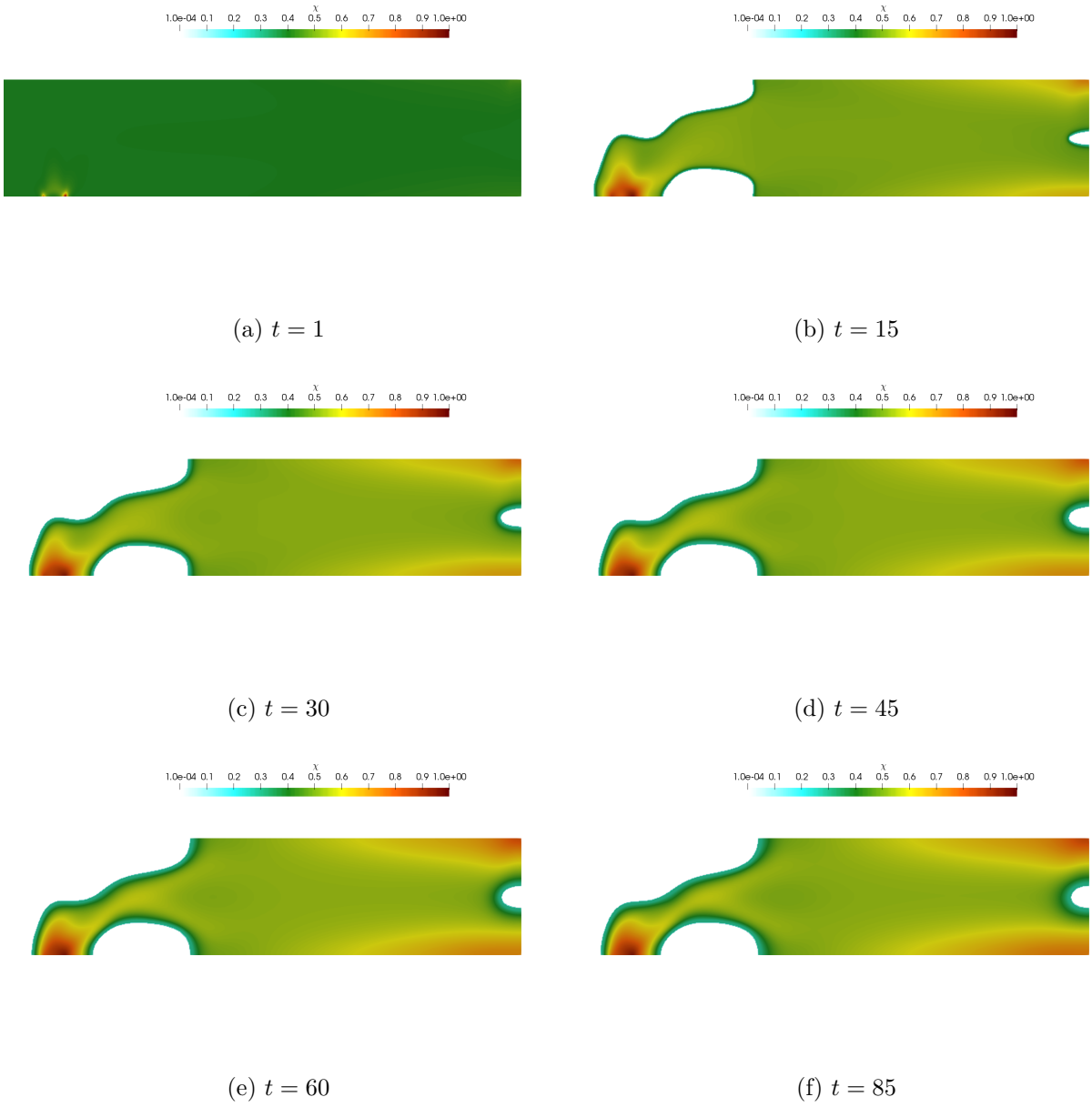

(a) $t = 1$ (b) $t = 15$

(c) $t = 30$ (d) $t = 45$

(e) $t = 60$ (f) $t = 85$

Figure 6.8: Two dimensional MBB: Evolution of the density variable χ at different time steps t.

able thickness and hole dimension. The dimension of the cell $l = 1\,mm$ is determined according to the resolution capability of the Connex 3 3D-printer;

2. Generate a Cartesian grid Λ_χ over the domain Ω with a constant size equal to the cell dimension;
3. Evaluate the average value $\bar{\chi}$ within each cell of Λ_χ;
4. Generate a cuboid for each cell of Λ_χ; each cuboid results from the extrusion of a square of side equal to a, evaluated through equation (6.25). Each cuboid represents the void that has to be introduced to create the microstructure;
5. Generate an high resolution Cartesian grid Λ_ϕ over the domain Ω with a constant size

equal to the finite element mesh dimension; for each cell of Λ_ϕ the corresponding value of the field variable ϕ is assigned. For each cell, if the value of $\phi > \xi$ a cuboid is generated, being ξ a threshold value;

6. By means of a boolean operation subtract the solid obtained at step 4 from the solid obtained at step 5.

This procedure is implemented in *Mathematica* such that we have obtained a complete conversion pipeline within a single numerical framework.

The complete process, from analysis to 3D printing is described in figure 6.9 where the main steps of this method are highlighted. Finally, we print the final structure using the *260 Connex 3*® available at the laboratories of the University of Pavia.

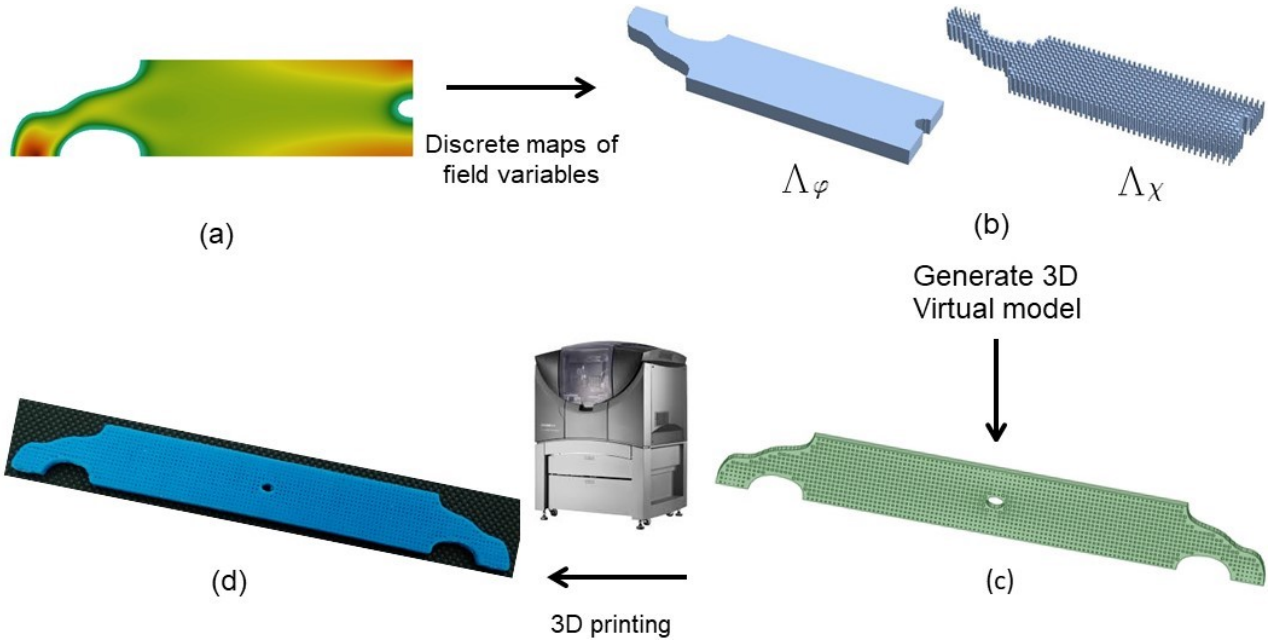

Figure 6.9: A complete pipeline from a continuously graded numerical solution to a 3D printed FGM structure; a) phase-field based topology optimization, b) generation of 3D virtual model from the discrete maps of the field variables, c) finished 3D virtual model, d) 3D-printed part

Experimental results

With this experimental measurements we aim at assessing the higher mechanical properties (e.g., stiffness) which topologically optimized structures can achieve compared to lattice structures having the same weight but constant density. We printed five different specimens: 3 using the optimized model and 2 constant density beams. One of the optimized specimen was used to calibrate the machine, thus we report results only of 4 measurements. Figure 6.10 shows the two different kind of specimens (constant density and FGM) in the testing machine. We perform a 3-point bending test and measure the maximum displacement along the axis of symmetry of the structure. The experimental results are reported in figure 6.11. These results clearly show the benefits of performing topology optimization on the mechanical response of the structure: for the same load (50 N) we have more than two times less maximum displacements in the optimized specimen than in the constant density one.

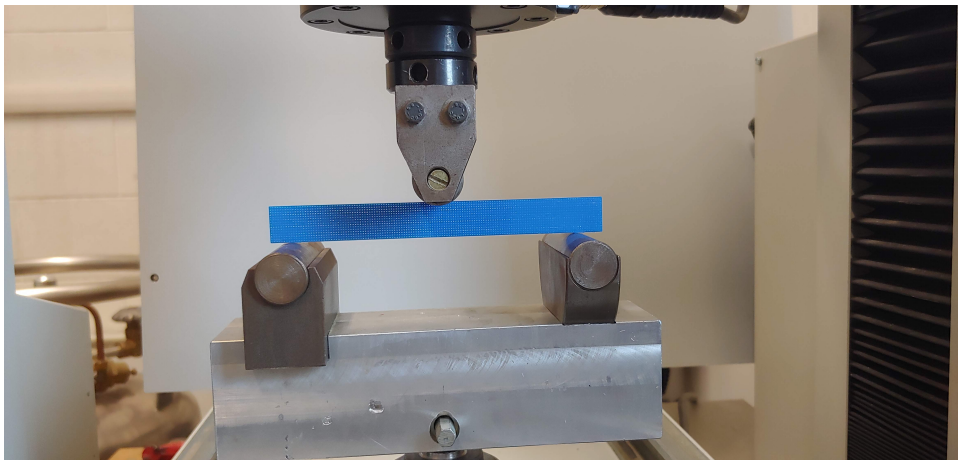

(a) Constant density specimen

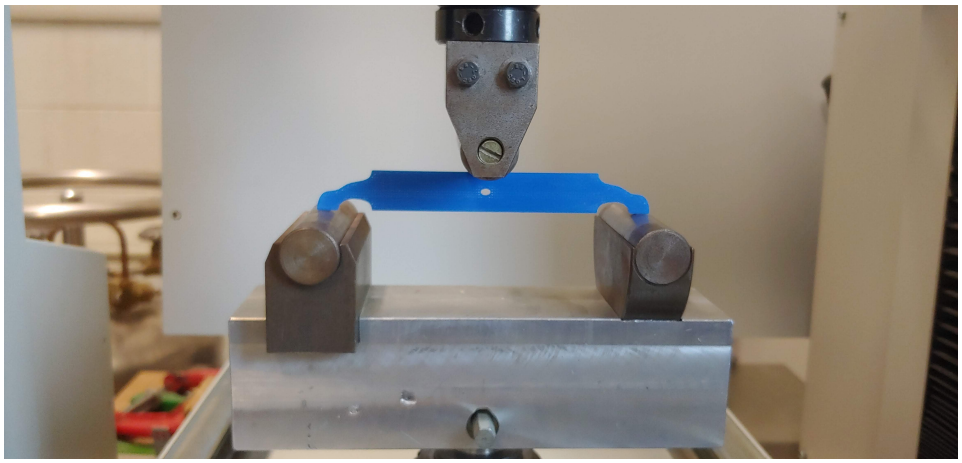

(b) FGM topologically optimized specimen

Figure 6.10: Specimens used in the experiment.

6.2.3 Three dimensional MBB

We now extend the numerical results of section 6.2.2 to the three-dimensional problem described in figure 6.12. As in section 6.2.2, we set $g = 25$ N and we consider the RGD851 rigid polymer from Stratasys, having elastic modulus $E = 2300$ MPa and a Poisson ratio $\nu = 0.3$. We change the volume filling ratio m_ϕ to 0.5 while we keep $m_\chi = 0.4$. We set a minimum value for the density parameter $\chi_{min} = 0.25$, such that $\chi \in [\chi_{min}, \phi]$ where $\phi \neq 0$. The evolution of the material phase-field variable ϕ at different time steps is shown in figure 6.13, while the evolution of the density phase-field variable χ at different time steps is depicted in figure 6.14. Both these results proof that the algorithm converges quite fast to the final solution, as we can also observe from the compliance evolution reported in figure 6.15. Finally, figure 6.16 shows the complex internal topology and density distribution obtained at the end of the optimization procedure.

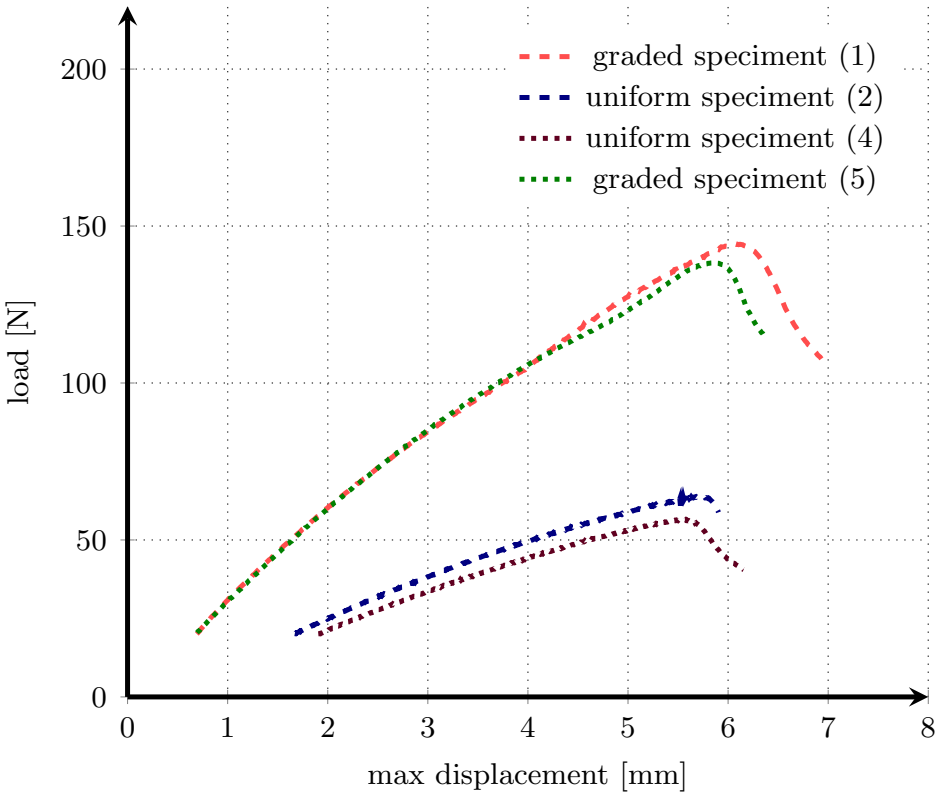

Figure 6.11: Load vs displacements plot.

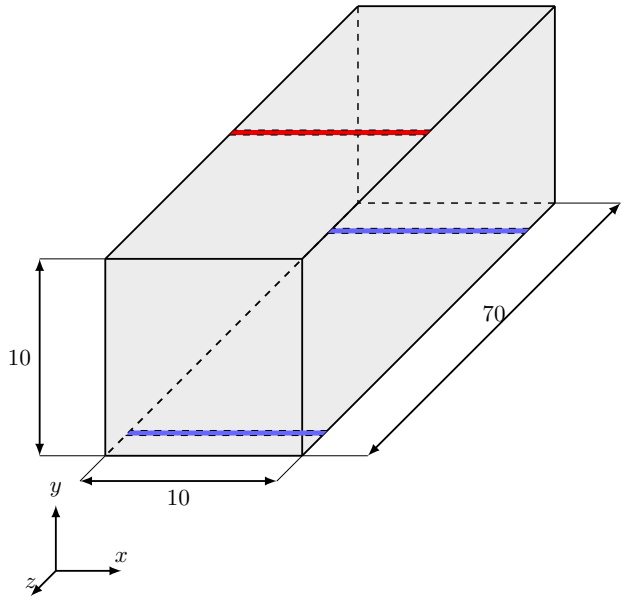

Figure 6.12: Three dimensional MBB: domain setup. The red area indicates the surface where the load is applied, while the blue areas the surfaces where Dirichlet BCs are aplied

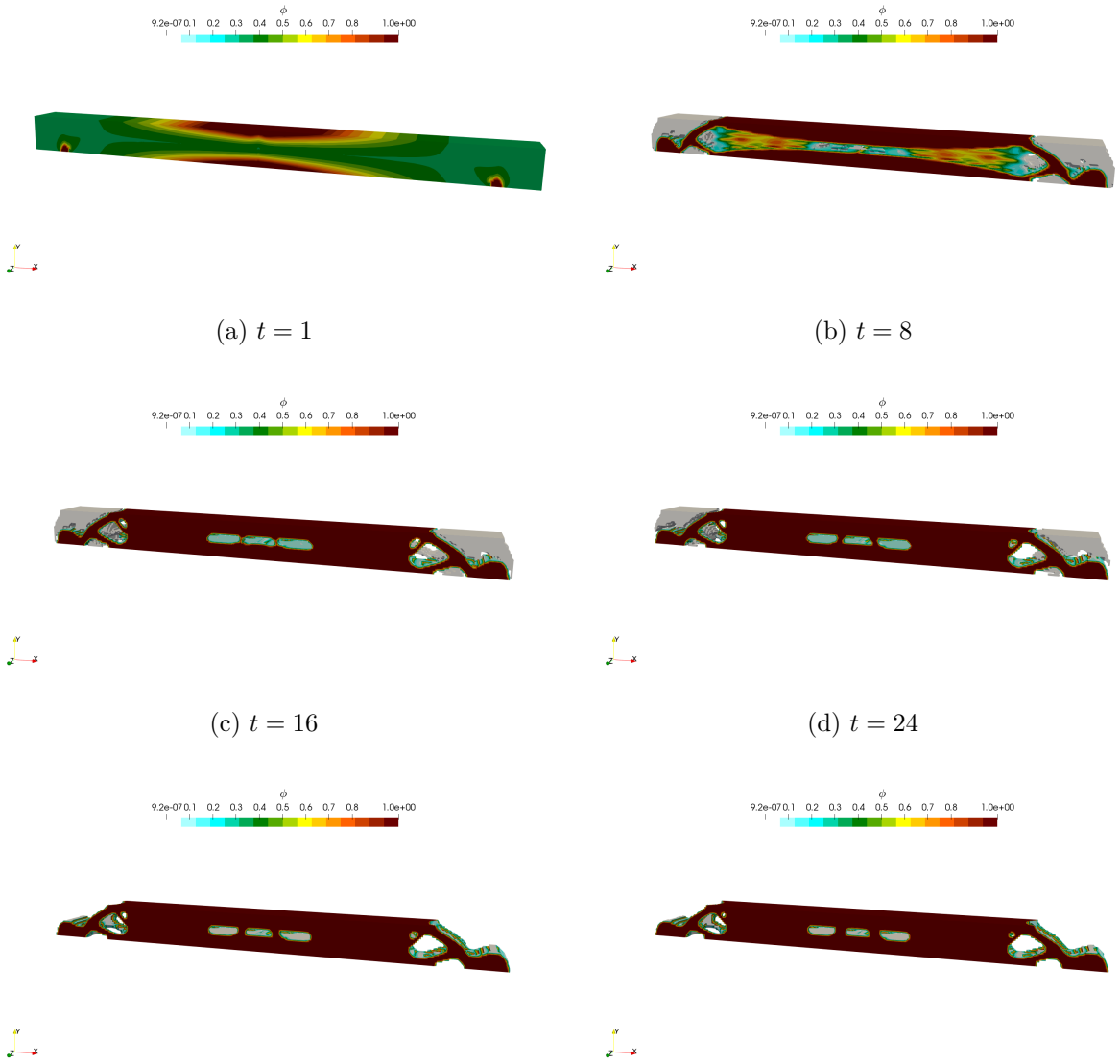

(a) $t = 1$ (b) $t = 8$

(c) $t = 16$ (d) $t = 24$

(e) $t = 32$ (f) $t = 49$

Figure 6.13: Three dimensional MBB: Evolution of the material variable ϕ at different time steps t.

6.2.4 L-bracket design

As a last numerical example we consider another classical benchmark from topology optimization literature: the L-bracket problem depicted in figure 6.17, where a load is applied at the lower-right corner (red surface) of the structure which is clamped at the upper face (blue area). We employ the same material and optimization parameters used in section 6.2.3. Figure 6.18 shows the evolution of the density variable, while the final topology is reported in figure 6.19 and the corresponding Von Mises stresses are shown in figure 6.20. In figure 6.21 the compliance value at each iteration is plotted. From this figure, we can observe that the algorithm converges to the optimal solution in few iterations. These results confirm the robustness and

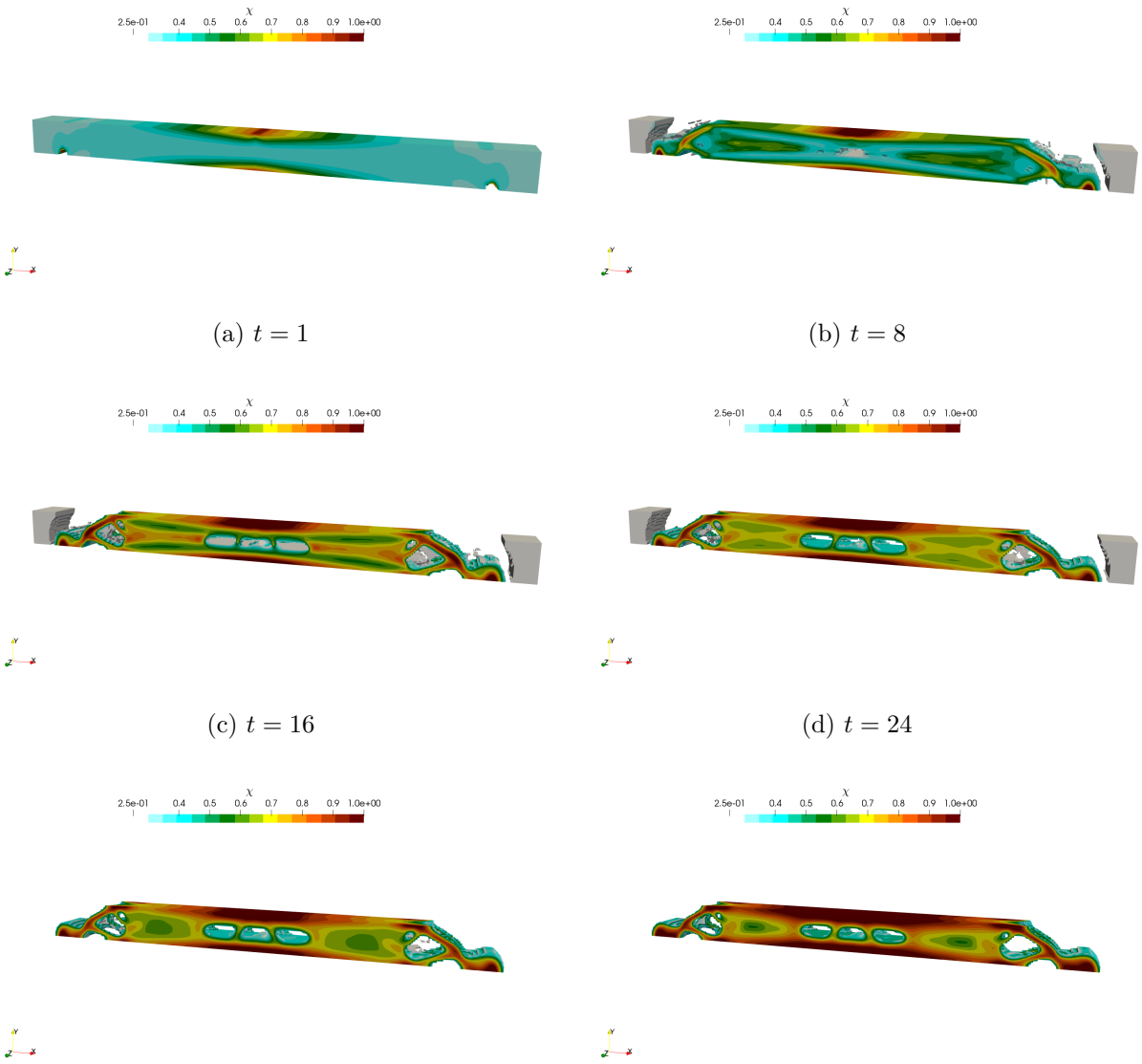

(a) $t = 1$ (b) $t = 8$

(c) $t = 16$ (d) $t = 24$

(e) $t = 32$ (f) $t = 49$

Figure 6.14: Three dimensional MBB: Evolution of the density variable χ at different time steps t.

efficiency of the proposed optimization procedure for 3D problems.

6.3 Summary and further outlooks

We have presented a complete pipeline to obtain from numerical results a 3D printed FGM structure. In particular, we employ the phase-field method together with asymptotic homogenization for the analysis and the topological optimization of 2D plane stress structures, whereas an *in-house* developed Mathematica code is used to convert the density map into a 3D virtual model suitable for 3D printing.

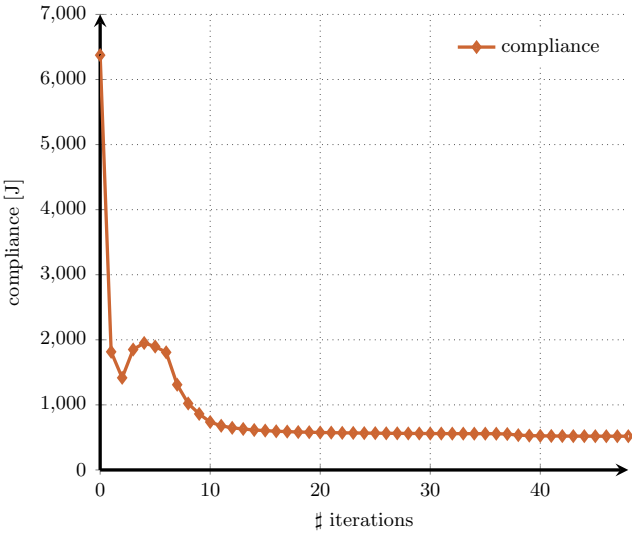

Figure 6.15: Three dimensional MBB: compliance evolution.

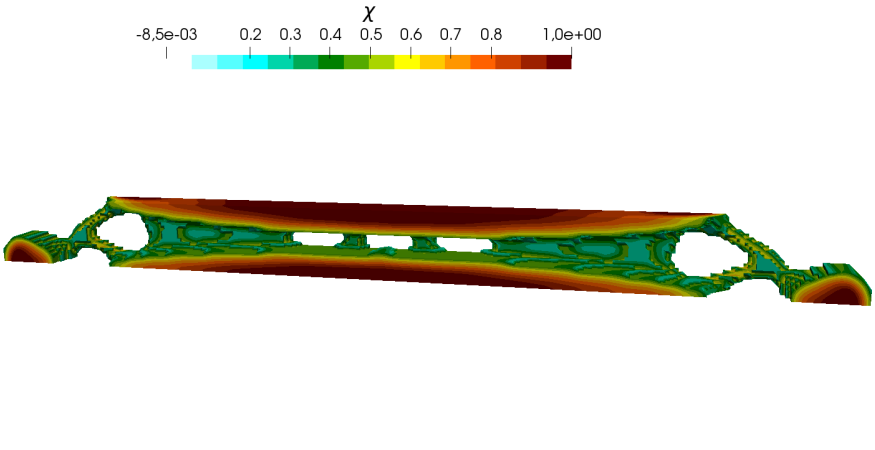

Figure 6.16: Three dimensional MBB: density distribution of optimized structure. Longitudinal plane clip.

As a validation benchmark we investigate an MBB-beam problem for plane stress structure. The resulting optimized structure is printed and measured experimentally. Measurements data are compared with a similar beam structure with constant density and equal weight. Experimental evidences show that-for a fixed weight of the structure-FGMD obtained by means of the presented methodology are more effective in terms of stiffness with respect to an analogous lattice structure with constant density.

This experimental results show that the phase-field approach can be useful in case of FGMD optimization. In fact, contrary to similar methods present in literature, the proposed phase-field based topology optimization allows to not only redistribute the material within a given domain but also to indicate void regions within the original domain, simply by means of an additional degrees of freedom into the problem.

Finally, we tested the phase-field based topology optimization procedure also to 3D benchmark problems, namely the three-dimensional MBB-beam problem and the L-bracket problem.

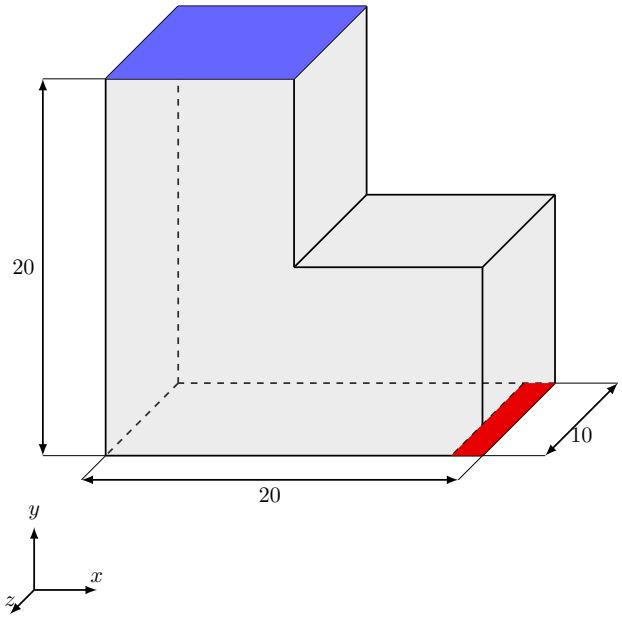

Figure 6.17: L-bracket: domain setup. The red area indicates the surface where the load is applied, while the blue area the clamped surface.

In both these problems the algorithm converged to the optimum in few iterations, showing a robust behavior.

As further outlooks for the present research we aim at extending the complete pipeline to treat 3D structures and at modifying the optimization algorithm such that we can perform mass minimization under both functional constraints (e.g., maximum stress constraint) and technological constraints related to AM processes (e.g., overhang building angles).

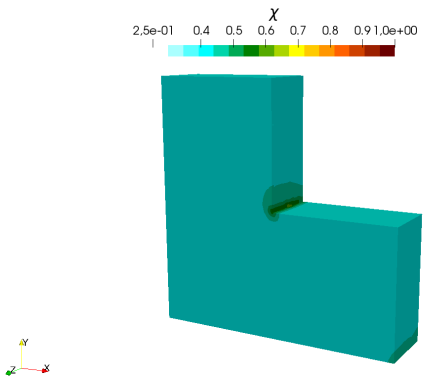

(a) $t = 1$

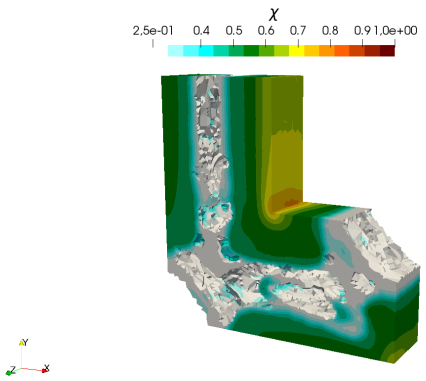

(b) $t = 10$

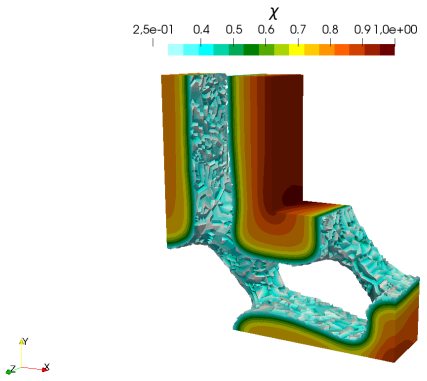

(c) $t = 27$

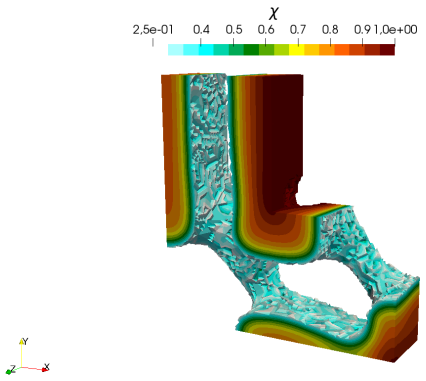

(d) $t = 37$

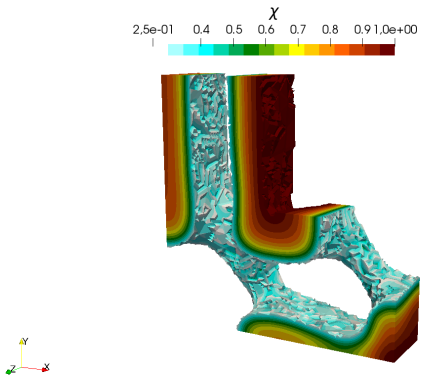

(e) $t = 47$

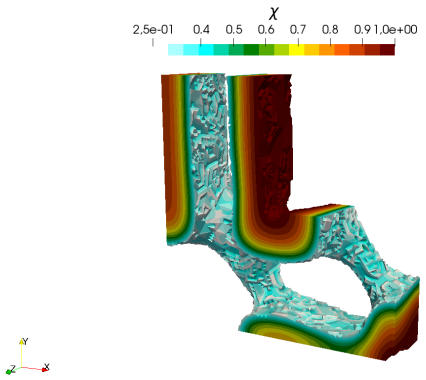

(f) $t = 57$

Figure 6.18: L-bracket: Evolution of the density variable χ at different time steps t. Mid-plane section view.

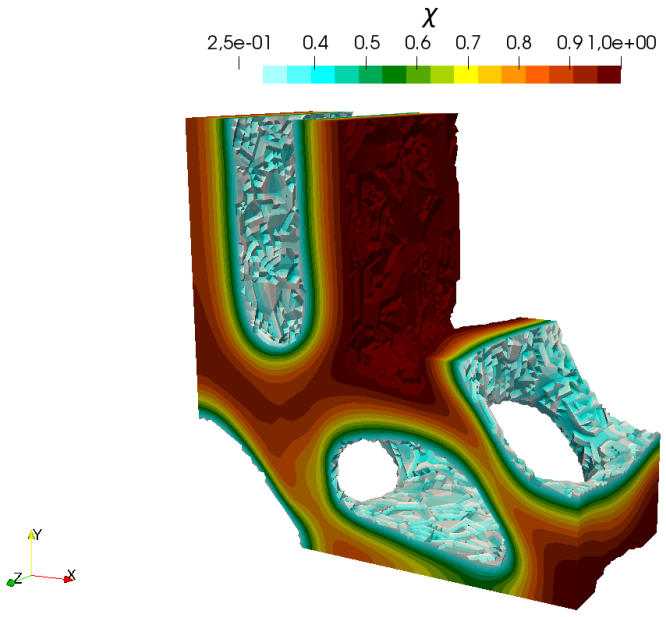

Figure 6.19: L-bracket: density variable χ distribution in the optimized structure.

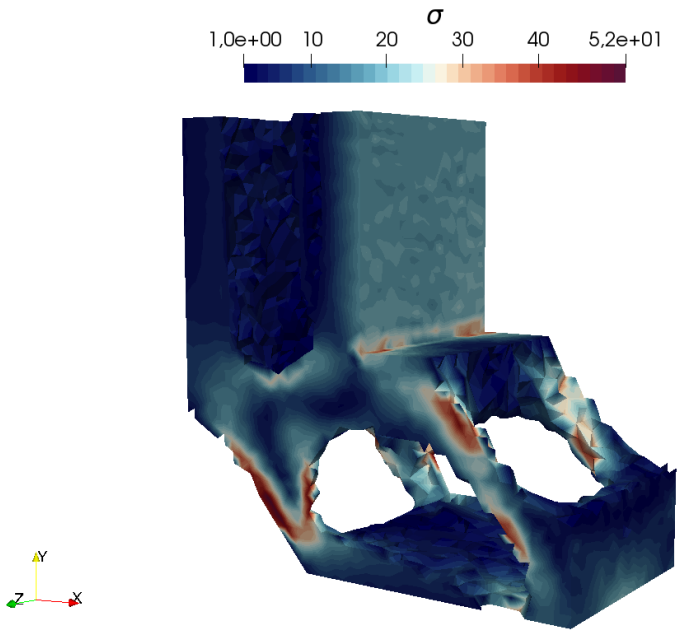

Figure 6.20: L-bracket: Von Mises stress distribution in the optimized structure.

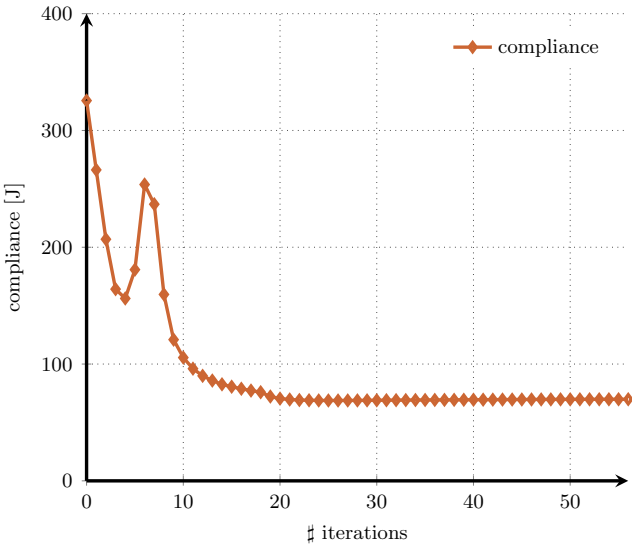

Figure 6.21: L-bracket: compliance evolution.

Chapter 7

Conclusion and outlook

Due to the high heterogeneity of the topics involved, we preferred to discuss most of the conclusions and possible further outlooks of the results presented in this work within each single chapter. Therefore, in this final chapter we limit to briefly recall the main conclusions of this work trying also to propose possible future perspectives for the research from a more general point of view.

7.1 Summary of scientific conclusions

Since numerical methods are surely a key instrument in understanding, developing, and optimizing AM technologies, in this work we have developed and investigated advanced computational methods suitable to solve AM related issues.

Accordingly, in chapter 2 we have presented and verified a set of algorithms to obtain an admissible, adaptive isogeometric discretization, which has shown an excellent trade-off between numerical accuracy and computational efforts. Admissible adaptive IGA seems to be a promising alternative to traditional discretization technique when localized solution with high gradient occurs, e.g., when we are interested in capturing the melt-pool geometry at the meso-scale.

To obtain an accurate prediction of the temperature field in proximity of the heat affected zone (HAZ), together with an efficient discretization, a robust and validated physical model is required. In chapter 3 we have presented a simple yet effective numerical model to approximate the physical phenomena occurring in the HAZ by means of an anisotropic thermal conductivity model. This model has been validated employing experimental data provided by the National Institute of Standards and Technology, showing a good capability in predicting melt-pool dimensions with respect to different process parameter variations (namely, laser power and velocity).

An interesting application of the physical model presented in chapter 3 is described in chapter 4, where numerical temperature results are used as *ground-truth* solution to control an AM machine through a *feed-back* loop scheme. Comparing pixel-by-pixel numerical results and thermal camera measurements the proposed control scheme is potentially able to obtain a real-time process control on the AM machine. In order to be able to perform operations directly on the pixel data coming from the thermal camera, we have developed a conversion procedure, the “inverse measurement” procedure, which allows to translate the continuous,

simulated temperature results into digital signals in the same field of view of the thermal camera.

Beside melt-pool shape prediction, another crucial information which AM industry requires from numerical simulation is the ability to estimate macro-effects on the final artifact which may occur during the AM process. To this end, both the numerical discretization described in chapter 2 and the physical model of chapter 3 are no longer valid, since they are tailored to resolve smaller scales, becoming computationally unaffordable when we are interested in part-scale results. Therefore, in chapter 5 we have introduced a different discretization technique, based on the Finite Cell Method and a simpler physical model which can capture averaged effects occurring during the process. Clearly, we pay a price in terms of accuracy, but this methodology shows the capability to combine a good geometric description with the possibility to compute large scale thermal problems within a reasonable computational time.

Optimal design for additive manufacturing is surely one of the most attractive topics combining together numerical method and AM technology. In this work, we have focused our attention on the so called functionally graded material design, which aims at manufacturing components with properties varying in an almost continuous fashion. In chapter 6 we have presented a numerical procedure to perform topology optimization of functionally graded material structures. This numerical scheme combines the phase-field method and asymptotic homogenization to obtain an efficient optimization tool of FGM components. Once the optimized graded material distribution is obtained, we need to convert the numerical results into a printable 3D virtual model. To this end, we have developed a procedure based on structural cells having variable filling ratio to map the continuous density distribution to a cellular structure. This computational framework has been validated with success for plane-stress structures. Furthermore, chapter 6 shows results obtained applying the topology optimization algorithm also to a 3D problem, but in this case we limit to report the optimized continuous density field, while conversion to a 3D virtual model is left to future investigations.

7.2 Future research

The possible interactions between computational methods and AM technologies are potentially unlimited, and in this work we have presented only a partial overview of potential usages of numerical analysis in AM applications. From the results discussed herein emerges that the complex problems posed by AM technology cannot be faced employing conventional and well-established computational methods. To address the new challenges presented by AM, it becomes of utmost importance to research and investigate new techniques.

Moreover, the considered problems are so complex which cannot be tackled by a single discipline; e.g., we have seen how numerical simulations can be fruitfully employed to develop more efficient process control schemes, or as CAD model generation can be driven by numerical optimization procedures due to the greater design flexibility introduced by AM.

Limiting this discussion to the topic addressed in this work, there are few general points which might be mentioned as possible further developments of the presented results.

Since both numerical discretization techniques and physical models are strongly dependent on the problem scale we are looking at (as we have described in chapter 3), validation procedures can be helpful not only to assess the robustness and the validity of a physical model but also to find its limits. Therefore, further experimental validations are required to highlight

the limits of the proposed models and, at the same time, to provide valuable information on how to possibly improve the presented numerical and physical models.

Another direction which surely requires to be deeply investigated is the possible interaction between measurements and simulations. So far, these two fields have been rarely integrated, but the complex issues presented by AM call for a deeper interaction between metrology and numerical science. We believe that further investigations in this direction might lead to interesting results.

Finally, the results we have obtained applying phase-field method for the optimization of FGM components look very promising and surely need to be further developed. In a first instance, the mapping algorithm needs to be extended to 3D problems, such that the experimental validation, successfully obtained for a plane stress structure, could be replicated for 3D cases. Secondly, different cell structures should be considered and eventually also anisotropic cells should be investigated. Moreover, different AM technology (e.g., metal 3D printing) should also be considered since the resulting FGMD strongly depends on the technological boundaries introduced by the machine.

Bibliography

Abedian, A., Parvizian, J., Düster, A., Khademyzadeh, H., and Rank, E. (2013). Performance of Different Integration Schemes in Facing Discontinuities in the Finite Cell Method. *International Journal of Computational Methods*, 10(03):1350002. 00027.

Alaimo, G., Carraturo, M., Rocca, E., Reali, A., and Auricchio, F. (2019). Functionally graded material design for plane stress structures using phase field method. In *Proceeding of the II International Conference on Simulation for Additive Manufacturing*, Sim-AM 2019.

Allaire, G. (2015). A review of adjoint methods for sensitivity analysis, uncertainty quantification and optimization in numerical codes. *Ingénieurs de l'Automobile*, 836:33–36.

Allaire, G. and Francfort, G. A. (1993). A numerical algorithm for topology and shape optimization. *Topology design of structures*, pages 239–248.

Allaire, G. and Kohn, R. V. (1993). Topology optimization for minimum stress design with the homogenization method. *Topology design of structures*, pages 207–218.

Allen, S. M. and Cahn, J. (1979). A microscopic theory for antiphase boundary motion and its application to antiphase domain coarsening. *Acta Metallurgica*, 27(6):1085–1095.

Bathe, K. J. (2007). *Finite element procedures*. Prentice Hall.

Bendsøe, M. P. (2003). *Topology Optimization: Theory, Methods, and Applications*. Springer, Berlin ; New York. 00112.

Bendsøe, M. P. and Kikuchi, N. (1988). Generating optimal topologies in structural design using a homogenization method. *Comput. Methods Appl. Mech. Engrg.*, 71:197–224.

Bendsøe, M. P. and Sigmund, O. (1999). Material interpolation schemes in topology optimization. *Archive of Applied Mechanics 6*, 65:635–654.

Blank, L., Garcke, H., Farshbaf-Shaker, M., and Styles, V. (2014). Relating phase field and sharp interface approaches to structural topology optimization. *ESAIM Control Optim. Calc. Var.*, 20:1025–1058.

Boettinger, W. J., Warren, J. A., Beckermann, C., and Karma, A. (2002). Phase-field simulation of solidification. *Annual Review of Materials Research*, 32(1):163–194.

Bourdin, B. and Chambolle, A. (2003). Design-dependent loads in topology optimization. *ESAIM Contr. Optim.Calc. Var.*, 9:19–48.

Box, G. (1976). Science and Statistics. *Journal of the American Statistical Association*, 71(356):791–799.

Bracco, C., Buffa, A., Giannelli, C., and Vázquez, R. (2019). Adaptive isogeometric methods with hierarchical splines: An overview. *Discrete and Continuous Dynamical Systems*, 39:241–261.

Bracco, C., Giannelli, C., Großmann, D., and Sestini, A. (2018a). Adaptive fitting with THB-splines: Error analysis and industrial applications. *Comput. Aided Geom. Design*, 62:239–252.

Bracco, C., Giannelli, C., and Vázquez, R. (2018b). Refinement algorithms for adaptive isogeometric methods with hierarchical splines. *Axioms*, 7(3):43.

Buffa, A. and Giannelli, C. (2016). Adaptive isogeometric methods with hierarchical splines: Error estimator and convergence. *Mathematical Models and Methods in Applied Sciences*, 26:1–25.

Buffa, A. and Giannelli, C. (2017). Adaptive isogeometric methods with hierarchical splines: Optimality and convergence rates. *Mathematical Models and Methods in Applied Sciences*, 27:2781–2802.

Cahn, J. and Hilliard, J. (1958). Free energy of a nonuniform system. i. interfacial free energy. *J. Chem. Phys.*, 28:258–267.

Carraturo, M., Giannelli, C., Reali, A., and Vázquez, R. (2019a). Suitably graded thb-spline refinement and coarsening: Towards an adaptive isogeometric analysis of additive manufacturing processes. *Computer Methods in Applied Mechanics and Engineering*, 348:660 – 679.

Carraturo, M., Rocca, E., Bonetti, E., Hömberg, D., Reali, A., and Auricchio, F. (2019b). Graded-material design based on phase-field and topology optimization. *Computational Mechanics*.

Celentano, D., Oñate, E., and Oller, S. (1994). A temperature-based formulation for finite element analysis of generalized phase-change problems. *International Journal for Numerical Methods in Engineering*, 37(20):3441–3465.

Cheng, L., Bai, J., and To, A. (2019). Functionally graded lattice structure topology optimization for the design of additive manufactured components with stress constraints. *Computer Methods in Applied Mechanics and Engineering*, 344:334–359.

Chiumenti, M., Lin, X., Cervera, M., Lei, W., Zheng, Y., and Huang, W. (2017a). Numerical simulation and experimental calibration of additive manufacturing by blown powder technology. Part I: thermal analysis. *Rapid Prototyping Journal*, 23(2):448–463.

Chiumenti, M., Neiva, E., Salsi, E., Cervera, M., Badia, S., Moya, J., Chen, Z., Lee, C., and Davies, C. (2017b). Numerical modelling and experimental validation in Selective Laser Melting. *Additive Manufacturing*, 18:171–185.

Cottrell, J., Hughes, T. J. R., and Bazilevs, Y. (2009). *Isogeometric Analysis: Toward Integration of CAD and FEA*. Wiley and Sons.

Cottrell, J. A., Hughes, T. J. R., and Reali, A. (2007). Studies of refinement and continuity in isogeometric structural analysis. *Computer Methods in Applied Mechanics and Engineering*, 196(41):4160–4183.

Craeghs, T., Bechmann, F., Berumen, S., and Kruth, J.-P. (2010). Feedback control of layerwise laser melting using optical sensors. *Physics Procedia*, 5:505–514.

D'Angella, D., Kollmannsberger, S., Rank, E., and Reali, A. (2018). Multi-level Bézier extraction for hierarchical local refinement of Isogeometric Analysis. *Computer Methods in Applied Mechanics and Engineering*, 328:147–174.

de Falco, C., Reali, A., and Vázquez, R. (2011-12). GeoPDEs: A research tool for isogeometric analysis of PDEs. *Advances in Engineering Software*, 42(12):1020–1034.

De Lorenzis, L., Wriggers, P., and Hughes, T. J. R. (2014). Isogeometric contact: a review. *GAMM-Mitteilungen*, 37(1):85–123.

Denlinger, E. R., Gouge, M., Irwin, J., and Michaleris, P. (2017). Thermomechanical model development and in situ experimental validation of the Laser Powder-Bed Fusion process. *Additive Manufacturing*, 16:73–80.

Diaz, A. and Sigmund, O. (1995). Checkboard patterns in layout optimization. *SIAM J. Appl. Math.*, 5:827–863.

Dörfler, W. (1996). A convergent adaptive algorithm for poisson's equation. *SIAM J. Numer. Anal.*, 33:1106–1124.

Dunbar, A. J., Denlinger, E. R., Gouge, M. F., and Michaleris, P. (2016). Experimental validation of finite element modeling for laser powder bed fusion deformation. *Additive Manufacturing*, 12:108–120.

Düster, A., Parvizian, J., Yang, Z., and Rank, E. (2008). The finite cell method for three-dimensional problems of solid mechanics. *Computer Methods in Applied Mechanics and Engineering*, 197(45–48):3768–3782.

Eschenauer, H. and Olhoff, N. (2001). Topology optimization of continuum structures: A review. *ASME. Appl. Mech. Rev.*, 54(4):331–390.

Forsey, D. and Bartels, R. (1988). Hierarchical B-spline refinement. *Comput. Graph.*, 22:205–212.

Fotovvati, B., Wayne, S. F., Lewis, G., and Asadi, E. (2018). A Review on Melt-Pool Characteristics in Laser Welding of Metals. *Advances in Materials Science and Engineering*, 2018:1–18.

Fox, J., Lopez, F., Lane, B., Yeung, H., and Grantham, S. (2016). On the requirements for model-based thermalcontrol of melt pool geometry in laser powder bedfusion additive manufacturing. *Materials Science and Technology 2016, October 23 – 27, 2016, Salt Palace Convention Center, Salt Lake City, Utah USA*.

Garau, E. and Vázquez, R. (2018). Algorithms for the implementation of adaptive isogeometric methods using hierarchical b-splines. *Appl. Numer. Math.*, 123:58–87.

Ghosh, S., Ma, L., Levine, L. E., Ricker, R. E., Stoudt, M. R., Heigel, J. C., and Guyer, J. E. (2018). Single-Track Melt-Pool Measurements and Microstructures in Inconel 625. *JOM*.

Giannelli, C., Jüttler, B., Kleiss, S. K., Mantzaflaris, A., Simeon, B., and Špeh, J. (2016). THB-splines: An effective mathematical technology for adaptive refinement in geometric design and isogeometric analysis. *Computer Methods in Applied Mechanics and Engineering*, 299:337–365.

Giannelli, C., Jüttler, B., and Speelers, H. (2012). THB-spline: The truncated basis for hierarchical splines. *Comp. Aided Geom. Design.*, 29:485–498.

Gibson, I., Rosen, D. W., and Stucker, B. (2015). *Additive Manufacturing Technologies*. Springer-Verlag New York.

Goldak, J., Chakravarti, A., and Bibby, M. (1984). A new finite element model for welding heat sources. *Metallurgical Transactions B*, 15(2):299–305.

Goldak, J. A. and Akhlaghi, M. (2005). *Computational Welding Mechanics*. Springer, New York.

Hassani, B. and Hinton, E. (1998). *Homogenization and structural topology optimization : theory, practice and software*. Springer.

Heigel, J. C. and Lane, B. M. (2017). Measurement of the Melt Pool Length During Single Scan Tracks in a Commercial Laser Powder Bed Fusion Process. *ASME*.

Hennig, P., Ambati, M., De Lorenzis, L., and Kästner, M. (2018). Projection and transfer operators in adaptive isogeometric analysis with hierarchical B-splines. *Computer Methods in Applied Mechanics and Engineering*, 334:313–336.

Hennig, P., Müller, S., and Kästner, M. (2016). Bézier extraction and adaptivite refinement of truncated hierarchical nurbs. *Comput. Methods Appl. Mech. Engrg.*, 305:316–339.

Hughes, T. J. R., Cottrell, J. A., and Bazilevs, Y. (2005). Isogeometric analysis: CAD, finite elements, NURBS, exact geometry and mesh refinement. *Computer Methods in Applied Mechanics and Engineering*, 194(39):4135–4195.

Hughes, T. J. R., Evans, J. A., and Reali, A. (2014). Finite element and nurbs approximations of eigenvalue, boundary-value, and initial-value problems. *Computer Methods in Applied Mechanics and Engineering*, 272:290–320.

Kamensky, D., Hsu, M.-C., Schillinger, D., Evans, J. A., Aggarwal, A., Bazilevs, Y., Sacks, M. S., and Hughes, T. J. R. (2015). An immersogeometric variational framework for fluid structure interaction: Application to bioprosthetic heart valves. *Computer Methods in Applied Mechanics and Engineering*, 284:1005–1053.

Khairallah, S. A., Anderson, A. T., Rubenchik, A., and King, W. E. (2016). Laser powder-bed fusion additive manufacturing: Physics of complex melt flow and formation mechanisms of pores, spatter, and denudation zones. *Acta Materialia*, 108:36–45.

King, W. E., Anderson, A. T., Ferencz, R. M., Hodge, N. E., Kamath, C., Khairallah, S. A., and Rubenchik, A. M. (2015a). Laser powder bed fusion additive manufacturing of metals; physics, computational, and materials challenges. *Applied Physics Reviews*, 2(4):041304.

King, W. E., Anderson, A. T., Ferencz, R. M., Hodge, N. E., Kamath, C., Khairallah, S. A., and Rubenchik, A. M. (2015b). Laser powder bed fusion additive manufacturing of metals; physics, computational, and materials challenges. *Applied Physics Reviews*, 2(4):041304.

Kiss, G., Giannelli, C., Zore, U., Jüttler, B., Großmann, D., and Barner, J. (2014). Adaptive CAD model (re–)construction with THB–splines. *Graphical models*, 76:273–288.

Kollmannsberger, S., Carraturo, M., Reali, A., and Auricchio, F. (2019). Accurate prediction of melt pool shapes in laser powder bed fusion by the non-linear temperature equation including phase changes. *Integrating Materials and Manufacturing Innovation*, 8:167–177.

Kollmannsberger, S., Özcan, A., Baiges, J., Ruess, M., Rank, E., and Reali, A. (2015). Parameter-free, weak imposition of Dirichlet boundary conditions and coupling of trimmed and non-conforming patches. *International Journal for Numerical Methods in Engineering*, 101(9):670–699. 00001.

Kollmannsberger, S., Özcan, A., Carraturo, M., Zander, N., and Rank, E. (2018). A hierarchical computational model for moving thermal loads and phase changes with applications to selective laser melting. *Comput. Math. Appl.*, 75(5):1483–1497.

Körner, C., Attar, E., and Heinl, P. (2011). Mesoscopic simulation of selective beam melting processes. *Journal of Materials Processing Technology*, 211(6):978–987.

Kraft, R. (1997). Adaptive and linearly independent multilevel B–splines. In Le Méhauté, A., Rabut, C., and Schumaker, L. L., editors, *Surface Fitting and Multiresolution Methods*, pages 209–218. Vanderbilt University Press, Nashville.

Kudela, L., Zander, N., Kollmannsberger, S., and Rank, E. (2016). Smart octrees: Accurately integrating discontinuous functions in 3D. *Computer Methods in Applied Mechanics and Engineering*, 306:406–426.

Le, C., Norato, J., Bruns, T., Ha, C., and Tortorelli, D. (2010). Stress-based topology optimization for continua. *Struct Multidisc. Optim.*, 41:605–620.

Lee, E., James, K., and Martins, J. (2012). Stress-constrained topology optimization with design-dependent loading. *Struct Multidisc. Optim.*, 46:647–661.

Lindgren, L. E. (2007). *L.E. Lindgren-Computational Welding Mechanics Thermomechanical and Microstructural Simulations*. Woodhead Publishing Limited and CRC Press LLC.

Lindwall, J., Malmelöv, A., Lundbäck, A., and Lindgren, L.-E. (2018). Efficiency and accuracy in thermal simulation of powder bed fusion of bulk metallic glass. *JOM*, 70(8):1598–1603.

Logg, A., Mardal, K.-A., and Wells, G. N. (2012). *Automated Solution of Differential Equations by the Finite Element Method*.

Loh, G., Pei, E., Harrison, D., and Monzòn, M. (2018). An overview of functionally graded additive manufacturing. *Additive Manufacturing*.

Lorenzo, G., Scott, M., Tew, K., Hughes, T. J. R., and Gomez, H. (2017). Hierarchically refined coarsened splines for moving interface problems, with particular application to phase-field models of prostate tumor growth. *Comput. Methods Appl. Mech. Engrg.*, 319:515–548.

Lu, X., Lin, X., Chiumenti, M., Cervera, M., Hu, Y., Ji, X., Ma, L., Yang, H., and Huang, W. (2019). Residual stress and distortion of rectangular and S-shaped Ti-6Al-4V parts by Directed Energy Deposition: Modelling and experimental calibration. *Additive Manufacturing*, 26:166 – 179.

Lu, X., Lin, X., Chiumenti, M., Cervera, M., Li, J., Ma, L., Wei, L., Hu, Y., and Huang, W. (2018). Finite element analysis and experimental validation of the thermomechanical behavior in laser solid forming of Ti-6Al-4V. *Additive Manufacturing*, 21:30–40.

Lundbäck, A. and Lindgren, L.-E. (2011). Modelling of metal deposition. *Finite Elements in Analysis and Design*, 47(10):1169–1177.

Mani, M., Lane, B., Donmez, A., Feng, S., Moylan, S., and Fesperman, R. (2015). Measurement science needs for real-time control of additive manufacturing powder bed fusion processes. *NISTIR 8036, NIST*.

Marussig, B., Hiemstra, R., and Hughes, T. J. R. (2018). Improved conditioning of isogeometric analysis matrices for trimmed geometries. *Comput. Methods Appl. Mech. Engrg.*, 334:79 – 110.

Megahed, M., Mindt, H.-W., N'Dri, N., Duan, H., and Desmaison, O. (2016). Metal additive-manufacturing process and residual stress modeling. *Integrating Materials and Manufacturing Innovation*, 5(1).

Michaleris, P. (2014). Modeling metal deposition in heat transfer analyses of additive manufacturing processes. *Finite Elements in Analysis and Design*, 86:51–60. 00006.

Mills, K. C. (2002). *Recommended Values of Thermophysical Properties for Selected Commercial Alloys*. Woodhead, Cambridge.

National Institute of Standards and Technology (2013). Measurement science roadmap for metal based additive manufacturing. *NIST*.

O'Hara, P., Duarte, C., and Eason, T. (2011). Transient analysis of sharp thermal gradients using coarse finite element meshes. *Computer Methods in Applied Mechanics and Engineering*, 200(5):812–829.

Oxman N., K. S. and Tsai, E. (2011). *Functionally Graded Rapid Prototyping*. MIT Media Lab.

Pal, D., Patil, N., Kutty, K. H., Zeng, K., Moreland, A., Hicks, A., Beeler, D., and Stucker, B. (2016). A generalized feed-forward dynamic adaptive mesh refinement and derefinement finite-element framework for metal laser sintering part ii: Nonlinear thermal simulations and validations. *J of Manuf. Sci. Eng.*, 138(6):061003.

Papadakis, L., Loizou, A., Risse, J., Bremen, S., and Schrage, J. (2014). A computational reduction model for appraising structural effects in selective laser melting manufacturing: A methodical model reduction proposed for time-efficient finite element analysis of larger components in Selective Laser Melting. *Virtual and Physical Prototyping*, 9(1):17–25.

Parvizian, J., Düster, A., and Rank, E. (2007). Finite cell method. *Computational Mechanics*, 41(1):121–133.

Schillinger, D., Dedè, L., Scott, M. A., Evans, J. A., Borden, M. J., Rank, E., and Hughes, T. J. R. (2012). An isogeometric design-through-analysis methodology based on adaptive hierarchical refinement of NURBS, immersed boundary methods, and t-spline CAD surfaces. *Computer Methods in Applied Mechanics and Engineering*, 249-252:116–150.

Schoinochoritis, B., Chantzis, D., and Salonitis, K. (2017). Simulation of metallic powder bed additive manufacturing processes with the finite element method: A critical review. *Proceedings of the Institution of Mechanical Engineers, Part B: Journal of Engineering Manufacture*, 231(1):96–117.

Scott, M. A., Thomas, D., and Evans, E. (2014). Isogeometric spline forest. *Comput. Methods Appl. Mech. Engrg.*, 269:222–264.

Sigmund, O. (1997). On the design of compliant mechanism using topology optimization. *Mech. Struct. Mach.*, 25:495–526.

Sigmund, O. and Maute, K. (2013). Topology optimization approaches: A comparative review. *Structural and Multidisciplinary Optimization*, 48:1031–1055.

Sigmund, O. and Petersson, J. (1998). Numerical instabilities in topology optimization: A survey on procedures dealing with cheackboards, mesh-dependencies and local minima. *Structural Optimization*, 16:68–75.

Smith, J., Xiong, W., Yan, W., Lin, S., Cheng, P., Kafka, O. L., Wagner, G. J., Cao, J., and Liu, W. K. (2016). Linking process, structure, property, and performance for metal-based additive manufacturing: Computational approaches with experimental support. *Computational Mechanics*, 57(4):583–610.

Speleers, H. and Manni, C. (2016). Effortless quasi-interpolation in hierarchical spaces. *Numer. Math.*, 132:155–184.

Svenungsson, J., Choquet, I., and Kaplan, A. F. (2015). Laser Welding Process – A Review of Keyhole Welding Modelling. *Physics Procedia*, 78:182–191.

Tanaka, M. (2004). An introduction to physical phenomena in arc welding processes. *Welding International*, 18(11):845–851.

Tröltzsch, F. (2010). Optimal control of partial differential equations. theory, methods and applications. *Graduate Studies in Mathematics*, 112.

Vázquez, R. (2016). A new design for the implementation of isogeometric analysis in octave and matlab: Geopdes 3.0. *Comput. Math. Appl.*, 72:523–554.

Vuong, A., Giannelli, C., Jüttler, B., and Simeon, B. (2011). A hierarchical approach to adaptive local refinement in isogeometric analysis. *Comput. Methods Appl. Mech. Engrg.*, 200:3554–3567.

Warren, J. and Boettinger, W. (1995). Prediction of dendritic growth and microsegregation patterns in a binary alloy using the phase-field method. *Acta Metallurgica et Materialia*, 43(2):689–703.

www.nist.gov/ambench (2018). AM Bench benchmark challenge CHAL-AMB2018-02-MP. https://www.nist.gov/ambench/amb2018-02-description.

www.specialmetals.com (2019). Inconel 625 material properties. http://www.specialmetals.com.

www.upmet.com (2019). 316l steel material properties. https://www.upmet.com.

Yan, Z., Liu, W., Tang, Z., Liu, X., Zhang, N., Li, M., and Zhang, H. (2018). Review on thermal analysis in laser-based additive manufacturing. *Optics & Laser Technology*, 106:427–441.

Yeung, H., Lane, B., Donmez, M., Fox, J., and Neira, J. (2018). Implementation of advanced laser control strategies for powder bed fusion systems. *Procedia Manufacturing*, 26:871–879.

Yeung, H., Neira, J., Lane, B., Fox, J., and Lopez, F. (2016). Laser path planning and power control strategies for powder bed fusion systems. *Proceedings of the 27th Annual International Solid Freeform Fabrication Symposium*.

Zhou, M. and Sigmund, O. (2017). On fully stressed design and p-norm measures in structural optimization. *Struct Multidisc. Optim.*, 56:731–736.

Appendix A

AMBench CHAL-AMB2018-02

In this appendix we provide the list of process parameters and measurement results for each scan track of each sample made for AMBench CHAL-AMB2018-02 (see figure A.1).

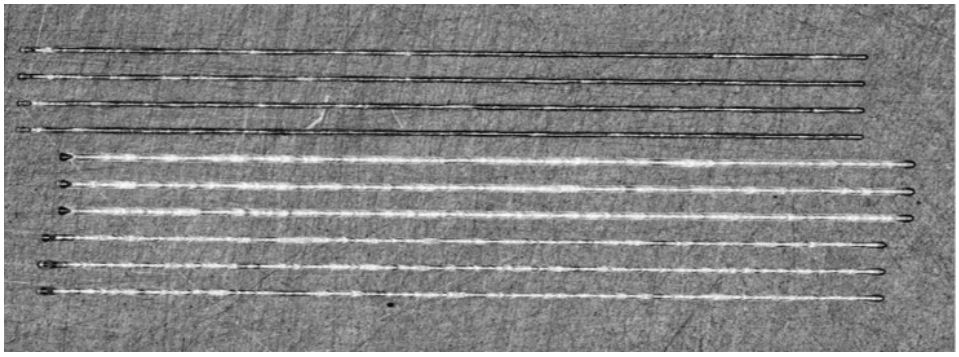

Figure A.1: Example of laser traces on the upper surface of a IN625 bare plate used for AMBench measurements. Courtesy of NIST.

Measurements for each individual track are provided together with their corresponding standard deviation ($\pm 1\sigma$). Table A.1 reports the melt pool (MP) length, width and depth measurements, while table A.2 reports the cooling rate (CR) measurements for two different temperature ranges. MP length and CR are calculated from the *true* temperature reconstructed from the thermal camera signal. MP width and depth are measured *ex-situ*: First the samples were cross sectioned through the middle of the laser path, then they were etched using aqua regia for a time from 20 s to 30 s and finally examined and photographed with a Zeiss LSM800 optical microscope.

Machine	#	Case	Power [W]	Speed [mm/s]	Laser Spot Diameter (D4σ) [νm]	#Video Frames	Int. Time [νs]	Effective Emittance	MP Length [νm]	MP Width [νm]	MP Depth [νm]
CBM	3	A	150	400	100	53	40	0.225 ±0.011	654 ±34	173.82 ±0.35	154.40 ±0.58
CBM	6	A	150	400	100	27	40	0.237 ±0.010	660 ±12	168.94 ±0.21	129.77 ±0.80
CBM	9	A	150	400	100	49	40	0.232 ±0.009	664 ±15	170.24 ±2.25	170.41 ±2.41
CBM	2	B	195	800	100	25	40	0.205 ±0.012	778 ±25	134.96 ±0.20	89.50 ±0.17
CBM	5	B	195	800	100	25	40	0.230 ±0.013	781 ±23	132.16 ±0.34	91.13 ±0.38
CBM	8	B	195	800	100	9	40	0.229 ±0.009	786 ±14	131.94 ±0.08	93.13 ±0.35
CBM	1	C	195	1200	100	11	40	0.169 ±0.020	756 ±56	97.82 ±0.20	59.61 ±0.39
CBM	4	C	195	1200	100	13	40	0.204 ±0.015	747 ±36	102.04 ±0.46	60.75 ±0.52
CBM	7	C	195	1200	100	15	40	0.220 ±0.018	758 ±44	100.73 ±0.16	60.03 ±0.35
CBM	10	C	195	1200	100	13	40	0.194 ±0.024	754 ±46	99.68 ±0.38	60.33 ±0.35
AMMT	5	A	137.9	400	170	51	100	0.673 ±0.034	350 ±8	144.00 ±0.32	44.40 ±0.12
AMMT	6	A	137.9	400	170	55	100	0.667 ±0.044	349 ±9	151.30 ±0.07	41.00 ±0.19
AMMT	7	A	137.9	400	170	55	100	0.679 ±0.060	346 ±9	148.50 ±0.36	42.10 ±0.11
AMMT	8	B	179.2	800	170	27	100	0.575 ±0.065	438 ±12	116.40 ±0.19	38.20 ±0.18
AMMT	9	B	179.2	800	170	31	100	0.581 ±0.062	421 ±13	129.10 ±0.14	34.80 ±0.04
AMMT	10	B	179.2	800	170	31	100	0.583 ±0.032	415 ±10	124.90 ±0.20	34.90 ±0.15
AMMT	1	C	179.2	1200	170	21	100	0.519 ⧫	444 ±13	104.40 ±0.19	29.00 ±0.08
AMMT	2	C	179.2	1200	170	22	100	0.519 ⧫	435 ±16	107.70 ±0.19	29.20 ±0.04
AMMT	3	C	179.2	1200	170	22	100	0.519 ⧫	445 ±14	106.60 ±0.07	30.00 ±0.00
AMMT	4	C	179.2	1200	170	16	100	0.519 ⧫	455 ±11	105.40 ±0.22	30.20 ±0.15
AMMT	2	A	137.9	400	170	19	20	0.600 ±0.016	300 ±12	152.00 ±2.00	43.00 ±0.90
AMMT	3	B	179.2	800	170	10	20	0.565 ±0.017	359 ±20	132.00 ±2.00	36.00 ±0.90
AMMT	1	C	179.2	1200	170	7	20	0.519 ±0.031	370 ±10	1113.00 ±2.00	29.00 ±0.90

Table A.1: Melt Pool Data
⧫ - Solidus could not be detected on these samples.

Machine	Track#	Case	Power [W]	Speed [mm/s]	Laser Spot Diameter (D4σ) [νm]	CR 1290°C-1190°C [°C/s]	CR 1290°C-1000°C [°C/s]
CBM	3	A	150	400	100	6.21E+05 ±7.19E+04	5.59E+05 ±4.46E+04
CBM	6	A	150	400	100	6.58E+05 ±9.41E+04	5.84E+05 ±5.96E+04
CBM	9	A	150	400	100	5.81E+05 ±4.38E+04	5.35E+05 ±2.55E+04
CBM	2	B	195	800	100	9.00E+05 ±1.65E+05	9.33E+05 ±9.24E+04
CBM	5	B	195	800	100	9.51E+05 ±1.44E+05	9.57E+05 ±8.16E+04
CBM	8	B	195	800	100	9.53E+05 ±1.11E+05	9.57E+05 ±7.74E+04
CBM	1	C	195	1200	100	1.31E+06 ±4.71E+05	1.38E+06 ±3.21E+05
CBM	4	C	195	1200	100	1.17E+06 ±3.71E+05	1.43E+06 ±2.46E+05
CBM	7	C	195	1200	100	1.40E+06 ±3.71E+05	1.54E+06 ±3.23E+05
CBM	10	C	195	1200	100	1.25E+06 ±3.13E+05	1.34+06 ±2.42E+05
AMMT	5	A	137.9	400	170	1.20E+07 ±5.66E+05	▼
AMMT	6	A	137.9	400	170	1.45E+07 ±4.77E+05	▼
AMMT	7	A	137.9	400	170	1.21E+07 ±7.15E+05	▼
AMMT	8	B	179.2	800	170	1.97E+07 ±1.27E+06	▼
AMMT	9	B	179.2	800	170	1.98E+07 ±1.82E+06	▼
AMMT	10	B	179.2	800	170	1.90E+07 ±1.85E+06	▼
AMMT	1	C	179.2	1200	170	2.90E+07 ±5.33E+06	▼
AMMT	2	C	179.2	1200	170	2.78E+07 ±4.88E+06	▼
AMMT	3	C	179.2	1200	170	2.76E+07 ±5.80E+06	▼
AMMT	4	C	179.2	1200	170	2.83E+07 ±4.46E+06	▼
AMMT	2	A	137.9	400	170	1.16E+06 ±2.68E+05	▼
AMMT	3	B	179.2	800	170	1.08E+06 ±5.88E+05	▼
AMMT	1	C	179.2	1200	170	1.90E+06 ±5.52E+05	▼

Table A.2: Cooling Rate Data
▼ - Due to the limited calibration range of camera on AMMT, temperature below 1100°C were too erroneous to use in cooling rate measurements.

Appendix B

Inconel 625 thermal properties

In this appendix we report the thermal properties of Nickel alloy Inconel 625. These values are taken from www.specialmetals.com [2019].

Table B.1: IN625; material constant parameters

density	8.44e-6 [kg/mm^3]
latent heat	2.8e5 [J/kg]
melting temperature interval	1290 - 1350 [°C]

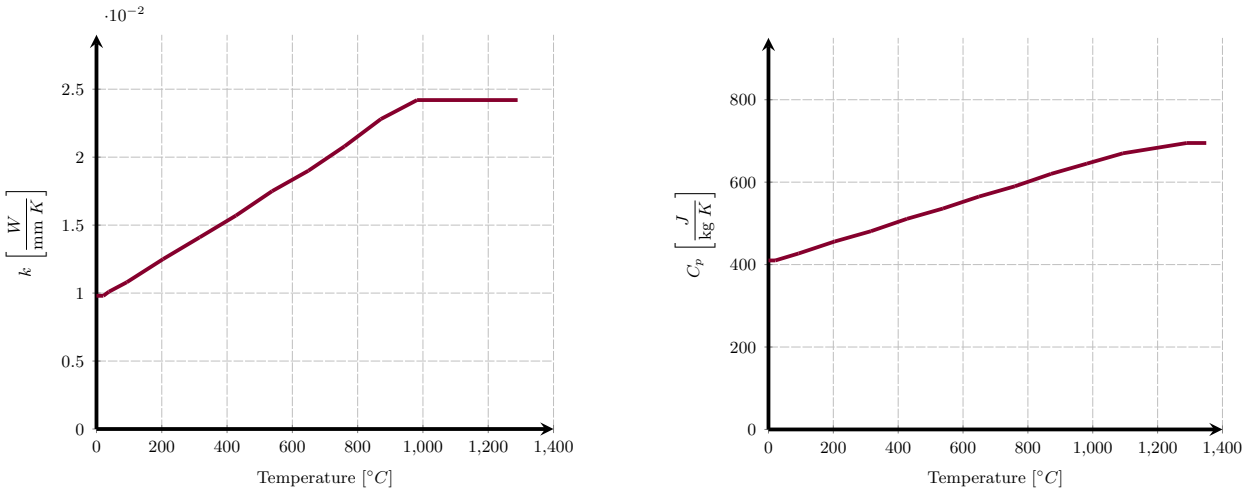

(a) Thermal conductivity.

(b) Specific heat capacity.

Figure B.1: IN625; temperature dependent material properties.

Appendix C

Steel 316L thermal properties

In this appendix we report the thermal properties of steel 316L. These values are taken from www.upmet.com [2019].

Table C.1: Steel 316L; material constant parameters

density	8.03e-6 [kg/mm^3]
latent heat	2.8e5 [J/kg]
melting temperature interval	1390 - 1440 [°C]

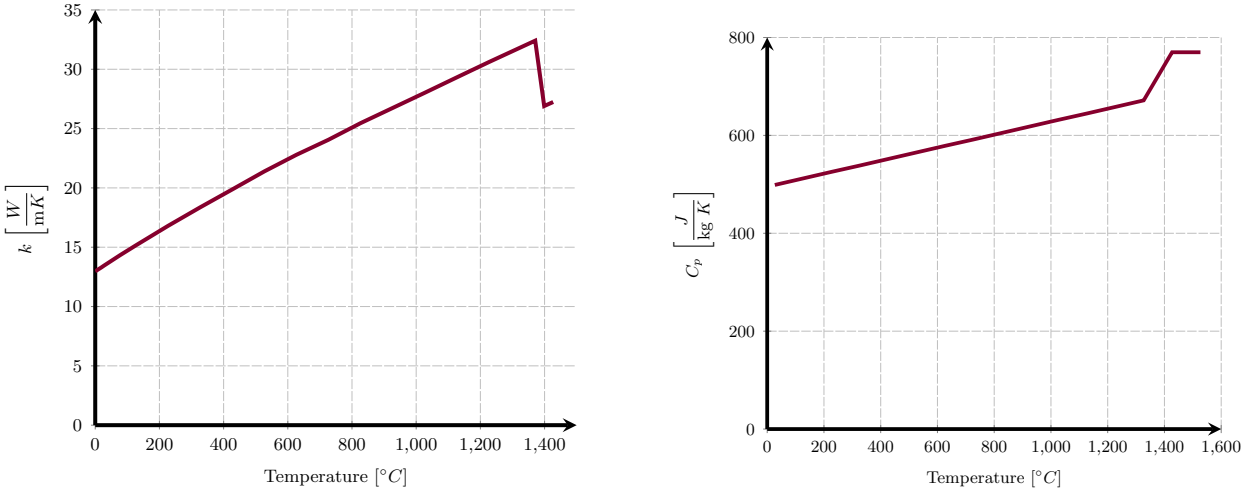

(a) Thermal conductivity.

(b) Specific heat capacity.

Figure C.1: Steel 316L; temperature dependent material properties.

Appendix D

Analytical results for FGM Topology Optimization

In this appendix we report the main analytical results and proofs, required to develop the optimization procedure developed in chapter 6.

Let us first introduce some notation in order to rewrite the state system in a weak form. Given a matrix $\mathbb{C}$, we introduce the product of matrices $\mathcal{A}$, $\mathcal{B}$

$$\langle \mathcal{A}, \mathcal{B} \rangle_{\mathbb{C}} := \int_{\Omega} \mathcal{A} \,:\, \mathbb{C}\mathcal{B},$$

where we have used the notation $\mathcal{A} \,:\, \mathcal{B} := \sum_{i,j=1}^{d} \mathcal{A}_{ij}\mathcal{B}_{ij}$. Then, the elastic boundary value problem 6.28 can be rewritten in a weak formulation as

$$\langle \boldsymbol{\varepsilon}(\mathbf{u}), \boldsymbol{\varepsilon}(\mathbf{v}) \rangle_{\mathbb{C}(\phi,\chi)} = G(\mathbf{v}, \phi) \quad \forall \mathbf{v} \in H^1_D(\Omega; \mathbb{R}^d) \tag{D.1}$$

where $G(\mathbf{v}, \phi) := \int_{\Omega} \phi\, \mathbf{f} \cdot \mathbf{v}\, d\Omega + \int_{\Gamma_g} \mathbf{g} \cdot \mathbf{v}\ d\Gamma$, and $\mathbb{C}(\phi, \chi)$ is the elasticity tensor defined as in 6.29. We define the convex set

$$C := \{(\phi, \chi) \,:\, \phi \in [0, 1], \quad \chi \in [0, \phi]\}. \tag{D.2}$$

Now, let us consider the following assumptions on the data introduced in section 6.1 .

Hypothesis D.0.1:
Assume that there exist positive constants c_w, θ, Θ, Λ such that

(**H1**) $\psi_0 \in C^1(\mathbb{R})$, $\psi_0 \geq -c_w$
(**H2**) $\mathbb{C}_{i,j,k,l} \in C^{1,1}(\mathbb{R}^2, \mathbb{R})$, $i, j, k, l \in \{1, \ldots, d\}$, $\mathbb{C}_{ijkl} = \mathbb{C}_{jikl} = \mathbb{C}_{ijlk} = \mathbb{C}_{klij}$, *and*

$$\theta|\mathcal{A}|^2 \leq \mathbb{C}(\phi, \chi)\mathcal{A} \,:\, \mathcal{A} \leq \Theta|\mathcal{A}|^2$$

,

$$|\partial_\phi \mathbb{C}(\phi, \chi)\mathcal{A} \,:\, \mathcal{B}| + |\partial_\chi \mathbb{C}(\phi, \chi)\mathcal{A} \,:\, \mathcal{B}| \leq \Lambda|\mathcal{A}||\mathcal{B}|\,,$$

for all symmetric matrices $\mathcal{A}$, $\mathcal{B} \in \mathbb{R}^{d\times d} \setminus \{\mathbf{0}\}$ and for all $\phi \in \mathbb{R}$
(**H3**) $(\mathbf{f}, \mathbf{g}) \in L^2(\Omega; \mathbb{R}^d) \times L^2(\Gamma_g; \mathbb{R}^d)$
(**H4**) $F \in C^1(\mathbb{R}^{d\times d}; \mathbb{R}^+)$ *is a convex function.*

The argument we are introducing exploits the results stated in Blank et al. [2014]. Actually, in our case we have to deal with two state variables (ϕ, χ) and with two control parameters $(\mathbf{u}, \boldsymbol{\sigma})$, so that the proofs have to be adapted to the vectorial case. For the sake of coherence we also use notations introduce in the same paper.

First, we recall a known result on the state system D.1 (cf. [Blank et al., 2014, Thm. 3.1, 3.2]).

Theorem D.0.2:
For any given $(\phi, \chi) \in L^\infty(\Omega) \times L^\infty(\Omega)$, there exists a unique $(\mathbf{u}, \boldsymbol{\sigma}) \in H^1(\Omega; \mathbb{R}^d) \times H(\mathrm{div}, \Omega)$ which fulfills equations (6.28e) *and* (D.1)*. Moreover, there exist positive constants C_1 and C_2 such that*

$$\|(\mathbf{u}, \boldsymbol{\sigma})\|_{H^1(\Omega;\mathbb{R}^d)\times H(\mathrm{div},\Omega)} \leq C_1(\|\phi\|_{L^\infty(\Omega)} + \|\chi\|_{L^\infty(\Omega)} + 1) \tag{D.3}$$

and

$$\begin{aligned} &\|\mathbf{u}_1 - \mathbf{u}_2\|_{H^1_D(\Omega;\mathbb{R}^d)} + \|\boldsymbol{\sigma}_1 - \boldsymbol{\sigma}_2\|_{L^2(\Omega,\mathbb{R}^{d\times d})} \leq \\ &C_2 \left(\|\phi_1 - \phi_2\|_{L^\infty(\Omega)} + \|\chi_1 - \chi_2\|_{L^\infty(\Omega)}\right) \end{aligned} \tag{D.4}$$

where C_2 depends on the problem data and on $\|\phi_i\|_{L^\infty(\Omega)}$, $\|\chi_i\|_{L^\infty(\Omega)}$, $i = 1, 2$ and $(\mathbf{u}_i, \boldsymbol{\sigma}_i) = \mathcal{S}(\phi_i, \chi_i)$, being $\mathcal{S} : (L^\infty(\Omega))^2 \to H^1_D(\Omega; \mathbb{R}^d) \times L^2(\Omega, \mathbb{R}^{d\times d})$ defined as the solution control-to-state operator which assigns to a given control (ϕ, χ) a unique state variable $(\mathbf{u}, \boldsymbol{\sigma}) \in H^1_D(\Omega; \mathbb{R}^d) \times L^2(\Omega, \mathbb{R}^{d\times d})$.

Then, we can state our main result related to the existence of solution to Problem (**CP**) and the derivation of first order necessary optimality conditions.

Theorem D.0.3:
The problem (**CP**) *has a minimizer.*

Proof. Let us denote by $\mathcal{G}_{ad} := \{(\mathbf{u}, \boldsymbol{\sigma}, \phi, \chi) \in \mathcal{U}_{ad} : (\mathbf{u}, \boldsymbol{\sigma}, \phi, \chi) \text{ fulfills D.1}\}$. By virtue of equation (D.1) and the Hypothesis Hypothesis D.0.1, and taking $\mathbf{v} = \mathbf{u}$ in equation (D.1), we can deduce that $\mathcal{J}$ is bounded from below on $\mathcal{G}_{ad}$, which is not empty. Thus, the infimum of $\mathcal{J}$ on $\mathcal{G}_{ad}$ exists and we can find a minimizing sequence $\{(\mathbf{u}_k, \boldsymbol{\sigma}_k, \phi_k, \chi_k)\} \subset \mathcal{G}_{ad}$. Moreover, using equation (D.3), we obtain that

$$\mathcal{J}(\mathbf{u}_k, \boldsymbol{\sigma}_k, \phi_k, \chi_k) \geq \delta \left(\frac{\gamma}{2}\|\nabla\phi_k\|^2_{L^2(\Omega)} + \frac{1}{2}\|\nabla\chi_k\|^2_{L^2(\Omega)}\right) - C_\delta$$

for some $\delta > 0$ and $C_\delta > 0$. This inequality follows by convexity and the boundedness of (ϕ, χ) (see, e.g., equation (D.2)). Hence, by using the fact that ϕ_k belong to $[0, 1]$ (cf. equation (D.2)) for all $k \in \mathbb{N}$ and by means of Poincaré inequality we obtain that the sequence $\{\phi_k\}$ is bounded in $H^1(\Omega) \cap L^\infty(\Omega)$. The same can be deduced for χ_k, which is uniformly bounded, too. Hence, by Theorem D.0.2, we have that also the sequences of $\{(\mathbf{u}_k, \boldsymbol{\sigma}_k)\}$ of corresponding states are bounded in $H^1_D(\Omega; \mathbb{R}^d) \times H(\mathrm{div}, \Omega)$ and that there exists, by compactness, some $(\bar{\mathbf{u}}, \bar{\boldsymbol{\sigma}}, \bar{\phi}, \bar{\chi}) \in H^1_D(\Omega; \mathbb{R}^d) \times H(\mathrm{div}, \Omega)) \times (H^1(\Omega; \mathbb{R}))^2$ such that (as $k \to \infty$) at least for subsequences

$$\mathbf{u}_k \to \bar{\mathbf{u}} \quad \text{weakly in } H^1_D(\Omega; \mathbb{R}^d) \quad \text{and strongly in } L^2(\Omega; \mathbb{R}^d) \tag{D.5}$$

$$\boldsymbol{\sigma}_k \to \bar{\boldsymbol{\sigma}} \quad \text{weakly in } L^2(\Omega; \mathbb{R}^{d\times d}) \tag{D.6}$$

$$\phi_k \to \bar{\phi} \quad \text{weakly in } H^1(\Omega) \quad \text{and strongly in } L^2(\Omega) \tag{D.7}$$

$$\chi_k \to \bar{\chi} \quad \text{weakly in } H^1(\Omega) \quad \text{and strongly in } L^2(\Omega)\,. \tag{D.8}$$

Moreover, since the set $\mathcal{U}_{ad}$ is convex and closed (and so also weakly closed), we also get $(\bar{\mathbf{u}}, \bar{\boldsymbol{\sigma}}, \bar{\phi}, \bar{\chi}) \in \mathcal{U}_{ad}$. Using $(\mathbf{H}_1)$ and the weak lower semicontinuity of I_C, of norms and of F (cf. (**H4**)), we get

$$\mathcal{J}(\bar{\mathbf{u}}, \bar{\boldsymbol{\sigma}}, \bar{\phi}, \bar{\chi}) \leq \lim_{k\to\infty} \mathcal{J}(\mathbf{u}_k, \boldsymbol{\sigma}_k, \phi_k, \chi_k).$$

Finally, due to the fact that $(\mathbf{u}_k, \boldsymbol{\sigma}_k, \phi_k, \chi_k)$ fulfills equation (D.1) we can deduce in addition that $(\bar{\mathbf{u}}, \bar{\boldsymbol{\sigma}}, \bar{\phi}, \bar{\chi})$ fulfills it because $\mathbb{C}(\phi_k, \chi_k)\boldsymbol{\varepsilon}(\mathbf{v})$ converges strongly to $\mathbb{C}(\bar{\phi}, \bar{\chi})\boldsymbol{\varepsilon}(\mathbf{v})$ in $L^2(\Omega; \mathbb{R}^{d\times d})$ and so, using equation (D.5), we get

$$\int_\Omega \mathbb{C}(\phi_k, \chi_k)\boldsymbol{\varepsilon}(\mathbf{u}_k) \,:\, \boldsymbol{\varepsilon}(\mathbf{v})\, d\Omega \to \int_\Omega \mathbb{C}(\bar{\phi}, \bar{\chi})\boldsymbol{\varepsilon}(\bar{\mathbf{u}}) \,:\, \boldsymbol{\varepsilon}(\mathbf{v})\, d\Omega\,.$$

Therefore $(\bar{\mathbf{u}}, \bar{\boldsymbol{\sigma}}, \bar{\phi}, \bar{\chi}) \in \mathcal{U}_{ad}$ turns out to be a minimizer for (**CP**). ∎

In order to deduce first order necessary optimality conditions, we first introduce the linearized system with respect to the variable ϕ and a direction h in a neighborhood of $(\bar{\phi}, \bar{\chi})$. We use the notation

$$(\boldsymbol{\xi}^h, \boldsymbol{\eta}^h) = \partial_\phi \mathcal{S}(\bar{\phi}, \bar{\chi})h,$$

where $(\boldsymbol{\xi}^h, \boldsymbol{\eta}^h)$ satisfies:

$$-\operatorname{div} \boldsymbol{\eta}^h = fh \quad \text{in } \Omega \tag{D.9}$$

$$\boldsymbol{\eta}^h \cdot \mathbf{n} = 0 \quad \text{on } \Gamma_g \tag{D.10}$$

$$\boldsymbol{\eta}^h = \mathbb{K}_\phi(\bar{\phi}, \bar{\chi})h\boldsymbol{\varepsilon}(\bar{\mathbf{u}}) + \mathbb{K}(\bar{\phi}, \bar{\chi})\boldsymbol{\varepsilon}(\boldsymbol{\xi}^h) \quad \text{in } \Omega. \tag{D.11}$$

Here $\bar{\mathbf{u}}$ stand for the first component of $\mathcal{S}(\bar{\phi}, \bar{\chi})$. Analogously, we introduce the linearized system with respect to χ in a general direction h. Letting

$$(\boldsymbol{\zeta}^h, \boldsymbol{\nu}^h) = \partial_\chi \mathcal{S}(\bar{\phi}, \bar{\chi})h,$$

where $(\boldsymbol{\zeta}^h, \boldsymbol{\nu}^h)$ satisfies:

$$-\operatorname{div} \boldsymbol{\nu}^h = 0 \quad \text{in } \Omega \tag{D.12}$$

$$\boldsymbol{\nu}^h \cdot \mathbf{n} = 0 \quad \text{on } \Gamma_g \tag{D.13}$$

$$\boldsymbol{\nu}^h = \mathbb{K}_\chi(\bar{\phi}, \bar{\chi})h\boldsymbol{\varepsilon}(\bar{\mathbf{u}}) + \mathbb{K}(\bar{\phi}, \bar{\chi})\boldsymbol{\varepsilon}(\boldsymbol{\zeta}^h) \quad \text{in } \Omega. \tag{D.14}$$

We can now reformulate the optimal control problem (**CP**) by means of the so-called reduced functional

$$j(\phi, \chi) := \mathcal{J}(\mathcal{S}(\phi, \chi), \phi, \chi)$$

which is Fréchet differentiable in $(H^1(\Omega) \cap L^\infty(\Omega))^2$. This fact is a consequence of the Fréchet differentiability of $\mathcal{J}$ (cf. [Blank et al., 2014, Lemma 4.2]), the differentiability of the control-to-state operator (cf. [Blank et al., 2014, Thm. 3.3]) and a standard chain rule formula (cf. [Tröltzsch, 2010, Thm. 2.20]). In particular, we have

$$\partial_\phi j(\phi, \chi)h = \mathcal{J}_{\mathbf{u}}(\mathbf{u}, \boldsymbol{\sigma}, \phi, \chi)\boldsymbol{\xi}^h + \mathcal{J}_{\boldsymbol{\sigma}}(\mathbf{u}, \boldsymbol{\sigma}, \phi, \chi)\boldsymbol{\eta}^h + \mathcal{J}_\phi(\mathbf{u}, \boldsymbol{\sigma}, \phi, \chi)$$

and

$$\partial_\chi j(\phi, \chi)h = \mathcal{J}_{\mathbf{u}}(\mathbf{u}, \boldsymbol{\sigma}, \phi, \chi)\boldsymbol{\zeta}^h + \mathcal{J}_{\boldsymbol{\sigma}}(\mathbf{u}, \boldsymbol{\sigma}, \phi, \chi)\boldsymbol{\nu}^h + \mathcal{J}_\chi(\mathbf{u}, \boldsymbol{\sigma}, \phi, \chi).$$

We can now restate the Problem (**CP**) in terms of minimizers of the cost functional, i.e., $(\mathbf{CP})_{\mathbf{R}}$:

$$\min_{(\phi,\chi)\in\mathcal{U}_{ad}} j(\phi,\chi). \tag{D.15}$$

Then, in order to find the first order necessary optimality conditions, we introduce the so-called Lagrangian:

$$\begin{aligned}\mathcal{L}(\mathbf{u},\boldsymbol{\sigma},\phi,\chi,\mathbf{U},\boldsymbol{\Sigma}) =& \mathcal{J}(\mathbf{u},\boldsymbol{\sigma},\phi,\chi) - \int_\Omega \boldsymbol{\sigma} \,:\, \boldsymbol{\varepsilon}(\mathbf{U})\, d\Omega + \int_\Omega \mathbf{f}\cdot(\phi\mathbf{U})\, d\Omega \\ &+ \int_{\Gamma_g} \mathbf{g}\cdot\mathbf{U}\, d\Omega + \int_\Omega (\boldsymbol{\sigma} - \mathbb{K}(\phi,\chi)\boldsymbol{\varepsilon}(\mathbf{u}))\boldsymbol{\Sigma}\, d\Omega.\end{aligned} \tag{D.16}$$

Thus, to get minimizers we consider the partial derivatives $\mathcal{L}_{\mathbf{u}}$ and $\mathcal{L}_{\boldsymbol{\sigma}}$ in direction $\mathbf{h}$ and impose that they are equal to zero. From these relations, it is straightforward, also by definition of $\mathcal{J}$, to derive the so-called adjoint equations. In particular, we get

$$\operatorname{div}(\mathbb{C}^T(\bar\phi,\bar\chi)\boldsymbol{\Sigma}) = \kappa_3\bar\varphi\mathbf{f} \quad \text{a.e. in } \Omega \tag{D.17}$$

$$\mathbb{C}^T(\bar\phi,\bar\chi)\boldsymbol{\Sigma}\cdot\mathbf{n} = \kappa_4\mathbf{g} \quad \text{a.e. on } \Gamma_g \tag{D.18}$$

$$\boldsymbol{\Sigma} = \boldsymbol{\varepsilon}(\mathbf{U}) - \kappa_5 F_{\boldsymbol{\sigma}}(\bar{\boldsymbol{\sigma}}) \quad \text{a.e. in } \Omega. \tag{D.19}$$

Note that since $(\bar\phi,\bar\chi)$ is a minimizer and $\mathcal{S}(\bar\phi,\bar\chi) = (\bar{\mathbf{u}},\bar{\boldsymbol{\sigma}}) \in H^1_D(\Omega;\mathbb{R}^d)\times H(\operatorname{div},\Omega)$, $(\mathbf{U},\boldsymbol{\Sigma}) \in H^1_D(\Omega;\mathbb{R}^d)\times H(\operatorname{div},\Omega)$ the corresponding state and adjoint variables, by convexity arguments it follows that the following inequality holds

$$(\mathcal{L}_{(\phi,\chi)}(\bar{\mathbf{u}},\bar{\boldsymbol{\sigma}},\bar\phi,\bar\chi,\bar{\mathbf{U}},\bar{\boldsymbol{\Sigma}}),(\phi,\chi)-(\bar\phi,\bar\chi)) \geq 0. \tag{D.20}$$

By means of this process we end up with the following main result.

Theorem D.0.4:
Let $(\bar\phi,\bar\chi)$ denote a minimizer of problem $(\mathbf{CP})_{\mathbf{R}}$ and $\mathcal{S}(\bar\phi,\bar\chi) = (\bar{\mathbf{u}},\bar{\boldsymbol{\sigma}}) \in H^1_D(\Omega;\mathbb{R}^d)\times H(\operatorname{div},\Omega)$, $(\mathbf{U},\boldsymbol{\Sigma}) \in H^1_D(\Omega;\mathbb{R}^d)\times H(\operatorname{div},\Omega)$ the corresponding state and adjoint variables. Then, $(\bar{\mathbf{u}},\bar{\boldsymbol{\sigma}},\bar\phi,\bar\chi,\bar{\mathbf{U}},\bar{\boldsymbol{\Sigma}})$ fulfills the optimality system in weak sense obtained coupling the state relations equations (D.17) *to* (D.19) *and the gradient inequality arising from equation* (D.20)*:*

$$\begin{aligned}&\kappa_1\int_\Omega \frac{\psi_0'(\bar\phi)}{\gamma}(\phi-\bar\phi)\, d\Omega + \kappa_1\gamma\int_\Omega \nabla\bar\phi\nabla(\phi-\bar\phi)\, d\Omega + \kappa_2\int_\Omega \nabla\bar\chi\nabla(\chi-\bar\chi)\, d\Omega \\ &+ \int_\Omega \mathbf{f}\cdot(\bar{\mathbf{U}}+\kappa_3\bar{\mathbf{u}})(\phi-\bar\phi)\, d\Omega - \kappa_3\int_\Omega \mathbb{C}_\phi(\bar\phi,\bar\chi)\boldsymbol{\Sigma} \,:\, \boldsymbol{\varepsilon}(\bar{\mathbf{u}})(\phi-\bar\phi)\, d\Omega \\ &- \kappa_3\int_\Omega \mathbb{C}_\chi(\bar\phi,\bar\chi)\boldsymbol{\Sigma} \,:\, \boldsymbol{\varepsilon}(\bar{\mathbf{u}})(\chi-\bar\chi)\, d\Omega \geq 0\end{aligned}$$

for all $(\phi,\chi)\in\mathcal{C}_{ad}$.